

Electronic Theses and Dissertations, 2004-2019

2016

Phase transformation and growth kinetics in reaction zone between uranium alloy and zirconium diffusion barrier

Young Joo Park
University of Central Florida

 Part of the [Materials Science and Engineering Commons](#)
Find similar works at: <https://stars.library.ucf.edu/etd>
University of Central Florida Libraries <http://library.ucf.edu>

This Doctoral Dissertation (Open Access) is brought to you for free and open access by STARS. It has been accepted for inclusion in Electronic Theses and Dissertations, 2004-2019 by an authorized administrator of STARS. For more information, please contact STARS@ucf.edu.

STARS Citation

Park, Young Joo, "Phase transformation and growth kinetics in reaction zone between uranium alloy and zirconium diffusion barrier" (2016). *Electronic Theses and Dissertations, 2004-2019*. 5094.
<https://stars.library.ucf.edu/etd/5094>

**PHASE TRANSFORMATION AND GROWTH KINETICS IN REACTION
ZONE BETWEEN URANIUM ALLOY AND ZIRCONIUM DIFFUSION
BARRIER**

by

YOUNG JOO PARK
B.S. Hanyang University, 2003
M.S. Hanyang University, 2005
M.S. University of Central Florida, 2013

A dissertation submitted in partial fulfillment of the requirements
for the degree of Doctor of Philosophy
in the Department of Materials Science and Engineering
in the College of Engineering and Computer Science
at the University of Central Florida
Orlando, Florida

Summer Term
2016

Major Professor: Yongho Sohn

© 2016 Young Joo Park

ABSTRACT

U-10wt.%Mo (U10Mo) alloy as a part of monolithic fuel system is being developed under Material Management and Minimization Reactor Conversion (MMMRC) program, tasked with replacing high-enriched uranium (HEU) fuel with low-enriched uranium (LEU) fuel in civilian research and test reactors. Use of U10Mo fuel alloy entails a Zr diffusion barrier to avoid the undesirable interdiffusion and reactions between the U10Mo and Al-alloy cladding. To better understand the interaction between these fuel system constituents, microstructural development and diffusion kinetics in U-Mo-Zr, U-Zr and fuel plate assembly processed by co-rolling and hot isostatic pressing (HIP) were investigated using a variety of analytical techniques accompanying scanning electron microscopy and transmission electron microscopy.

Phase constituents, microstructure and diffusion kinetics between U10Mo and Zr were examined using solid-to-solid diffusion couples annealed at 650 °C for 240, 480 and 720 hours. Concentration profiles were mapped as diffusion paths on the isothermal ternary phase diagram. Within the diffusion zone, single-phase layers of (γ U, β Zr) were observed along with a discontinuous layer of Mo₂Zr between the β Zr and β U layers. In the vicinity of Mo₂Zr phase, islands of α Zr phase were also found. In addition, acicular α Zr and U₆Zr₃Mo phases were observed within the γ U(Mo). Growth rate of the interdiffusion-reaction zone was determined to be 1.81×10^{-15} m²/sec at 650 °C, however with an assumption of a certain incubation period.

Investigation for interdiffusion and reaction between U and Zr were carried out using solid-to-solid diffusion couples annealed at 580, 650, 680 and 710 °C. The interdiffusion and reaction layer consisted of α U containing Zr acicular precipitate, α' (oC4-variant) and (γ U, β Zr) solid

solution at 650, 680 and 710 °C. The δ -UZr₂ phase, instead of (γ U, β Zr) solid solution phase, was observed in the couple annealed at 580 °C. The interdiffusion fluxes and coefficients were determined for the α U, (γ U, β Zr) and δ -UZr₂ (580 °C only) phases using both Sauer-Freise and Boltzmann-Matano analyses. For the α' -phase with negligible concentration gradient, integrated interdiffusion coefficients were determined via Wagner method. Marker plane was found in (γ U, β Zr) (c12) solid solution from the couples annealed at 650, 680 and 710 °C and δ -UZr₂ from the couple at 580 °C. Intrinsic diffusion coefficients at the compositions corresponding to the marker plane were determined based on Heumann analysis: U intrinsically diffused an order magnitude faster than Zr. Arrhenius temperature-dependence, Darken relation, and comparison to existing literature data demonstrated consistency in results.

Monolithic fuel plate assembly was fabricated by sequential process of (1) co-rolling to laminate the Zr barrier onto the U10Mo fuel alloy and (2) HIP to encase the fuel laminated with Zr, within the Al-alloy 6061 (AA6061). In this study, HIP process was carried out as functions of temperature (520, 540, 560 and 580 °C for 90 minutes), time (45, 60, 90, 180 and 345 minutes at 560 °C) with ramp-cool rate (35, 70 and 280 °C/hour). At the interface between the U10Mo and Zr, following the co-rolling, the UZr₂ phase was observed to develop adjacent to Zr, and the α U phase was found between the UZr₂ and U10Mo. Mo₂Zr was found as precipitates mostly within the α U phase. Observable growth due to HIP was only observed for the (Al,Si)₃Zr phase found at the Zr/AA6061 interface, however, with a large activation energy of 457 kJ/mol. Decomposition of γ U into α U and γ' was observed in the U10Mo alloy. The volume fraction of α and γ' increased as the HIP temperature and ramp-cool rate decreased. The UC-UO₂ inclusions within the U10Mo

fuel alloy were observed, but the volume percent of the UC-UO₂ inclusions within the U10Mo alloy, ranging from approximately 0.5 to 1.8, did not change as functions of HIP temperature and holding time. However, the inclusions located near the surface of the U10Mo alloy, were frequently observed to interfere the uniformity of interdiffusion and reaction between the U10Mo alloy and Zr diffusion barrier. The regions of limited interaction between the U10Mo and Zr barrier associated with UC-UO₂ inclusions decreased with an increase in HIP temperature, however no significant trend was observed with an increase in HIP duration at 560 °C.

I dedicate this work to God

ACKNOWLEDGMENTS

First and above all, I praise God, the almighty for providing me this opportunity and granting me the capability to proceed successfully.

I would like to express my sincere gratitude to my advisor, Dr. Yong-Ho Sohn for his support, guidance and patience; and I would also like to extend my thanks to my committee members: Dr. Dennis D. Keiser, Dr. Kevin Coffey, Dr. Jiyu Fang, and Dr. Yeonwoong Jung. I would also like to express my thanks to all my fellow students at the Laboratory of Materials and Coatings for Extreme Environment (MCEE) and to the engineers, faculty and staff members at the Advanced Materials Processing and Analysis Center (AMPAC) and the MSE department.

I am truly grateful to my parents for their immeasurable love. They have always prayed for me to be encouraged to complete my Ph. D.

These acknowledgements would not be complete without my wife Eunhee for her love and standing beside me. Also, I thank my little kids, Younwoo, Jiwoo and Siwoo, for making me so happy with their cute smile.

TABLE OF CONTENTS

LIST OF FIGURES	xi
LIST OF TABLES	xxi
CHAPTER 1: INTRODUCTION	1
1.1. Basic background	1
1.2. Motivation	2
1.3. Objectives	4
CHAPTER 2: LITERATURE REVIEW	6
2.1. Fuel design for Material Management and Minimization Reactor Conversion (MMMRC).....	6
2.2. Allotropic transformation of U	10
2.3. Composition of U-Mo alloy	11
2.4. Phase transformation of γ phase	11
2.5. U10Mo vs. Zr system	16
CHAPTER 3: EXPERIMENTAL DETAILS.....	17
3.1. Laboratory facility	17
3.2. Alloy preparation and diffusion experiment.....	19
3.3 Fabrication of HIP monolithic fuel plate at INL	20
3.3 Characterization.....	23
CHAPTER 4: ANALYTICAL FRAMEWORK	26

4.1. Time-dependent growth and Arrhenius relationship	26
4.2. Molar volume and Vegard's law	27
4.3. Boltzmann-Matano analysis	28
4.4. Sauer-Freise with Wagner analysis.....	29
4.5. Heumann analysis.....	31
CHAPTER 5: U10Mo vs. Zr DIFFUSION COUPLES.....	33
5.1. Background	33
5.2. Experimental Parameters.....	34
5.3. Results	34
5.3.1. Phase constituents and microstructure	34
5.3.2. Concentration profiles and diffusion paths.....	41
5.3.3. Time- and temperature-dependence of interdiffusion and reaction.....	42
5.4. Discussion	46
CHAPTER 6: U vs. Zr DIFFUSION COUPLES	50
6.1. Background	50
6.2. Experimental Parameters.....	51
6.3. Results	52
6.3.1. Phase constituents and microstructure	52
6.3.2. Diffusion kinetics	59
6.4. Discussion	72
CHAPTER 7: HOT ISOSTATIC PRESSED U10Mo MONOLITHIC FUEL PLATE.....	74

7.1. Background	74
7.2. Experimental Parameters.....	76
7.3. Results	76
7.3.1. Phase constituents and microstructure of typical features at U10Mo/Zr and Zr/AA6061 interfaces	76
7.3.2. Diffusion and kinetics analyses at U10Mo/Zr and Zr/AA6061 interfaces.....	83
7.3.3. Phase transformation of γ U within U10Mo	90
7.3.4. Phase constituents and microstructure of anomalous features	105
7.3.5. Image analyses for the anomalous features.....	113
7.4. Discussion	121
7.4.1. The U10Mo/Zr interface.....	121
7.4.2. The AA6061/Zr interface	122
7.4.3. U10Mo matrix	122
7.4.4. UC and UO ₂ inclusions at the U10Mo/Zr interface and U10Mo matrix.....	127
7.4.5. U10Mo-Zr system vs. U10Mo/Zr interface in HIP fuel plates	127
CHAPTER 8: Summary.....	130
APPENDIX A: MATHEMATICAL THEOREM FOR RECIPROCAL LATTICE.....	135
APPENDIX B: LIST OF PUBLICATIONS AND PRESENTATIONS	140
1. Journal Publications	141
2. Conference Presentations	142
LIST OF REFERENCE	145

LIST OF FIGURES

Figure 1. Schematic diagram of (a) dispersion and (b) monolithic fuels.....	7
Figure 2. Effective densities of U in fuel systems for research reactor [51].	7
Figure 3. Schematic illustrations of phase constituents observed by Perez <i>et al.</i> [39] at the interface between the U10Mo monolithic fuel and Zr diffusion barrier, and at the interface between Zr diffusion barrier and AA6061 cladding alloy.....	9
Figure 4. Allotropic crystal structures of α U, β U and γ U [68-70]......	10
Figure 5. TTT diagram of U-Mo alloys as a function of Mo composition.	12
Figure 6. U-Mo equilibrium phase diagram for (a) overall feature and (b) magnified feature indicated by the dotted line [52].	13
Figure 7. TTT diagram of U10Mo alloy [63].	14
Figure 8. (a) Glove box under a controlled Ar atmosphere and (b) the schematic diagram of gas flow for alloy handling.....	17
Figure 9. High vacuum system for evacuating quartz capsules.....	18
Figure 10. Lindberg/Blue TM three-zone tube furnace.	18
Figure 11. Quartz capsules for heat treatment of diffusion couples.	20
Figure 12. A schematic illustration of co-rolling employed in this investigation to produce U10Mo monolithic fuel encased in AA6161 with Zr diffusion barrier.	22
Figure 13. A schematic diagram of HIP.	23
Figure 14. (a) Zeiss ULTRA-55 FEG SEM (b) FEI TEM200 FIB (c) FEI TECNAI F30 TEM. .	24
Figure 15. FIB sample preparation: (a) initial milling completion (b) in-situ lift-out (c) insertion	

of sample onto the pre-slotted Cu-grid (d) welding the sample on Cu-grid.	25
Figure 16. Concentration profile to explain the Huemman’s analysis for determination of the intrinsic diffusion coefficients	32
Figure 17. Backscattered electron micrographs from U10Mo vs. Zr diffusion couples annealed at 650 °C for (a) 240, (b) 480 and (c) 720 hours followed by water-quench, and (d) for 480 hours followed by furnace-cooling.	35
Figure 18. High angle annular dark field micrographs from the water-quenched U10Mo vs. Zr diffusion couple annealed at 650 °C for 720 hours.....	36
Figure 19. From region (1) in Figure 18: (a) Bright field and (b) high-resolution TEM micrographs with the fast Fourier transformation analysis of needle-shaped α Zr precipitate in the water-quenched U10Mo vs. Zr diffusion couples annealed at 650 °C for 720 hours.	37
Figure 20. From region (2) in Figure 18: selected area electron diffraction patterns from the (a) β Zr, (b) Mo_2Zr and (c) β U layers observed in the water-quenched U10Mo vs. Zr diffusion couples annealed at 650 °C for 720 hours.	37
Figure 21. From region (2) in Figure 18: (a) dark field and (b) high-resolution TEM micrographs of the α Zr precipitates observed within the β U layer formed in the water-quenched U10Mo vs. Zr diffusion couples annealed at 650 °C for 720 hours.	38
Figure 22. From region (3) in Figure 18: (a) dark field and (b) high-resolution TEM micrographs with the fast Fourier transformation analysis of $\text{U}_6\text{Zr}_3\text{Mo}$ precipitate within the U - Mo matrix from the water-quenched U10Mo vs. Zr diffusion couples annealed at 650 °C for	

720 hours.....	39
Figure 23. Schematic diagram of the interaction layers from the water-quenched U10Mo vs. Zr diffusion couple annealed at 650 °C for 720 hours.....	40
Figure 24. Concentration profiles from U10Mo vs Zr diffusion couples annealed at 650 °C for 720 hours after water-quench.....	43
Figure 25. Estimated diffusion paths from U10Mo vs. Zr diffusion couples annealed at 650 °C for 480 hours after water-quench and furnace-cooling.....	44
Figure 26. Thickness of the diffusional interaction zone as a function of time for the U10Mo vs Zr diffusion couples annealed at 650 °C followed by water-quench.....	45
Figure 27. Temperature dependence of growth constant from U10Mo vs. Zr diffusion couples annealed at 1000, 900, 800 [43] and 650 °C.....	46
Figure 28. U-Zr equilibrium phase diagram with annealed temperatures for U-Zr isothermal diffusion couples.....	51
Figure 29. BSE micrographs from the water-quenched U vs. Zr diffusion couples annealed (a) at 580 °C for 960 hours, (b) at 650 °C for 480 hours, (c) at 680 °C for 240 hours, and (d) at 710 °C for 96 hours. The selected areas (red-dot rectangular) in (a) and (c) are indicated for TEM analyses.....	53
Figure 30. BSE micrographs from the water-quenched U vs. Zr diffusion couples annealed at 580 °C for (a) 360, (b) 480, (c) 720 and (d) 960 hours.....	54
Figure 31. High angle annular dark field micrographs of the water-quenched U vs. Zr diffusion couple annealed at 650 °C for 480 hours selected from Figure 29(c).	55

Figure 32. Selected area diffraction patterns of (a) (γ U, β Zr) solid solution and (b) α U.	56
Figure 33. The precipitate flakes for (a) BF and (b) HR-TEM with FFT analysis of α Zr (hP2), and (c) BF and (d) HR-TEM with FFT analysis of UZr ₂ (hP3).....	56
Figure 34. (a) BF micrograph of the water-quenched U vs. Zr diffusion couple annealed at 580 °C for 960 hours selected from Figure 29(a). (b) SAED pattern and (c) HR-TEM micrograph with FFT analysis selected from the red circle area in (a). Intensities of the pixel at the positions for lattice parameter (d) a and (e) b measured from the red and blue lines, respectively.	58
Figure 35. (a, c, e, g) Concentration profiles and (b, d, f, h) flux profiles for U-Zr diffusion couples annealed (a, b) at 580 °C for 960 hours, (c, d) at 650 °C for 480 hours, (e, f) at 680 °C for 240 hours and (g, h) at 710 °C for 96 hours.....	61
Figure 36. Interdiffusion coefficients determined using the Boltzmann-Matano method as a function of composition (at.% Zr).	62
Figure 37. Integrated interdiffusion coefficients determined according to Sauer-Freise with Wagner analysis as a function of temperature.	63
Figure 38. The interdiffusion coefficients at 71 at.% Zr as a function of temperature for Akabori <i>et al.</i> [99], Ogata <i>et al.</i> [97] and this study.	66
Figure 39. Intrinsic diffusion coefficient for (γ U, β Zr) as a function of temperature.....	67
Figure 40. Thickness of the diffusional interaction zone as a function of time for the U vs. Zr diffusion couples annealed at 580 °C followed by water-quench.....	70
Figure 41. Temperature dependence of growth constants determined from the U vs Zr diffusion	

<p>couples annealed at 580 °C for 960 hours, at 650 °C for 480 hours, at 680 °C for 240 hours and at 710 °C for 96 hours.</p>	72
<p>Figure 42. Typical backscatter electron micrograph of the U10Mo monolithic fuel encased in AA6061 with Zr diffusion barrier, produced by co-rolling and HIP'ing (sample 56-345-280, HIP'ed at 560 °C for 345 minutes with 280 °C/hour).</p>	77
<p>Figure 43. Backscatter electron micrograph from U10Mo monolithic fuel laminated with Zr diffusion barrier via co-rolling (sample AR, as co-rolled prior to HIP).</p>	77
<p>Figure 44. Backscatter electron micrographs from (a) the interface between U10Mo monolithic fuel and Zr diffusion barrier, and (b) the interface between Zr diffusion barrier and AA6061 cladding alloy (sample 56-345-280, HIP'ed at 560 °C for 345 minutes with 280 °C/hour).</p>	78
<p>Figure 45. High angle annular dark field TEM micrographs from (a) the interface between U10Mo monolithic fuel and Zr diffusion barrier, and (b) the interface between Zr diffusion barrier and AA6061 cladding alloy (sample 56-345-280, HIP'ed at 560 °C for 345 minutes with 280 °C/hour). An arrow in (a) corresponds to the small Mo₂Zr precipitate found within the UZr₂ away from the Zr diffusion barrier.</p>	80
<p>Figure 46. Selected area electron diffraction patterns from (a,b) γU(Mo) solid solution, (c,d) αU, (e,f) Mo₂Zr, and (g,h) UZr₂ phases at the interface between U10Mo monolithic fuel and Zr diffusion barrier (sample 56-345-280, HIP'ed at 560 °C for 345 minutes with 280 °C/hour).</p>	80
<p>Figure 47. Selected area electron diffraction patterns from (a) the continuous layer of (Al,Si)₃Zr</p>	

adjacent to Zr diffusion barrier and (b) the discontinuous $(Al,Si)_3Zr$ protrusions adjacent to AA6061 at the interface between Zr diffusion barrier and AA6061 cladding alloy (sample 56-345-280, HIP'ed at 560 °C for 345 minutes with 280 °C/hour). 81

Figure 48. Measured thickness of interaction layer between the U10Mo monolithic fuel and Zr barrier after HIP'ing at 560 °C as a function of time in (a) longitudinal and (b) transverse directions. 84

Figure 49. Measured thickness of interaction layer between the Zr barrier and AA6061 after HIP'ing at 560 °C as a function of time in (a) longitudinal and (b) transverse directions. 84

Figure 50. Measured thickness of interaction layer between the U10Mo monolithic fuel and Zr barrier after HIP'ing for 90 min as a function of temperature range from 520 to 580 °C in (a) longitudinal and (b) transverse directions. 86

Figure 51. Measured thickness of interaction layer between the Zr barrier and AA6061 after HIP'ing for 90 min as a function of temperature range from 520 to 580 °C in (a) longitudinal and (b) transverse directions. 86

Figure 52. Temperature dependence of growth constant determined for the interaction layer developed at the interface between the Zr barrier and AA6061 during HIP'ing. 88

Figure 53. Cellular structure resulted from decomposition of γ into α and γ' in the microstructure of AR sample. 92

Figure 54. Backscattered electron micrographs for the U10Mo of HIP fuel plates co-rolled at 560 °C for 90 minutes with variation in ramping and cooling rate: (a) 280, (b) 70, and

(c) 35 °C/hour.....	93
Figure 55. High magnification BSE of lamellar structure for the U10Mo of HIP fuel plates co-rolled at 560 °C for 90 minutes with ramping and cooling rate of 35 °C/hour.....	94
Figure 56. The volume fraction of decomposed constituents area in the U10Mo alloy as a function of ramping and cooling rate.....	95
Figure 57. The heat treatment traces on the TTT diagram of U10Mo for the ramping and cooling rates of 35, 70 and 280 °C/hour at 560 °C for 90 minutes.....	96
Figure 58. TEM (a) HAADF and (b) BF micrographs for the reaction zone by decomposition of γ U10Mo into α U and γ' U ₂ Mo in 56-90-35 HIP'ed at 560 °C for 90 minutes with 35 °C/hour.....	97
Figure 59. Selected area electron diffraction patterns from the decomposition reaction zone of 56-345-35 HIP'ed at 560 °C for 345 minutes with 35 °C/hour (a) γ U10Mo, (b) γ U ₂ Mo and (c) α U.....	98
Figure 60. Backscattered electron micrographs for the U10Mo of HIP fuel plates co-rolled for 90 minutes with ramping and cooling rate of 280 °C/hour at: (a) 520, (b) 540, (c) 560 and (d) 580 °C.....	100
Figure 61. The volume fraction of decomposed constituents area in the U10Mo alloy as a function of HIP'ed temperature.....	101
Figure 62. The heat treatment traces on the TTT diagram of U10Mo for the HIP'ed temperature of 520, 540, 560 and 580 °C for 90 minutes with 280 °C/hour.....	102

Figure 63. Backscattered electron micrographs for the U10Mo of HIP fuel plates co-rolled at 560 °C with ramping and cooling rate of 280 °C/hour for: (a) 45, (b) 60, (c) 90, (d) 180 and (e) 345 minutes.....	103
Figure 64. The heat treatment traces on the TTT diagram of U10Mo for the HIP'ed holding time of 45, 60, 90, 180 and 345 minute at 560 °C with 280 °C/hour.....	104
Figure 65. The volume fraction of decomposed constituents area in the U10Mo alloy as a function of HIP'ed temperature.	105
Figure 66. (a) Anomalous microstructure associated with the UC and UO ₂ phases, and (b) the imperfect reaction zone in U10Mo alloy (from sample 56-345-280, HIP'ed at 560 °C for 345 minutes with 280 °C/hour).	106
Figure 67. (a) High angle annular dark field (HAADF) scanning transmission electron microscopy (STEM) micrograph and (b) bright field (BF)micrograph from the UC and UO ₂ inclusion phases (TEM specimen prepared from Figure 66(a) from sample 56-345-280, HIP'ed at 560 °C for 345 minutes with 280 °C/hour).	107
Figure 68. Selected area electron diffraction patterns from the UC phase in (a) [1 1 2] and (b) [1 1 1] beam directions (TEM specimen prepared from Figure 66(a) from sample 56-345-280, HIP'ed at 560 °C for 345 minutes with 280 °C/hour).	107
Figure 69. High resolution TEM micrographs with the fast Fourier transform analysis along the [0 1 1] and [0 0 1] beam directions for the UO ₂ phase (TEM specimen prepared from Figure 66(a) from sample 56-345-280, HIP'ed at 560 °C for 345 minutes with 280 °C/hour).	108

Figure 70. HAADF STEM micrograph of the region with limited interdiffusion and reaction near the interface between the U10Mo alloy and Zr diffusion barrier. Contrast developed by composition and orientation shows UC (white arrows) and UO₂ (black arrows) phases (TEM specimen prepared from Figure 66(b) from sample 56-345-280, HIP'ed at 560 °C for 345 minutes with 280 °C/hour)..... 111

Figure 71. (a) Bright field micrograph and high resolution TEM micrographs with the fast Fourier transform analyses for the (b) UC and (c) UO₂ phases (TEM specimen prepared from Figure 66(b) from sample 56-345-280, HIP'ed at 560 °C for 345 minutes with 280 °C/hour). 112

Figure 72. XEDS elemental mapping of Figure 70 (TEM specimen prepared from Figure 66(b) from sample 56-345-280, HIP'ed at 560 °C for 345 minutes with 280 °C/hour)..... 113

Figure 73. The measurement of area percent for the UC and UO₂ phases distributed in the U10Mo alloy. 116

Figure 74. Estimate volume fraction of the UC and UO₂ inclusion phases distributed in the U10Mo monolithic fuel after HIP'ing (a) at 560 °C as a function of time, and (b) after 90 minutes as a function of time. “AR” refers to the estimated volume fraction in as-rolled sample prior to HIP process..... 117

Figure 75. Illustration of the linear measurement for regions with limited interdiffusion and reaction between the U10Mo alloy and Zr diffusion barrier..... 118

Figure 76. Estimated area of limited interdiffusion and reaction between the U10Mo and Zr diffusion barrier during HIP'ing as (a) a function of temperature after 90 minutes and

(b) a function of time at 560 °C. “AR” refers to the estimated volume fraction in as-rolled sample prior to HIP process..... 120

Figure 77. Schematic diagram for nucleation of cellular structure and development of lamellar structure..... 125

Figure 78. The procedure C++ coding for the identification of crystal structure and indexing . 139

LIST OF TABLES

Table 1. Atomic characteristics of Mo, Zr and Nb [40-42].	3
Table 2. Properties for γ , α and γ' [4, 12, 52, 60, 73, 77-82].	15
Table 3. List of monolithic fuel plate assemblies examined as functions of temperature, time and ramp-cool rate of HIP under 103 MPa (~15 ksi).	21
Table 4. Crystallographic information on relevant phases of this investigation.	40
Table 5. Growth rate of diffusional interaction zone determined from U10Mo vs. Zr diffusion couple annealed at 650 °C followed by water-quench.	44
Table 6. Growth rate of interaction zone of U10Mo vs. Zr diffusion couples reported by Huang <i>et al.</i> [43] and this study.	45
Table 7. Crystallographic data for each phase.	59
Table 8. Integrated interdiffusion coefficient (D_{int}), pre-exponential factor (D_{0int}) and the corresponding activation energy (Q_{int}) for Zr in each phase.	64
Table 9. Intrinsic diffusion coefficients (D_{Zr} and D_U), and interdiffusion coefficients determined by the Darken equation (DD) and the Boltzmann-Matano method (DBM). Pre-exponential factor and activation energy for each diffusion coefficient.	68
Table 10. Total thickness for each U-Zr system annealed at 580 °C.	69
Table 11. Layer thickness, parabolic growth constant and the corresponding activation energy for each layer in U-Zr system.	71
Table 12. Incubation times, growth constants, pre-exponential factors and activation energies for the U-Zr and U10Mo-Zr diffusion couples annealed at 650 °C.	73

Table 14. Crystallographic information for all the phases observed by TEM in this investigation.	82
Table 15. The average growth constants and activation energy calculated from the layer growth at the interface between Zr and AA6061 as functions of HIP parameters.....	89
Table 16. Crystallographic details, properties, and chemical compositions for the UC, UO ₂ and γ (U10Mo) phases [52, 60, 71, 81, 106, 108-113]. The chemical compositions reported are typical values observed in this study by semi-quantitative standard-less XEDS. ..	109
Table 17. HIP plate samples examined in this study along with estimated quantity of microstructural anomalies.....	115
Table 18. The observed phases for each heat treatment in previous researches and the indicated in TTT diagram.	126
Table 19. The critical temperatures of U10Mo alloy for the phase transformations.	126
Table 20. Comparison the U10Mo-Zr system and the U10Mo/Zr interface in HIP fuel plate. ..	129

LIST OF ABBREVIATIONS

AA6061	Aluminum Alloy 6061
AFCI	Advanced Fuel Cycle Initiative
BCC	Body Centered Cubic
at.%	Atomic percent
BSE	Backscattered Electron Micrograph
DF	Dark Field imaging
DU	Depleted Uranium
EDS/XEDS	Energy Dispersive X-Ray Spectroscopy
FCC	Face Centered Cubic
FCCI	Fuel-Cladding Chemical Interaction
FFT	Fast-Fourier Transformation
FIB	Focused Ion Beam
Gen-IV	Generation IV
GTRI	Global Threat Reduction Initiative
HAADF	High-Angle Annular Dark-Field
HIP	Hot Isostatic Press
HR-TEM	High Resolution Transmission Electron Microscopy
INL	Idaho National Laboratory
INLO	In-situ Lift Out
MMMRC	Material Management and Minimization Reactor Conversion

RERTR	Reduced Enrichment for Research and Test Reactors
SAED	Selected Area Electron Diffraction
SE	Secondary Electron imaging
SEM	Scanning Electron Microscope
SFR	Sodium-Cooled Fast Reactor
STEM	Scanning Transmission Electron Microscopy
TEM	Transmission Electron Microscopy
TTT	Time Temperature Transformation
U7Mo	U-7 weight % Mo
U10Mo	U-10 weight % Mo
wt. %	Weight Percent
XEDS	X-ray Energy Dispersive Spectroscopy
XRD	X-ray Diffraction
ZAF	Atomic number, Absorption and Fluorescence correction

CHAPTER 1: INTRODUCTION

1.1. Basic background

Metallic fuels are the most appropriate type of nuclear fuel with excellent performance and properties for the Material Management and Minimization Reactor Conversion (MMMRC) previously known as the Global Threat Reduction Initiative (GTRI) and the Reduced Enrichment for Research and Test Reactors (RERTR), and the Advanced Fuel Cycle Initiative (AFCI) programs [1-3]. The metallic fuels have high burnup ability, high thermal conductivity, compatibility for fabrication and advantage of recycling. Furthermore, the metallic fuels have capability to develop advanced fuel design through alloying with elements such as Mo, Zr, Nb, Ti, Pu and so on to overcome their own adverse properties. In U-Mo and U-Zr fuel alloys, the alloying addition of Mo and Zr stabilizes the (bcc) metastable γ U phase in lower temperature ranges than high purity U (<668°C, α U; 668-776°C, β U; >776°C, γ U). The γ U exhibits better performance than either the α U or U β during irradiation testing. The Mo and Zr have wide solubility in γ U, which allows for fuel customization, while satisfying the fissile-U densities required by various reactor designs. Many investigations have been carried out to develop an understanding of the phase equilibria/thermodynamics [4-9], kinetics [9, 10], mechanical properties [11, 12], and irradiation behavior [13-17] for the binary alloys.

U-Mo alloy is being considered as the metallic fuel for development of low-enriched uranium (LEU) fuel under the MMMRC program [18, 19]. LEU is being developed to replace

high-enriched uranium (HEU) fuel in research and test reactors around the world. This is consistent with a U.S. policy to eliminate proliferation of HEU from civilian facilities [20]. In order to achieve equivalent performance of HEU fuel, higher U-density in LEU fuel is required.

1.2. Motivation

Although the metallic fuels have been considered as an ideal fuel for MMMRC and AFCI programs, a few potential challenges have been reported. Among them, the fuel cladding chemical interaction (FCCI) has been reported as a critical factor that can adversely affect the performance and reliability of the fuels [21-23]. During the operation, the metallic fuels can swell (i.e., volumetric expansion) due to neutron irradiation, and contact the cladding alloys. This contact between the fuel and cladding can then induce the interdiffusion [13, 14, 24-37], alter the composition, microstructure and properties of both the fuel and cladding, and can cause a premature failure of fuel elements. In addition, during irradiation, undesirable fission gas bubbles can form in the interdiffusion and reaction zone between the U7Mo and Al. [14, 33]. Therefore, in order to minimize the deleterious effects by interdiffusion and optimize the fuel design, it is necessary to utilize a diffusion barrier. An ideal diffusion barrier to ensure good fuel performance and reliability could have following characteristics:

- Good thermal conductivity
- Low neutron absorption cross section
- Good chemical resistant

- High melting point
- Low thermal expansion coefficient
- Low diffusivity between fuel and cladding

Table 1 shows the characteristics of potential diffusion barriers, Mo, Zr and Nb, such as low neutron absorption, high melting point, high thermal conductivity and good corrosion resistance. In this dissertation, Zr has been examined because of the lowest neutron adsorption rate and the best compatible fabrication of fuel system using hot rolling process [38, 39].

Table 1. Atomic characteristics of Mo, Zr and Nb [40-42].

Property	Mo	Zr	Nb
Neutron absorption (barn)	2.48	0.18	1.15
Density (gcm ⁻³)	10.22	6.49	8.35
Melting point (°C)	2623	1854	2477
Thermal expansion coefficient (K ⁻¹)	5.35×10 ⁻⁶	5.78×10 ⁻⁶	7.34×10 ⁻⁶
Thermal Conductivity (Wm ⁻¹ K ⁻¹)	138	22.7	54
Corrosion resistance	Good	Good	Good

Diffusion couples of U10Mo and Zr were used to investigate the interdiffusion and reaction as a function of temperature with selected annealed time [43]. Also, the interdiffusion behaviors for the elements in the ternary U-Mo-Zr as a function of annealed time at 650 °C have to be studied

to understand the growth kinetics and microstructural evolution during co-rolling process to laminate Zr with the U10Mo plate [39, 44-46].

The U10Mo monolithic fuels (i.e., U10Mo plate with Zr diffusion barrier encased in AA6061 cladding) are being considered as more appropriate fuel design than the U7Mo dispersion fuel (i.e., U7Mo particles dispersed in Al matrix, 8 g/cm³) to achieve the primary objective of the MMMRC program because of higher U-density in the fuel meat. Therefore, monolithic fuel plates have been subjected to several heat-treatment processes, pre- and post-heating for lamination of Zr on U10Mo, and then HIP'ed for encasing the U10Mo/Zr fuel meat in AA6061 [44, 45, 47]. In order to optimize the fabrication process, microstructural and kinetics analyses were carried out for monolithic fuel plates as function of fabrication parameters have to be investigated.

1.3. Objectives

Three primary objectives of this stud are: (1) investigation of the interdiffusion behavior in the binary U vs. Zr system, (2) investigation of the interdiffusion behavior in the ternary U10Mo vs Zr system for understanding the complex reaction zone in the HIP fuel plates, and (3) characterization for microstructural and kinetics analysis for HIP fuel plates as functions of fuel fabrication processes.

To fulfill these objectives, the following studies have been conducted for the development of optimized fuel for the MMMRC:

1. Investigation of U vs. Zr diffusion couples as a function of annealed time at

580 °C, and as a function of temperature with pre-determined annealed time.

2. Investigation of U10Mo vs. Zr diffusion couples as a function of annealed time at 650 °C to understand interdiffusion behavior of elements in the ternary U-Mo-Zr system.
3. Investigation of interdiffusion and reaction at the U10Mo/Zr interface in HIP fuel plates.
4. Investigation of interdiffusion and reaction at the Zr/AA6061 interface in HIP fuel plates.
5. Investigation of phase transformation of γ into α and γ' via eutectoid reaction in the binary U-Mo system as functions of HIP parameters such as temperature, holding time and ramp-cool rate.
6. consideration for optimized fuel fabrication parameters.

CHAPTER 2: LITERATURE REVIEW

2.1. Fuel design for Material Management and Minimization Reactor Conversion (MMMRC)

The replacement of high-enriched uranium (HEU, $^{235}\text{U} > 20$ at.%) fuel with low-enriched uranium (LEU, $^{235}\text{U} < 20$ at.%) fuel is the primary goal of the MMMRC program [18, 20, 48]. To achieve this goal, the density of uranium in the fuel meat has to increase for the equivalent performance of fuel as delivered by the highly enriched fuel meat.

The metallic fuel based on the U10Mo alloy has been examined for MMMRC applications and implemented in selected research and test reactors [18, 20, 48]. Figure 1 illustrates two types of fuel designs. The U7Mo dispersion fuel (i.e., U7Mo particles dispersed in Al-alloy matrix) with uranium loading of 8 g/cm^3 have been fabricated and implemented [49]. However, some test reactors require even higher U-density in the fuel meat. The U10Mo monolithic fuel (i.e., U10Mo plate encased in Al-alloy cladding) can achieve a uranium density of around 15.6 g/cm^3 , and has been a subject of many recent investigations [50]. Effective densities of U in various fuels for research and test reactions are presented in Figure 2.

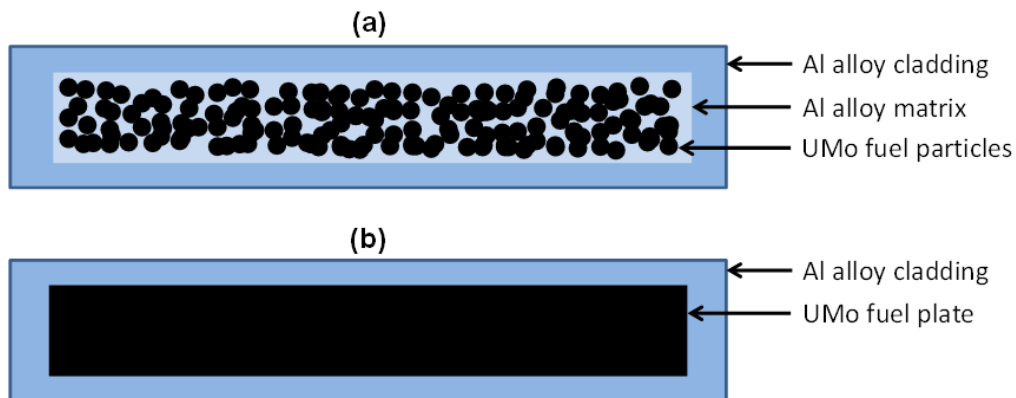


Figure 1. Schematic diagram of (a) dispersion and (b) monolithic fuels.

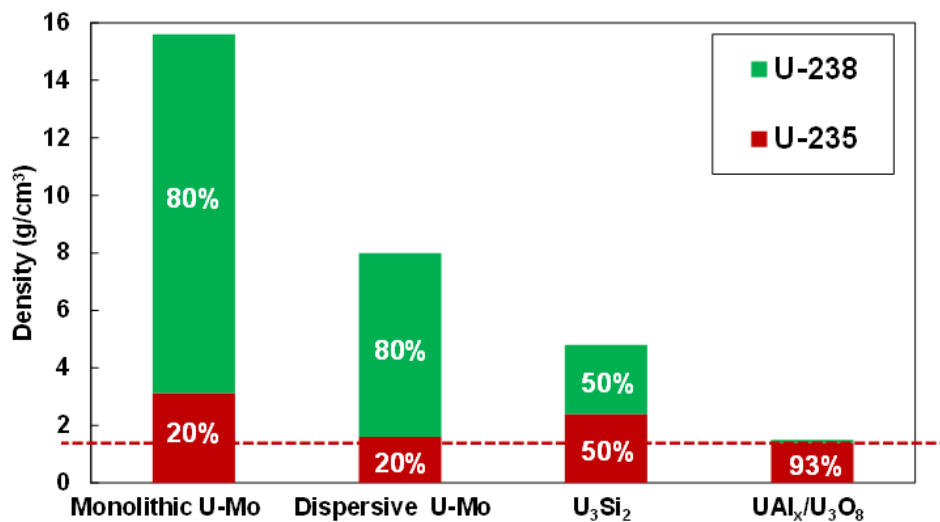


Figure 2. Effective densities of U in fuel systems for research reactor [51].

The swelled UMo fuel in contact with the Al-cladding can result in an adverse metallurgical reaction during irradiation [13, 14, 30, 31, 34-37]. Furthermore, fission gas bubbles can develop at the UMo/Al interface. In order to solve the problems, laminated Zr on UMo is being considered as an excellent diffusion barrier [39]. Several researchers have studied the U10Mo monolithic fuels in AA6061 cladding with a Zr diffusion barrier for microstructural development and kinetics by

varying fabrication parameters such as temperature and holding time.

Perez *et al.* [39] found a variety of phases at the interface between U10Mo and Zr as well as at the interface between Zr and AA6061 by TEM, as schematically summarized in Figure 3. The research also provided a thorough literature review regarding the relevant phase equilibria and diffusion for the U10Mo/Zr/AA6061 fuel plate system. The $\gamma\text{U}(\text{Mo})$, $\gamma\text{U}(\text{Zr})$, Zr solid solution and Mo_2Zr phases were observed at the interface between UMo and Zr. The $(\text{Al},\text{Si})_2\text{Zr}$, $(\text{Al},\text{Si})_3\text{Zr}$, $(\text{Al},\text{Si})\text{Zr}_3$ and AlSi_4Zr_5 phases were observed at the interface between AA6061 and Zr.

Jue *et al.* [46] evaluated the HIP-bonded monolithic fuels with Zr diffusion barriers. Grain structure and shape of decomposed UMo region (Eutectoid: $\gamma\text{U} \rightarrow \alpha\text{U} + \text{U}_2\text{Mo}$) depended on rolling direction. Mo_2Zr precipitates were formed by the Mo-depletion from the U10Mo alloy between UZr_2 and the U10Mo. Even though there was no extensive interaction at the edge of the cladding and none-Zr-coated fuel region, a very complex microstructure of Zr during fabrication of the Zr-laminated U-Mo coupon was formed by distortion or smearing.

Robinson *et al.* [16] reported results of tests and qualifications for monolithic fuel plates to find an optimized fabrication process. The U10Mo was recommended as the optimal alloy because of reduced swelling compared to U7Mo and U8 Mo alloys. In addition, U10Mo had excellent co-rolling properties with Zr laminate and resistance against decomposition during exposure to the heat-treatment. However, the destabilization of γU into Mo and αU can cause voids due to fission gas during irradiation. This occurred a few micrometers away from the interface which corresponds to the location where the αZr precipitates, αU and $\gamma\text{U}(\text{Mo})$ exist nearby.

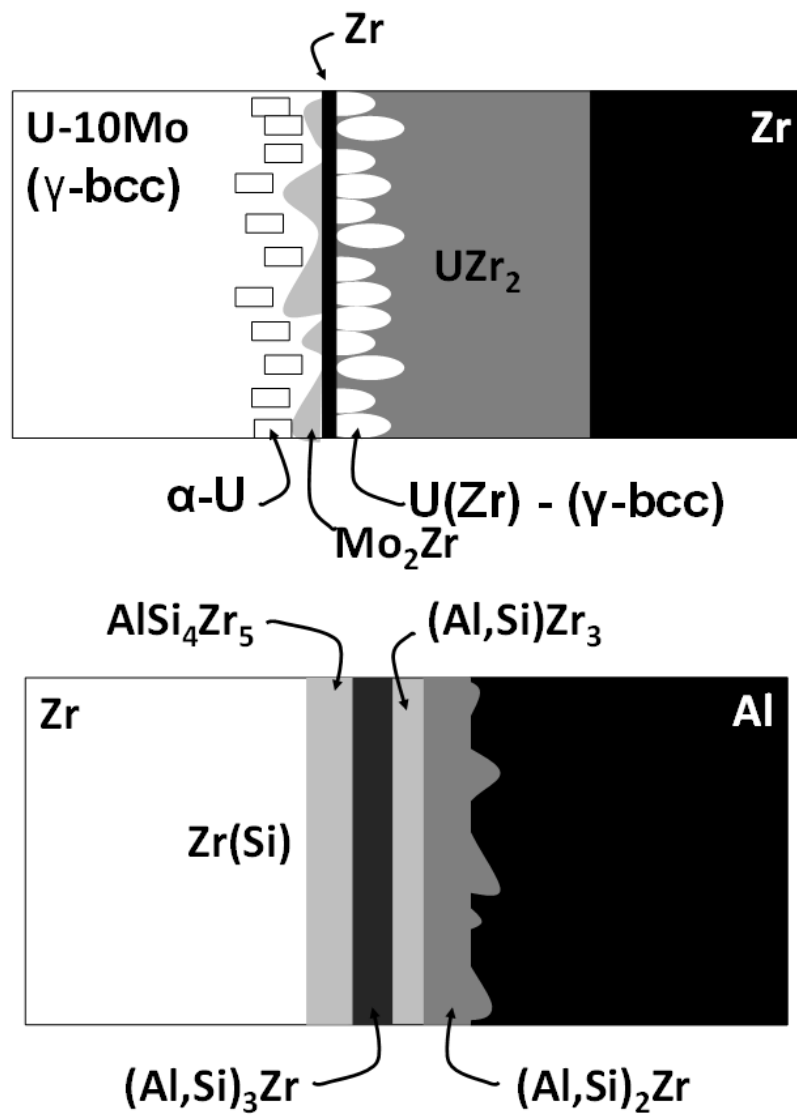


Figure 3. Schematic illustrations of phase constituents observed by Perez *et al.* [39] at the interface between the U10Mo monolithic fuel and Zr diffusion barrier, and at the interface between Zr diffusion barrier and AA6061 cladding alloy.

2.2. Allotropic transformation of U

Pure U exhibits two allotropic transformations, and thus three different crystal structures as shown in Figure 4. Orthorhombic α U, tetragonal β U and body-centered cubic (BCC) γ U are stable up to 667 °C, 667 ~ 771 °C and above 771 °C, respectively [52-54]. The α U has undesirable characteristics as a nuclear fuel such as low hardness, rapid oxidation, low corrosion resistance and anisotropic irradiation behavior [55-58]. A single crystal of α U shortens in a-axis and extends in b-axis, and there is no significant change in c-axis during irradiation under 500 °C [54, 59], leading to dimensional instability [60, 61].

In contrast, the γ U exhibits favorable properties as a nuclear fuel. The BCC γ U displays good dimensional stability because of isotropic expansion during irradiation [61]. The γ U also has a higher corrosion resistance to water, both liquid and vapor [62]. In order to retain the metastable γ U below 560 °C, rapid cooling or alloying additions has been employed [63, 64]. It is difficult for pure U to exist as γ U even after quenching because α U is thermodynamically favorable at low temperature [61, 63, 64]. Thus, alloying U with Me (Me = Mo, Nb, Zr, Ti, Re and etc.) has been adopted to stabilize the γ U and produce good irradiation behavior [65-67].

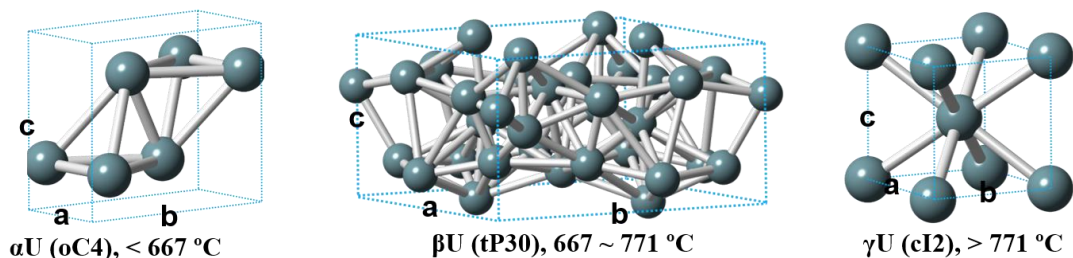


Figure 4. Allotropic crystal structures of α U, β U and γ U [68-70].

2.3. Composition of U-Mo alloy

The optimized U-Mo composition has to be considered to maximize the fuel performance in reactors. With the Mo content 8 wt.% or above, the γ U is stabilized even from slow cooling with acceptable uranium density for good irradiation behavior [52]. With the Mo content 6 wt.% or above, U-Mo alloy has displayed acceptable swelling behavior, and been delineated by tiny and uniformly distributed gas bubbles under irradiation condition [46]. U10Mo alloy is an excellent candidate for the development of fuel design because of its physical and mechanical properties during irradiation in reactors [46, 71]. U10Mo fuel has advantages such as excellent thermal conductivity and good compatibility for fabrication of fuel [71]. Furthermore, U10Mo has stable irradiation performance with metastable BCC γ U at room temperature.

2.4. Phase transformation of γ phase

The γ decomposition is affected by the Mo concentration in the alloy. The time temperature-transformation (TTT) diagram presented in Figure 5 [72] demonstrates that the decomposition is hindered by the Mo addition. Despite the sluggish kinetics, according to the equilibrium phase diagram, the high temperature γ U undergoes an eutectoid decomposition upon cooling to low-temperature orthorhombic α U and tetragonal γ' as shown in Figure 6 [42, 52, 73]. The equilibrium temperature of decomposition is relevant to the high temperature employed during co-rolling and HIP for the monolithic fuel system. Table 2 lists relevant properties of the γ U, α U and γ' . Generally, the microstructure related to the decomposition was observed first at γ U grain

boundaries [16, 65].

Figure 7 presents the TTT diagram that illustrates the time-dependent phase decomposition of the γ -phase in U10Mo alloy. The TTT diagrams of Repas *et al.* [63] and Peterson *et al.* [64] were constructed based on hardness, dilatometry, XRD and metallographic analyses. Saller *et al.* [74] also reported measurements of the electrical resistivity and hardness for U-21 at.% Mo alloy, indicating a structural transformation from BCC to an ordered body-centered tetragonal through isothermal transformation study at 500 °C. The transformation began approximately after 27 hours and completed at around 170 hours. It should be noted that a reverse decomposition, i.e., α and γ' into γ was observed during irradiation testing [75, 76].

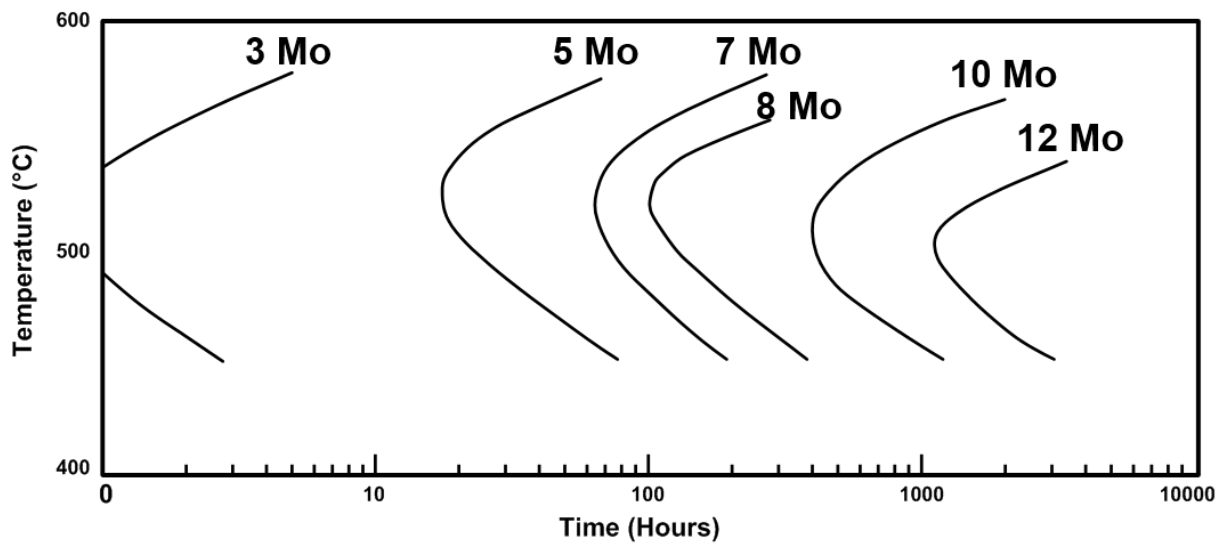


Figure 5. TTT diagram of U-Mo alloys as a function of Mo composition.

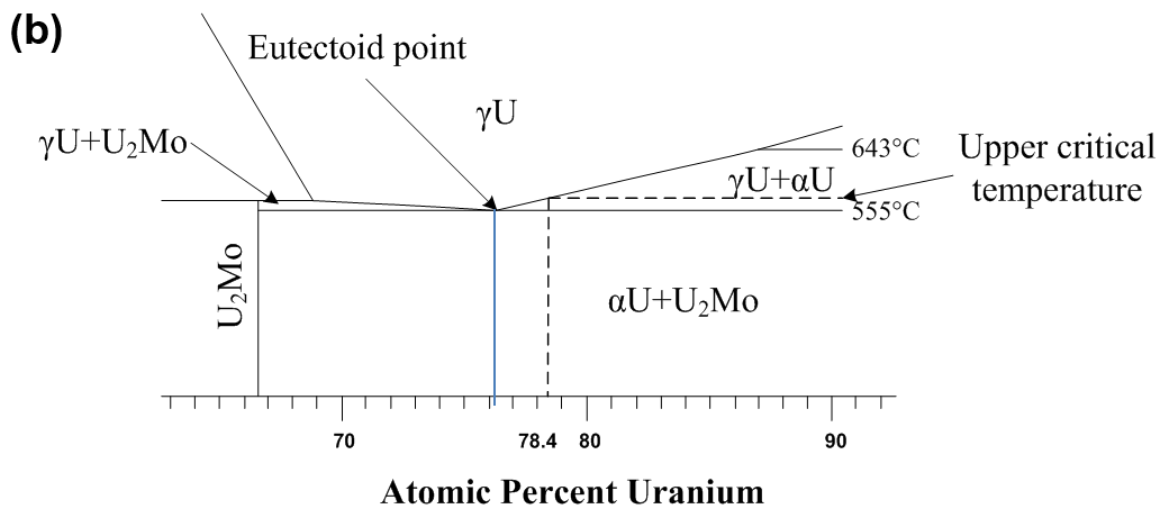
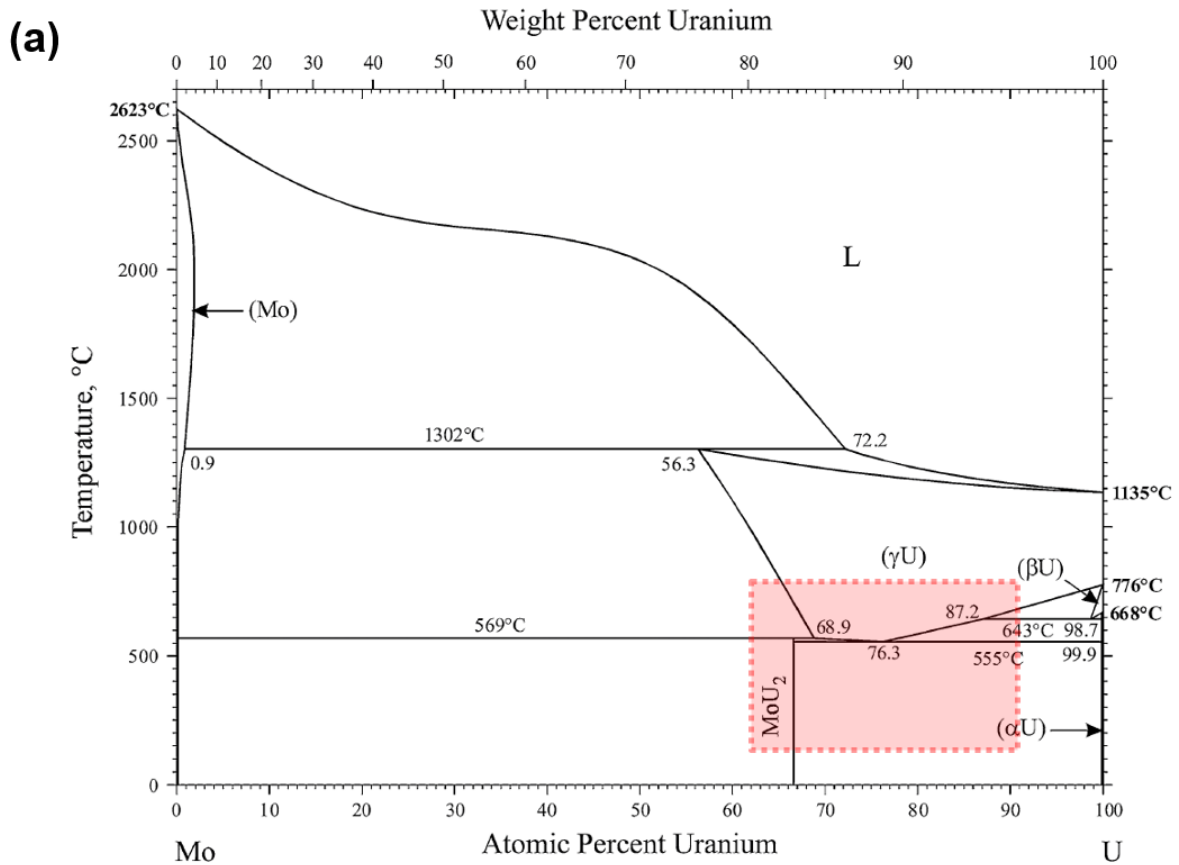


Figure 6. U-Mo equilibrium phase diagram for (a) overall feature and (b) magnified feature indicated by the dotted line [52].

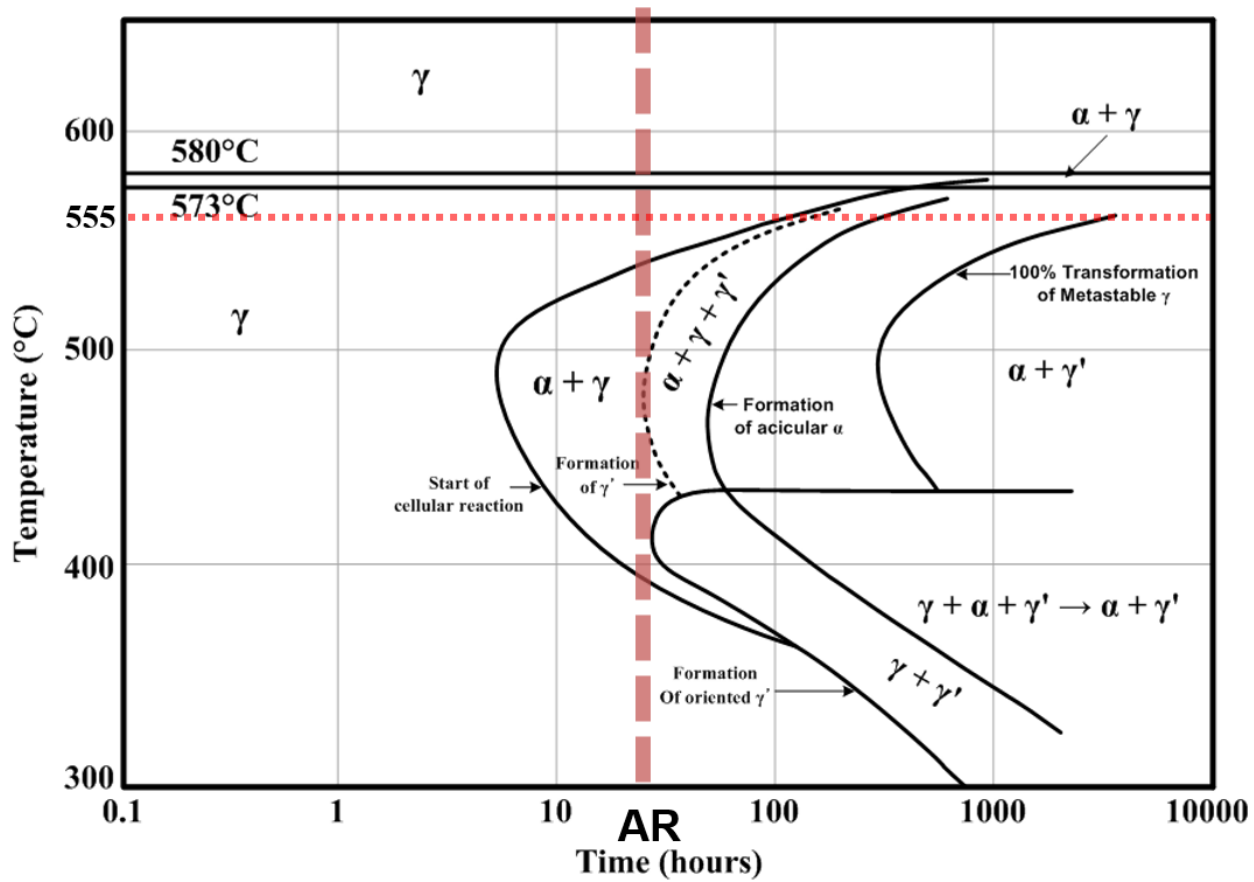


Figure 7. TTT diagram of U10Mo alloy [63].

Table 2. Properties for γ , α and γ' [4, 12, 52, 60, 73, 77-82].

Physical property	$\gamma(\text{U10Mo})$ (at 800 °C)	αU (at 627 °C)	$\gamma'(\text{U}_2\text{Mo})$ (at 500 °C)
Mo solubility (wt.%)	10	0.2	16
Strukturbericht designation	A2	A20	C11b
Prototype	W	αU	MoSi_2
Crystal structure	Body-centered cubic	C-centered orthorhombic	Body-centered tetragonal
Lattice parameter (Å)	a	3.474	2.854
	b	3.474	5.869
	c	3.474	4.955
Space group	Im3m (229)	Cmcm (63)	I4/mmm (139)
Pearson symbol	cI2	oC4	tI6
Young's modulus (GPa)	98	117	102
Hardness (GPa)	3.1	2.3	N/R
Poisson ratio	0.35	0.26	0.40
Thermal conductivity ($\text{Wm}^{-1}\text{K}^{-1}$)	3.65	34	N/R
Thermal expansion coefficient (10^{-6}K^{-1})	19.2	18.0	14.7
Specific heat ($\text{JK}^{-1}\text{g}^{-1}$)	0.194	0.192	0.154

2.5. U10Mo vs. Zr system

To examine the details of interdiffusion and reactions between the U10Mo fuel and Zr diffusion barrier, the analyses from diffusion couples have been carried out at temperatures between 600 and 1000 °C, in 100 °C increments by Huang *et al.* [43]. According to Huang *et al.* [43], a negligible amount (i.e., less than the resolution of scanning electron microscope) of U10Mo/Zr interactions occurred at 600 °C, while quantitative and qualitative analyses were carried out for couples annealed between 700 and 1000 °C based on definite diffusion interactions. According to Huang *et al.* [43], while the growth kinetics followed typical Arrhenius relation between 700 and 1000 °C, lack of interaction at 600 °C warranted a further investigation at temperature lower than 700 °C. Furthermore, from a MMMRC applications perspective, an understanding of interdiffusion and reactions at 650 °C is important, directly related to the co-rolling process, and starting microstructure for HIP.

CHAPTER 3: EXPERIMENTAL DETAILS

3.1. Laboratory facility

All alloys were continuously handled under an Ar atmosphere in a glove box shown in Figure 8(a) to minimize oxidation of U alloys and to prevent contamination of the laboratory facility. Figure 8(b) shows a schematic diagram of the Ar-gas flow. The inert atmosphere is maintained by Ar-gas injected into the glove box through an outlet. The Ar-gas exited the glove box through HEPA filter to trap potential airborne particles, and exhausted. The high vacuum system shown in Figure 9 was utilized for evacuating quartz capsules and flushing H₂-gas and Ar-gas to be presented in Section 3.2. The Lindberg/Blue™ three-zone tube furnace shown in Figure 10 was used to anneal at homogeneous temperatures for predetermined times to be presented in Section 3.2.

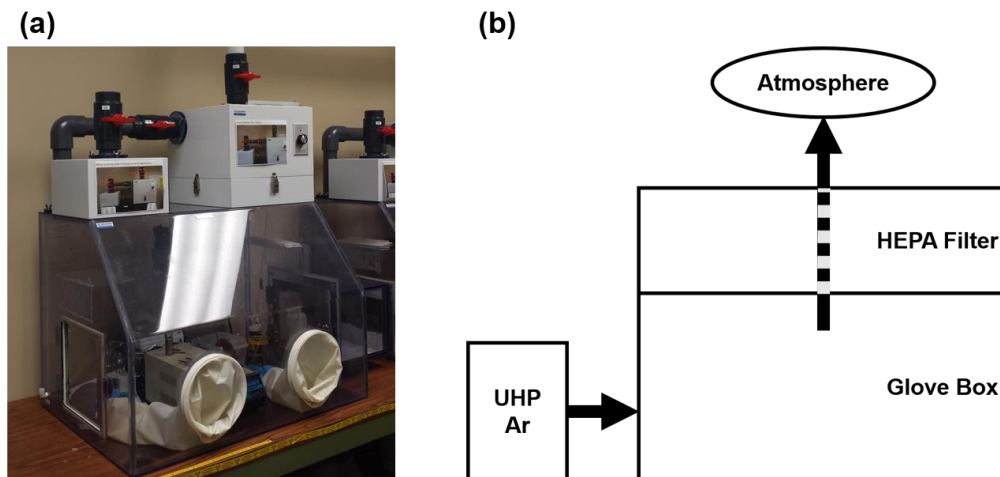


Figure 8. (a) Glove box under a controlled Ar atmosphere and (b) the schematic diagram of gas flow for alloy handling.

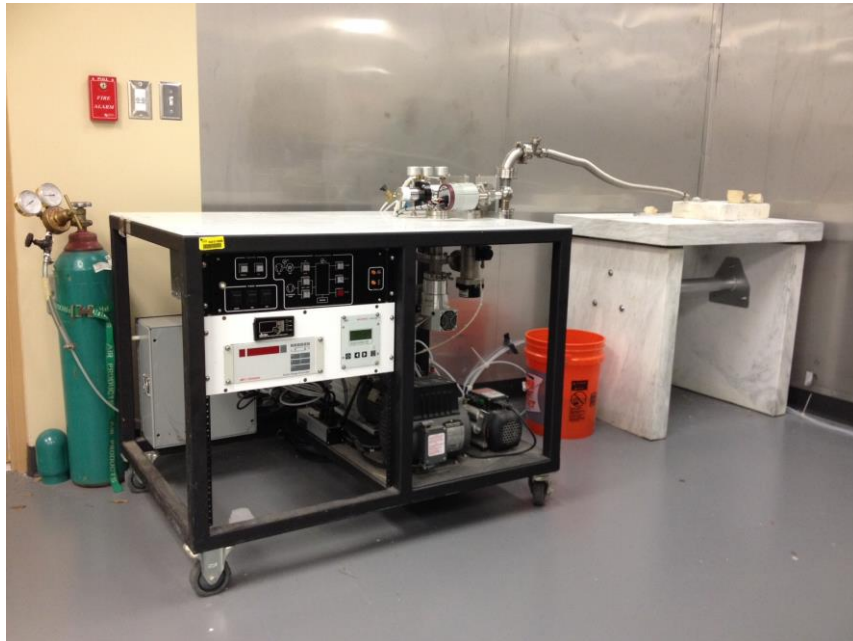


Figure 9. High vacuum system for evacuating quartz capsules.



Figure 10. Lindberg/Blue™ three-zone tube furnace.

3.2. Alloy preparation and diffusion experiment

All metallurgical preparation and assembly of diffusion couples were carried out under an Ar atmosphere inside a glove box to minimize oxidation of the alloys. The U, U10Mo and high-purity Zr (99.8%) were employed for the experiments. The U10Mo alloy was cast using high-purity depleted U and 99.95% Mo via arc melting at Idaho National Laboratory (INL). They were melted three times to ensure the homogeneity and then drop-cast to form rods with ¼ inch (6.35mm) diameters. The as-cast rods were then homogenized in an Ar atmosphere at 950 °C for 96 hours. The U and U10Mo were water-quenched after homogenization.

The U alloys and the commercial alloys were sectioned into disks of about 3mm in thickness, and the surface of disks designated to form diffusion interface were ground using silicon carbide papers (240, 600 and 800 grit) with ethanol as a lubricant for minimizing oxidation.

Figure 11 shows the U alloy vs. Zr diffusion barrier couples clamped by a steel jig with alumina spacers to prevent interaction between the diffusion couple disks and the steel jig set. The assembled diffusion couples were encapsulated in quartz capsules with a piece of Ta foil, and then were repeatedly flushed with H₂-gas and Ar-gas. The tubes were then sealed under vacuum ($\sim 10^{-6}$ torr) by using an oxygen-propane torch. Figure 11 shows diffusion couples before and after being sealed in quartz tubes. Each sealed couple was annealed in a Lindberg/Blue™ three-zone tube furnace at predetermined temperature and duration. After heat treatment, the diffusion couples were pulled out of the furnace and then immediately quenched by breaking the quartz capsule in cold water. The couples were then submerged for about 1 minute in water, and then the diffusion couples were extracted from the quartz capsule. The quenched diffusion couples were then

mounted in epoxy and cross-sectioned for metallographic sample preparation.

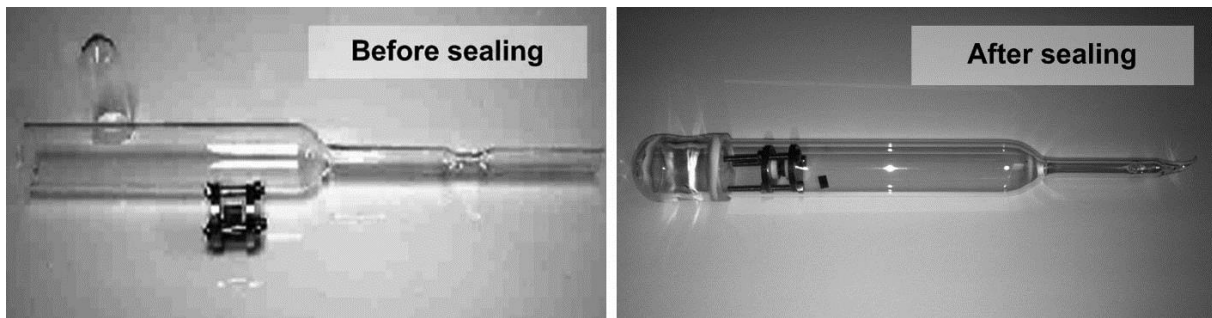


Figure 11. Quartz capsules for heat treatment of diffusion couples.

3.3 Fabrication of HIP monolithic fuel plate at INL

The U10Mo alloy was cast into a coupon shaped ingots using a graphite mold. The alloy coupon had an approximate dimension of 88.8 mm x 48.9 mm x 3.2 mm. The carbon content of this alloy coupon was more than 700 ppm. This ingot was first acid cleaned using a mixture of nitric and hydrofluoric acid (2.5% HF, 35% HNO₃ and 62.5% H₂O) and then laminated, in a carbon steel can, using pure Zr (99.9% pure) foil with approximate starting thickness of 250 μ m, on each surface. The Zr-laminated U10Mo coupon was pre-heated at 650 °C for 30 minutes in a furnace, and then co-rolled 15 times to a thickness of approximately 0.46 mm. A post-rolling annealing treatment was performed at 650 °C for 45 minutes. The hot-rolled/annealed foil was then removed from the can, and cold-rolled to the final thickness of 0.33 mm. This thickness includes the Zr diffusion barrier layer on each surface. The dimensions of the final as-rolled foil was 74.6 cm x

6.54 cm x 0.033 cm. The total time exposure at 650 °C was estimated to be approximately 130 minutes. The final thickness of the Zr diffusion barrier was approximately 25 micrometers. The final as-rolled U-Mo foil was then sheared into mini-size foils. All the U-Mo mini-sized foils used in this study were sheared from the same full-size foil. Each mini foil is expected to represent the microstructure of the co-rolled U-10Mo foil with Zr. The as-rolled/sheared sample before the HIP process, labeled sample AR, was examined in this study as listed in Table 3. A schematic illustration of co-rolling is presented in Figure 12.

Table 3. List of monolithic fuel plate assemblies examined as functions of temperature, time and ramp-cool rate of HIP under 103 MPa (~15 ksi).

HIP #	Temperature. (°C)	Hold Time (minute)	Ramp-cool Rate (°C/hour)
AR	N/A	N/A	N/A
52-90-280	520	90	280
54-90-280	540	90	280
56-90-280	560	90	280
58-90-280	580	90	280
56-45-280	560	45	280
56-60-280	560	60	280
56-180-280	560	180	280
56-345-280	560	345	280
56-90-35	560	90	35
56-90-70	560	90	70

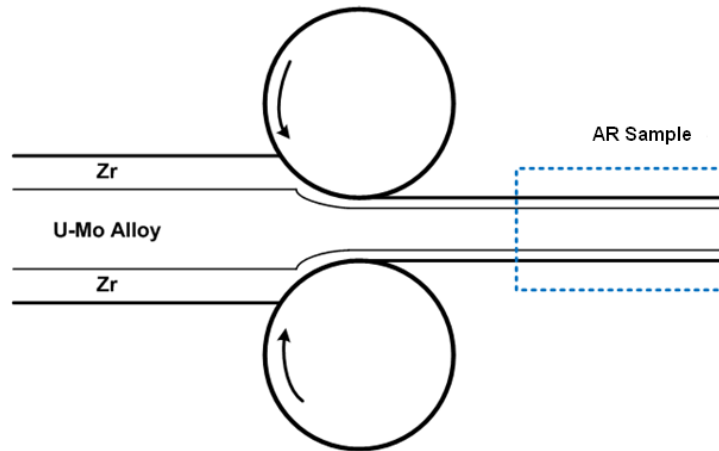


Figure 12. A schematic illustration of co-rolling employed in this investigation to produce U10Mo monolithic fuel encased in AA6161 with Zr diffusion barrier.

Each U10Mo/Zr mini foil was polished and stacked with AA6061 (in wt.% nominal composition of 0.6Si-0.35Fe-0.28Cu-0.08Mn-1.0Mg-0.20Cr-0.13Zn-0.08Ti-Al balance) cladding pieces, and HIP'ed at various temperatures (520, 540, 560 and 580 °C) and durations (45, 60, 90 180 and 345 minutes) with ramp-cool rates (35, 70 and 280 °C/hour) as listed in Table 3. Prior to HIP'ing, the AA6061 cladding was etched using 1.85 M NaOH rinse, followed by pickling using 30% nitric acid in order to remove the residual oxide scale on the Al alloy. The U10Mo/Zr/AA6061 assemblies were inserted into stainless steel HIP cans with tool steel strong-backs that were welded, with corners open for degassing, in an argon atmosphere glove box. The samples were then leak checked and vacuum de-gassed at 315°C for 3 hours. The HIP can was then loaded into a laboratory-size HIP, and heated to the target temperature with a ramp-cool rate. The isostatic pressure of HIP was kept constant at 103 MPa (~15 ksi), and argon was used as the pressurizing medium. Figure 13 shows a schematic of the HIP processing.

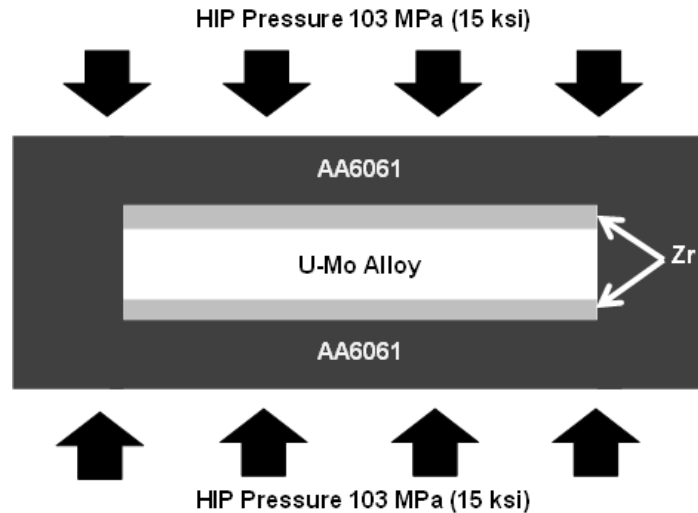


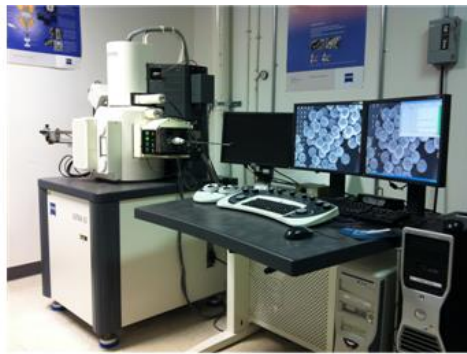
Figure 13. A schematic diagram of HIP.

3.3 Characterization

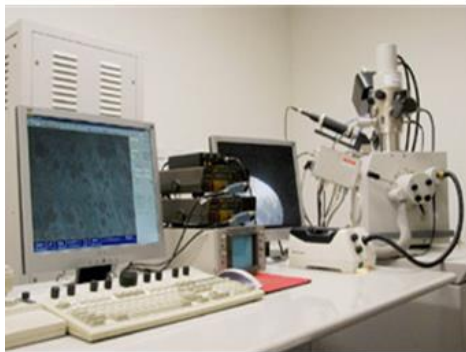
The samples were cross-sectioned and mounted in epoxy. The mounted fuel plates were ground using silicon carbide papers (240, 600, 800 and 1200 grit) with an ethanol lubricant. Subsequently diamond pastes (3 and 1 μ m) with an oil lubricant were used for final polishing in a glove box under Ar atmosphere to prevent oxidation and contamination.

For each diffusion couple, SEM (Zeiss ULTRA-55 FEG SEM) with an accelerating voltage of 20.0 kV was used to examine the quality of diffusion bonding and the thickness of the reaction layer. BSE and SE micrographs were employed to observe metallurgical microstructures. EDS was utilized for the semi-quantitative compositional analysis. A point-to-point counting measurement technique and ZAF correction were employed to determine compositional variation. TEM

(FEI/Tecnai™ F30) equipped with a HAADF detector (Fischione™) and XEDS was used to examine the detailed microstructure of the interdiffusion zone. SEM, FIB and TEM instruments are presented in Figure 14. Samples were prepared by FIB (FEI TEM200) as presented in Figure 15 for transmissions of electrons to be examined by TEM. SAED patterns were collected from selected regions of HAADF images, DF images and BF images to carry out crystallographic identification of intermetallic phases. In order to index the diffraction patterns, Digital Micrograph™, Microsoft Excel™, Microsoft Visual Studio™ and Photoshop™ were used.



(a)

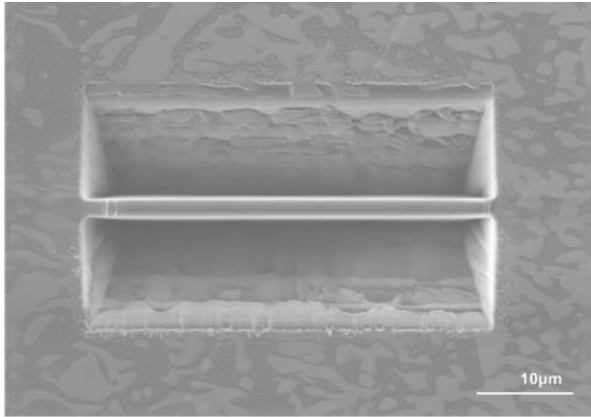


(b)

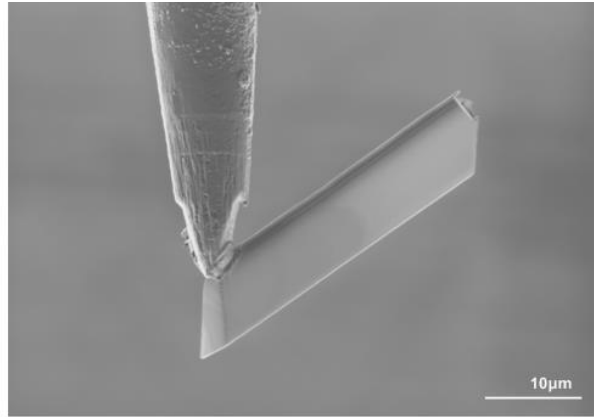


(c)

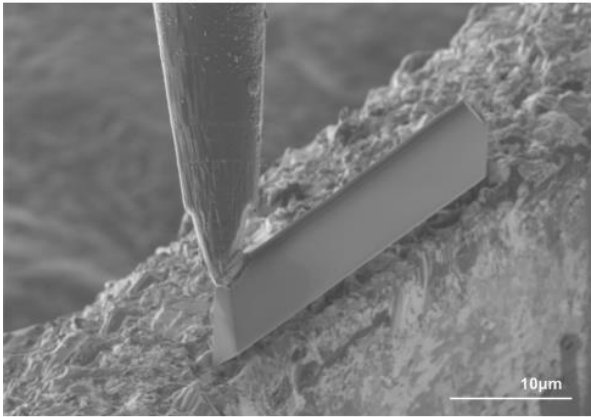
Figure 14. (a) Zeiss ULTRA-55 FEG SEM (b) FEI TEM200 FIB (c) FEI TECNAI F30 TEM.



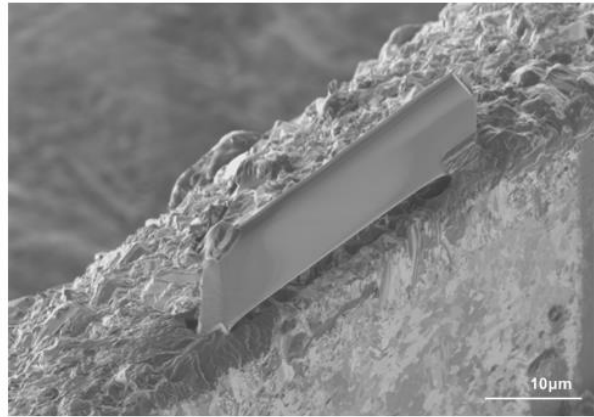
(a)



(b)



(c)



(d)

Figure 15. FIB sample preparation: (a) initial milling completion (b) in-situ lift-out (c) insertion of sample onto the pre-slotted Cu-grid (d) welding the sample on Cu-grid.

CHAPTER 4: ANALYTICAL FRAMEWORK

4.1. Time-dependent growth and Arrhenius relationship

The flux of diffusion is a reciprocal proportion to a layer thickness in a diffusion-controlled process and can be [83] written as:

$$\frac{dx}{dt} \propto \frac{1}{x} \quad (1)$$

$$\frac{dx}{dt} = k \frac{1}{x} \quad (2)$$

where x is the thickness of layer, t is the time and k is a constant. Equation (2) can be modified by integration from beginning annealing time ($t = 0$ and $x = 0$) to after annealing time ($t = t_l$ and $x = x_l$) as:

$$k_p = \frac{x^2}{2t} \quad (3)$$

where k_p is the parabolic growth constant. As the equations describe, growth of thickness increases with an increase annealing time. Generally, growth and diffusion rates increase as annealing temperature increases. The thermally activated systems can be described by the Arrhenius expression:

$$k_p = k_0 e^{-\frac{Q_k}{RT}} \text{ or } D = D_0 e^{-\frac{Q_D}{RT}} \quad (4)$$

where k_0 (and D_0) is the pre-exponential factor, Q_k (and Q_D) is the activation energy, R is the molar gas constant of 8.314 J/mol-K and T is the absolute temperature.

4.2. Molar volume and Vegard's law

Composition in fraction of a binary alloy can be expressed by:

$$C_i + C_j = 1 \quad (5)$$

where C_i and C_j are the compositions given by atomic fractions of element i and j . The molar volume of a phase can be written as:

$$v_m = \frac{v_{cell}}{n_i} N_{avo} \quad (6)$$

where v_{cell} is the volume of the unit cell calculated from lattice parameters, n_i is the atomic number, and N_{avo} is the Avogadro number ($6.023 \times 10^{23} \text{ mol}^{-1}$). The ideal deviation of molar volume as a function of composition follows the Vegard's law defined as:

$$v_m = C_i v_m^i + C_j v_m^j \quad (7)$$

where v_m^i and v_m^j are the partial volumes of element i and j .

4.3. Boltzmann-Matano analysis

The Boltzmann-Matano analysis solved Fick's second law of nonlinear partial differential equation with a mass balance, Matano plane, and this analysis has been utilized to estimate the interdiffusion coefficients at specific compositions from a concentration profile under the condition that the partial molar volumes for the interdiffusion phases remain constant [84, 85]. The Fick's second law is expressed as:

$$\frac{\partial C_i}{\partial t} = D \frac{\partial^2 C_i}{\partial x^2} \quad (8)$$

where C_i is the concentration of component i .

The interdiffusion flux, \tilde{J}_i [86], can be calculated with the Matano plane as:

$$\tilde{J}_i = \frac{1}{2t} \int_{c_i^{\pm\infty}}^{c_i} x dC_i = \frac{1}{2t} \int_{c_i^{\pm\infty}}^{c_i^0} (x - x_0) dC_i \quad (9)$$

where $C_i^{-\infty}$ and $C_i^{+\infty}$ are the concentration at terminal ends, C_i^0 is the concentration at the Matano plane and x_0 is the location of Matano plane. The interdiffusion coefficient of a component, \tilde{D}_i can be expressed after applying Fick's first law, $\tilde{J}_i = -\tilde{D} \left(\frac{\partial C_i}{\partial x} \right)$ as:

$$\tilde{D} = - \frac{\frac{1}{2t} \int_{C_i^{\pm\infty}}^{C_i^0} (x - x_0) dC_i}{\frac{\partial C_i}{\partial x}} \quad (10)$$

The interdiffusion coefficient can be rewritten at the selected point, x^* , with the concentration, C_i^* , for the left-hand side of the Matano plane as:

$$\tilde{D}(C_i^*) = -\frac{1}{2t} \left(\frac{dx}{dC_i} \right)_{C_i^*} \left[x^*(C_i^* - C_i^{-\infty}) - \int_{x^{-\infty}}^{x^*} (C_i - C_i^{-\infty}) dx \right] \quad (11)$$

4.4. Sauer-Freise with Wagner analysis

As stated above, the Boltzmann-Matano analysis is valid for a system with negligible change in molar volume. The Sauer-Freise analysis generalized the Boltzmann-Matano analysis for systems having the deviated molar volume. The Sauer-Freise analysis with Wagner approach should be utilized to determine the integrated interdiffusion coefficient for an intermetallic phase with negligible concentration gradient [87, 88]. The normalized concentration variable, Y_i , can be written as

$$Y_i = \frac{C_i - C_i^{-\infty}}{C_i^{+\infty} - C_i^{-\infty}} \quad (12)$$

Then, the interdiffusion flux can be calculated as:

$$\tilde{J}_i(Y_i^*) = \frac{V_m^*}{2t} (C_i^{+\infty} - C_i^{-\infty}) \left[(1 - Y_i^*) \int_{x^{-\infty}}^{x^*} \frac{Y_i}{V_m} dx + Y_i^* \int_{x^*}^{x^{+\infty}} \frac{1 - Y_i}{V_m} dx \right] \quad (13)$$

where V_m is the molar volume and Y_i^* is the normalized concentration variable at the selected location. The interdiffusion coefficient can be calculated as:

$$\tilde{D}(Y_i^*) = \frac{V_m^*}{2t \left(\frac{dY_i}{dx} \right)_{x^*}} \left[(1 - Y_i^*) \int_{x^{-\infty}}^{x^*} \frac{Y_i}{V_m} dx + Y_i^* \int_{x^*}^{x^{+\infty}} \frac{1 - Y_i}{V_m} dx \right] \quad (14)$$

The integrated interdiffusion coefficient for a stoichiometric composition can be written as:

$$\begin{aligned}
\tilde{D}(Y_i^*) = & \frac{(C_i^* - C_i^{-\infty})(C_i^{+\infty} - C_i^*) \Delta x_i^2}{C_i^{+\infty} - C_i^{-\infty}} \frac{1}{2t} \\
& + \frac{\Delta x_i}{2t} \left[\frac{C_i^{+\infty} - C_i^*}{C_i^{+\infty} - C_i^{-\infty}} \int_{x^{-\infty}}^{x^*} \frac{V_m^*}{V_m} (C_i - C_i^{-\infty}) dx \right. \\
& \left. + \frac{(C_i^* - C_i^{-\infty})}{C_i^{+\infty} - C_i^{-\infty}} \int_{x^*}^{x^{+\infty}} \frac{V_m^*}{V_m} (C_i^{+\infty} - C_i) dx \right]
\end{aligned} \tag{15}$$

where Δx_i is the thickness of selected stoichiometric phase.

4.5. Heumann analysis

The difference of intrinsic fluxes between elements in a binary system can cause the movement of Kirkendall marker plane (x_m) with respect to the laboratory fixed frame as shown Figure 16. If the intrinsic flux of element i is larger than that of element j , the marker plane moves to the i -rich side from the initial contact interface x_0 . The composition of marker plane is constant. The accumulated intrinsic flux, $A_i = -2tD_i \left[\frac{\partial C_i}{\partial x_m} \right]$, can be modified to calculate the intrinsic diffusion coefficient, D_i written as:

$$D_i = - \frac{A_i}{2t \left[\frac{\partial C_i}{\partial x_m} \right]} \tag{16}$$

The relationship between and intrinsic diffusion coefficients can be demonstrated by Darken

equation presented as:

$$\tilde{D} = C_i D_j + C_j D_i \quad (17)$$

The Darken equation can be used under the isothermal and isobaric conditions with the constant molar volume such as $v_m = v_i = v_j$.

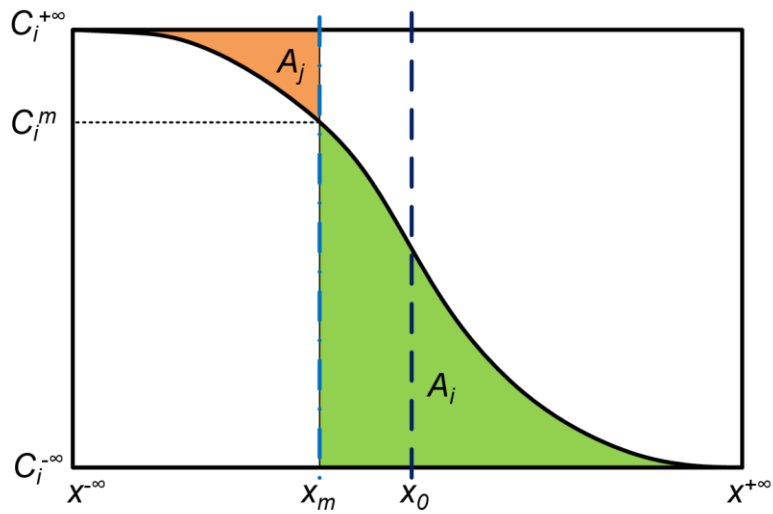


Figure 16. Concentration profile to explain the Huemman's analysis for determination of the intrinsic diffusion coefficients

CHAPTER 5: U10Mo vs. Zr DIFFUSION COUPLES

5.1. Background

The U-Mo alloys, typically containing 8 to 12 wt.% Mo for the MMMRC program applications, can undergo complex interdiffusion and reactions in contact with Al matrix or cladding, which can produce various phases with rapid growth kinetics [29-31, 35] and undesirable irradiation behavior [13-15]. In monolithic fuels, AA6061, with nominal composition of, in wt.%, Al-1.0Mg-0.6Si-0.7Fe-0.25Zn-0.2Cu-0.2Cr-0.15Mn-0.15Ti, is commonly used to encase the U-Mo fuel to provide structural stability and to isolate the fuel. Interactions between the U-Mo and AA6061 take place at high temperature (450 ~ 650 °C) during fuel plate manufacturing, and at lower temperature in reactor (well below 300 °C), however with irradiation-enhancement.

To reduce the overall kinetics and complexity of this diffusion interaction, Zr can be used as a diffusion barrier between the U-Mo fuel and AA6061 cladding [16, 38, 43]. Consequently, however, interdiffusion and reactions can occur between U-Mo and Zr, as well as Zr and AA6061 during the fuel plate fabrication. Typically, these monolithic fuels are produced by the repeated co-rolling of Zr-laminated U-Mo fuel at soaking temperature reaching up to 650 °C, followed by hot-isostatically pressing (HIP'ing) with AA6061 cladding at temperature ranging from 520 to 580 °C. During co-rolling, it is estimated that the Zr laminated U-Mo fuel is exposed to the highest temperature of 650 °C for approximately 2 to 3 hours.

In this study, the phase constituents and the growth of the interaction zone that develop between the U10Mo alloys and Zr at the co-rolling soaking temperature of 650 °C were examined as a function of time using solid-to-solid diffusion couples. The couples were annealed at 650 °C

for 240, 480 and 720 hours to develop interaction regions with phase constituents.

5.2. Experimental Parameters

U10Mo vs. Zr diffusion couples were annealed at 650 °C

1. for 240, 480 and 720 hours followed by water quenching
2. for 480 hours followed by furnace-cooling

5.3. Results

5.3.1. Phase constituents and microstructure

Typical backscatter electron (BSE) micrographs from the U10Mo vs. Zr diffusion couples annealed at 650 °C are presented in Figure 17. Figure 17 (a), (b) and (c) are the BSE micrographs from water-quenched diffusion couples that were annealed for 240, 480, 720 hours, respectively. Figure 17 (d) is the BSE micrographs from the diffusion couples annealed for 480 hours and furnace cooled. The interdiffusion and reaction in these couples resulted in similar microstructure and phase constituents. Based on BSE micrographs and XEDS analyses, phase constituents such as γ U(Mo) solid solution (cI2), needle-like α Zr (hP2) precipitates, Mo₂Zr (cF24), bcc β Zr (cI2), and α Zr (hP2) were identified as labeled in Figure 17.

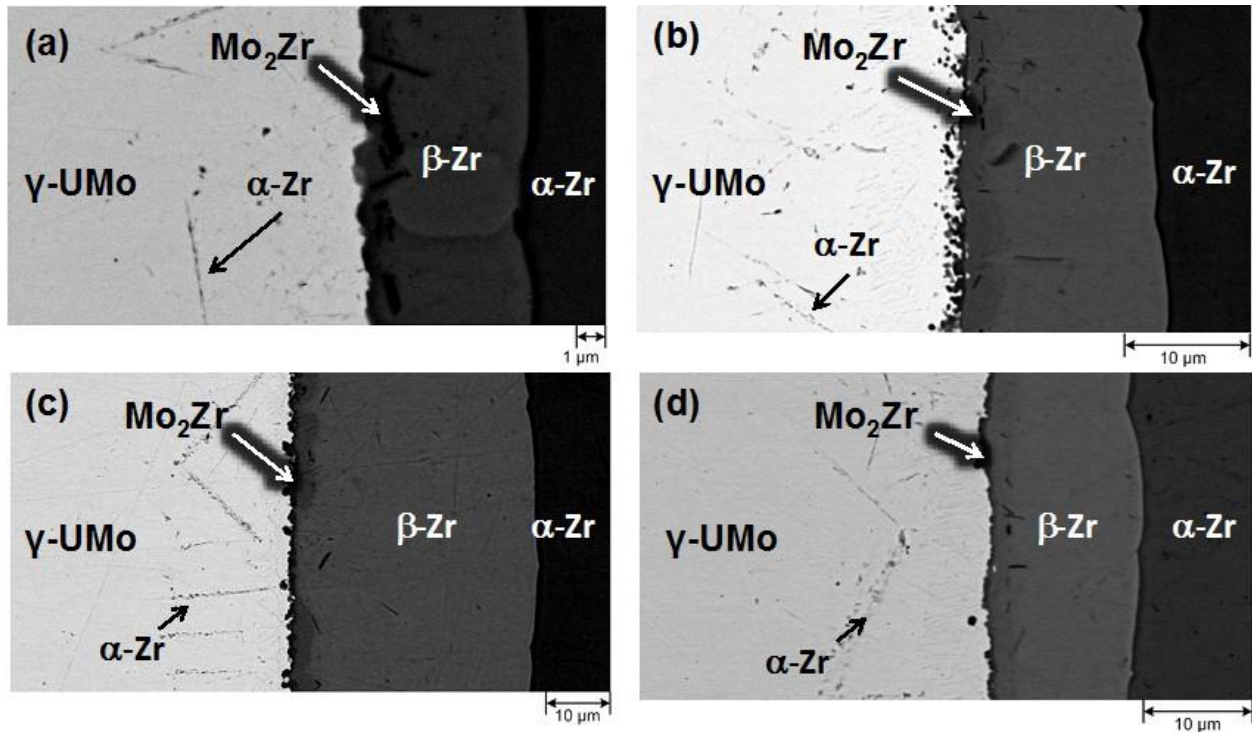


Figure 17. Backscattered electron micrographs from U10Mo vs. Zr diffusion couples annealed at 650 °C for (a) 240, (b) 480 and (c) 720 hours followed by water-quench, and (d) for 480 hours followed by furnace-cooling.

Figure 18 presents a HAADF scanning STEM micrograph from the region near the interface between the $\gamma\text{U}(\text{Mo})$ solid solution and βZr layer, where the discontinuous Mo_2Zr layer, needle-shaped αZr precipitates, blocky $\text{U}_6\text{Zr}_3\text{Mo}$ precipitates, and βU layer were observed. Based on fast-Fourier transformation (FFT) of high-resolution TEM (HR-TEM) micrograph, from region (1) in Figure 18, the needle-shaped Zr precipitates were identified as αZr (hP2) surrounded in a matrix of $\gamma\text{U}(\text{Mo})$ as presented in Figure 19. Figure 20 shows the SAED patterns collected from the region 2 in Figure 18 corresponding to the layers of βZr , Mo_2Zr and βU . Occasionally within the βU layer, small precipitates of αZr (hP2) were also observed as presented in Figure 21.

Formation of the Mo_2Zr phase would deplete the Mo content from the U10Mo alloy, and can destabilize the $\gamma\text{U}(\text{Mo})$ solid solution into the βU with limited solubility for Zr. This would promote the formation of αZr precipitates upon cooling near the interface between the $\gamma\text{U}(\text{Mo})$ solid solution and βZr layer since a two-phase equilibrium between the $\gamma\text{U}(\text{Mo})$ and αZr does not exist at 650 °C.

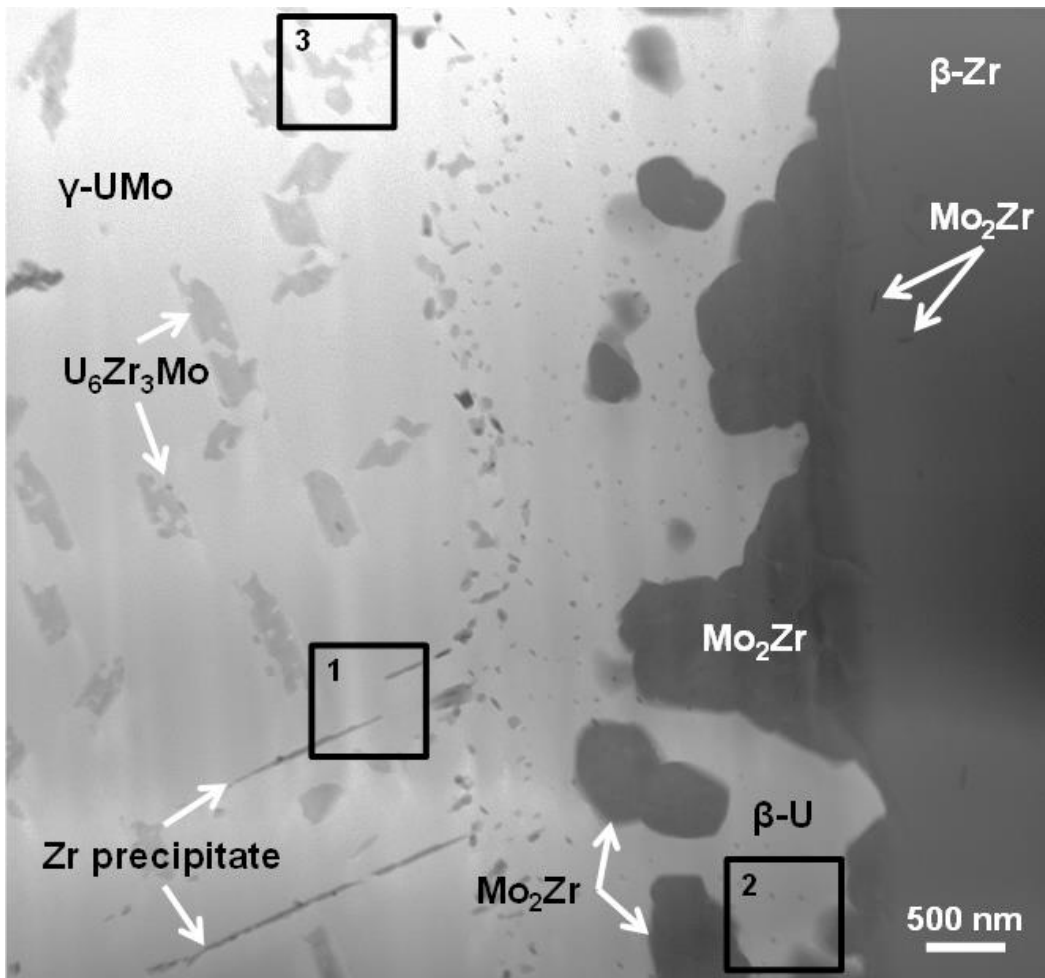


Figure 18. High angle annular dark field micrographs from the water-quenched U10Mo vs. Zr diffusion couple annealed at 650 °C for 720 hours.

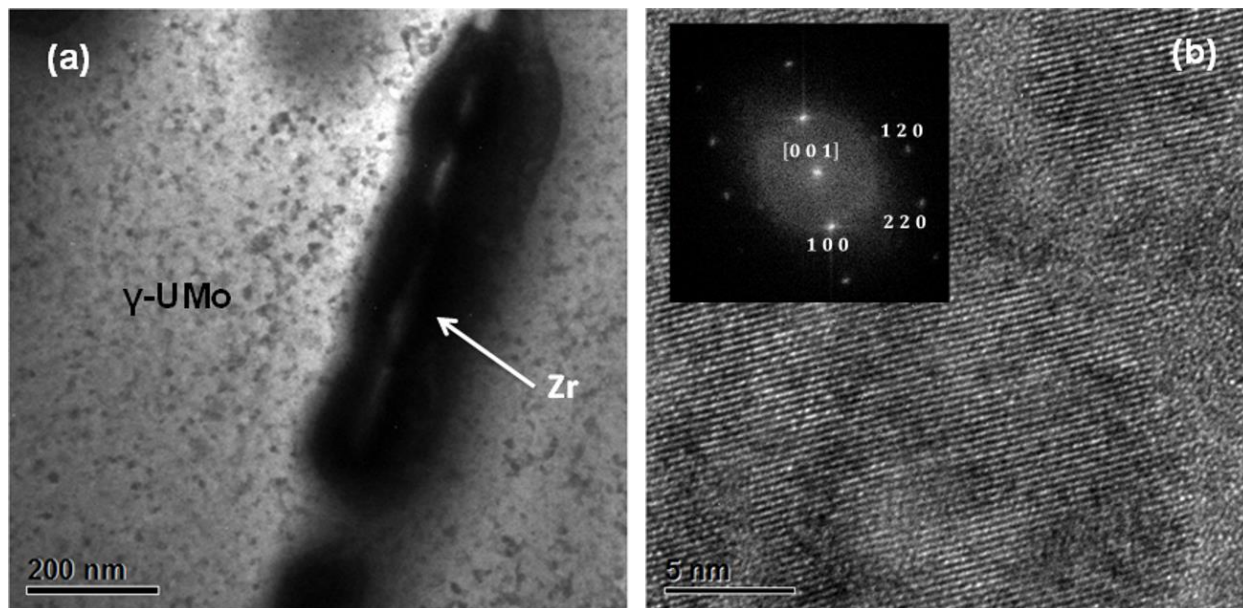


Figure 19. From region (1) in Figure 18: (a) Bright field and (b) high-resolution TEM micrographs with the fast Fourier transformation analysis of needle-shaped α Zr precipitate in the water-quenched U10Mo vs. Zr diffusion couples annealed at 650 °C for 720 hours.

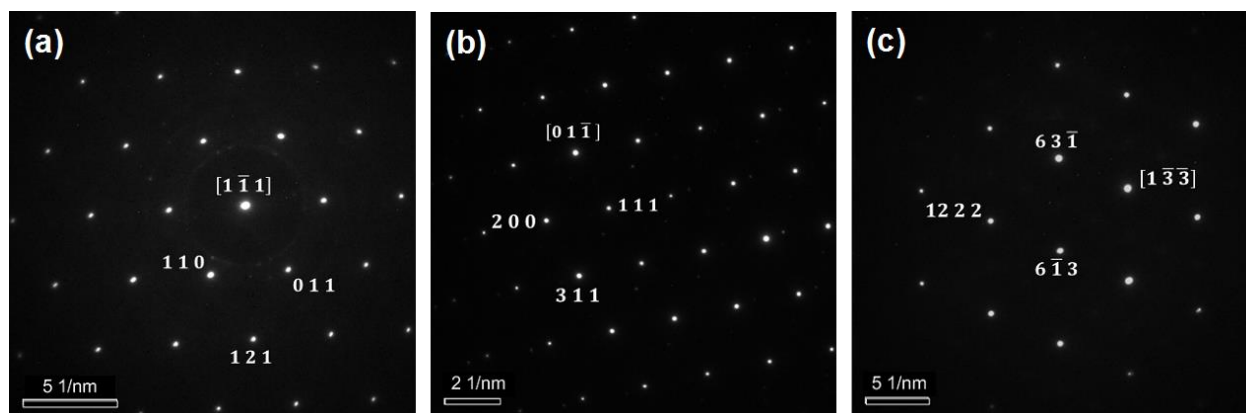


Figure 20. From region (2) in Figure 18: selected area electron diffraction patterns from the (a) β Zr, (b) Mo_2Zr and (c) β U layers observed in the water-quenched U10Mo vs. Zr diffusion couples annealed at 650 °C for 720 hours.

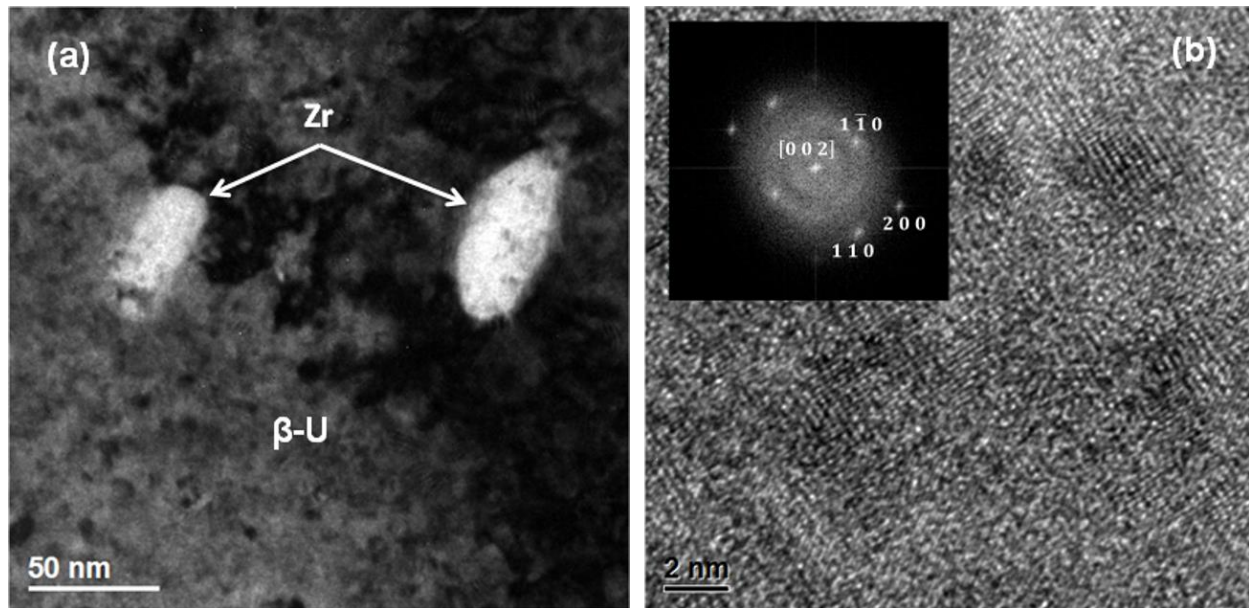


Figure 21. From region (2) in Figure 18: (a) dark field and (b) high-resolution TEM micrographs of the α Zr precipitates observed within the β U layer formed in the water-quenched U10Mo vs. Zr diffusion couples annealed at 650 °C for 720 hours.

Aside from the stable Mo_2Zr and βZr phases, the microstructural development and phase formation presented can be a result of cooling after diffusion anneal. For example, analysis of blocky precipitates in region 3 of Figure 18 confirmed the presence of $\text{U}_6\text{Zr}_3\text{Mo}$ phase as presented in Figure 22. The $\text{U}_6\text{Zr}_3\text{Mo}$ phase, according to the ternary phase diagrams, should form at lower temperature during cooling. Figure 23 summarizes the phase constituents and microstructural development observed between the $\gamma\text{U}(\text{Mo})$ solid solution and βZr layer in this study from the diffusion couples annealed at 650 °C. Table 4 lists crystallographic information on phases identified within the interaction zone in this investigation. No significant variation in phase constituents was observed as a function of anneal time or cooling rate. Onset of void formation during irradiation has been presented [16] few micrometers away from the fuel/barrier interface.

Based on observation in this study, this location can correspond to the presence of U_6Zr_3Mo and needle-shaped αZr , and/or the interface between the $\gamma U(Mo)$ and βU . Furthermore, the presence of βU (possibly αU with anneal at lower temperature of 520–580 °C during subsequent HIP'ing) may adversely affect the irradiation behavior of the bonding between the U10Mo fuel and Zr diffusion barrier. Previous works [39, 46, 89] has noted several changes in the phase constituents including the presence of UZr_2 , after secondary anneal at lower temperature, with or without pressure, relevant to HIP (520-580 °C), after the initial anneal at higher temperature (e.g., 650 °C).

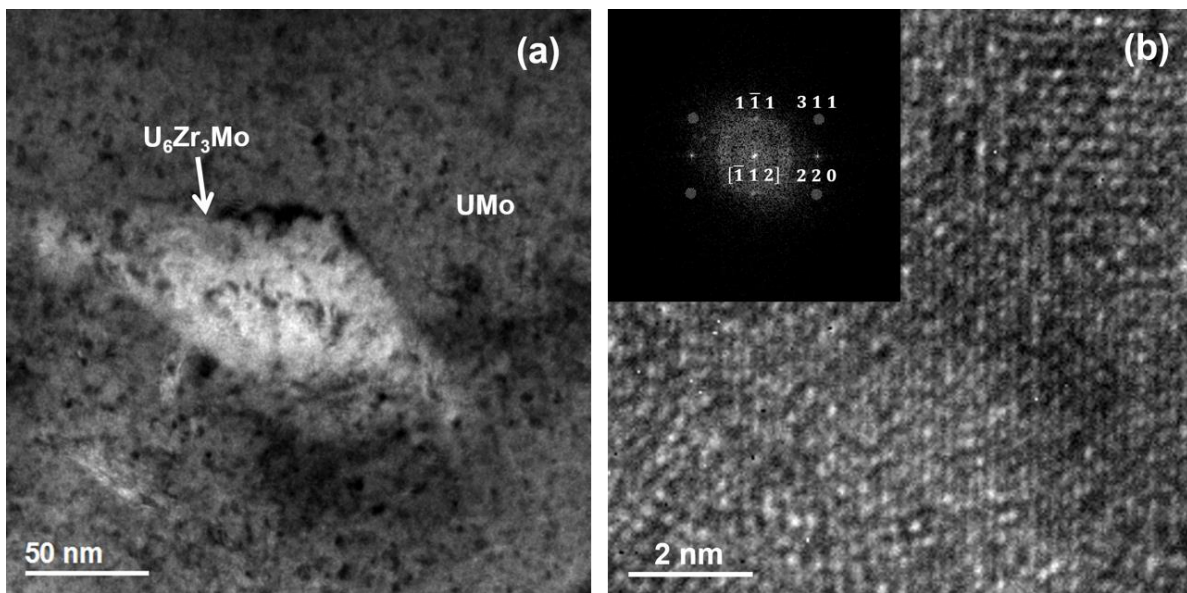


Figure 22. From region (3) in Figure 18: (a) dark field and (b) high-resolution TEM micrographs with the fast Fourier transformation analysis of U_6Zr_3Mo precipitate within the U - Mo matrix from the water-quenched U10Mo vs. Zr diffusion couples annealed at 650 °C for 720 hours.

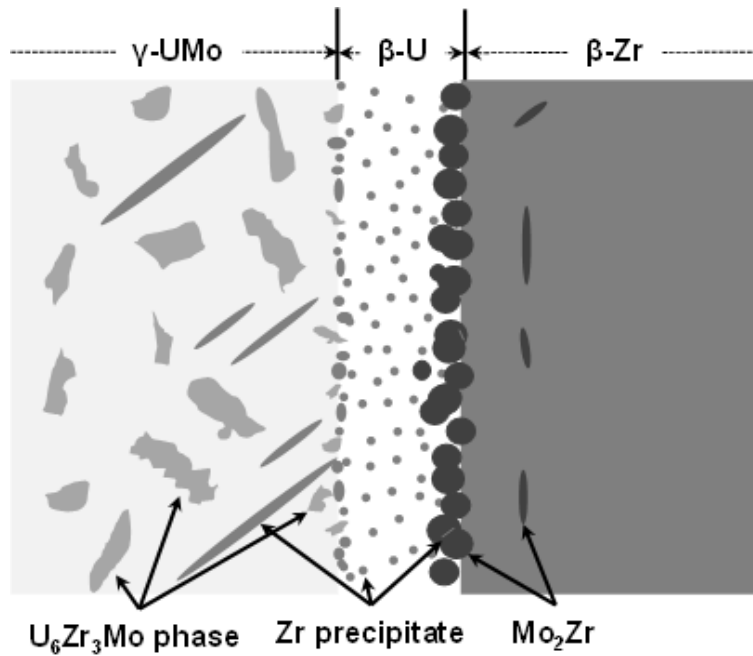


Figure 23. Schematic diagram of the interaction layers from the water-quenched U10Mo vs. Zr diffusion couple annealed at 650 °C for 720 hours.

Table 4. Crystallographic information on relevant phases of this investigation.

Phase	Pearson Symbol	Space Group
γ U(Mo)	cI2	Im3m
β U	tP30	P42/mnm
Mo ₂ Zr	cF24	Fd3m
β Zr	cI2	Im3m
α Zr	hP2	P63/mmc
U ₆ Zr ₃ Mo	cFX	Fm3m

5.3.2. Concentration profiles and diffusion paths

A concentration profiles from the U10Mo vs. Zr diffusion couple, annealed at 650 °C is presented in Figure 24, from the couple that was annealed for 720 hours and water-quenched. These profiles are very similar to those reported by Huang *et al.* [43], and other couples examined in this study also exhibited similar profiles regardless of cooling rate. The relative concentration of U and Mo clearly increases and decreases, respectively, within the U-10Mo alloy similar to the observation also reported by Huang *et al.* [43]. This is a favorable diffusional behavior for the barrier effectiveness of Zr to retain the U-density stability within the metallic fuel. However, it should be noted that the enrichment of U is accompanied by the depletion of Mo, presumably due to the formation of Mo₂Zr, and can alter the stability of γ U(Mo) phase, as observed in study as a β U layer.

Figure 25 shows the semi-quantitative diffusion paths estimated for the quenched and furnace-cooled diffusion couples annealed at 650 °C for 480 hours. Despite the scatter due to the presence of two phase regions, compositions determined from the XEDS and the phase constituents identified (except for the α Zr and U₆Zr₃Mo precipitates upon cooling), the diffusion path constructed follows the ternary isotherm approximately with two-phase equilibrium between the γ U(Mo) and Mo₂Zr, the β U and Mo₂Zr, the β Zr and Mo₂Zr, β Zr and α Zr. In all the diffusion couples, the two-phase region containing the γ U(Zr) and Mo₂Zr equilibrium was not observed. However, this may explain why α Zr precipitates were observed, upon cooling to a room temperature, in the vicinity of Mo₂Zr phases. Although the concentration profiles determined via XEDS follow the ternary isotherm closely in a semi-quantitative manner, detailed analyses for the

determination of diffusion coefficients and phase diagrams (i.e., solubility limits) could not be carried out due to the presence of non-planar interfaces, two-phase regions and precipitation of αZr . The βZr layer also did not exhibit any discernable concentration gradient.

5.3.3. Time- and temperature-dependence of interdiffusion and reaction

Thickness of the interaction zone was measured from the terminal ends of the U10Mo alloy and pure Zr, defined by $\partial C/\partial x = 0$, from the couples that were quenched after each anneal as reported in Table 5 and Figure 26. Assuming the initial thickness of zero, the growth of the interaction zone does not follow the parabolic growth as seen in Figure 26. In fact it does not follow any other time-dependence, $t^{(1/n)}$ where $n \geq 1$. However, when the growth constant was determined just for the couples annealed at 650 °C as a function of time in this study (i.e., assuming a certain incubation period, approximately 159 hours), a growth rate of $7.75 (\pm 5.84) \times 10^{-16} \text{ m}^2/\text{s}$ was determined as reported in Table 5. Furthermore, this analysis demanding the incorporation of “incubation” period, may be related to the Huang’s [43] observation of “negligible” interaction in the same diffusion couple annealed at 600 °C for 960 hours. Whether this incubation period is due to nucleation barrier for relevant phases (e.g., βU and Mo_2Zr) or dissolution of native oxide, a further study is warranted for a better understanding of experimental variables and thermo-kinetic description for nucleation and growth.

The growth constant determined at 650 °C with an assumption of certain incubation period was plotted along with those determined at higher temperature by Huang *et al.* [43]. The

temperature dependence of the growth constant for the interaction between U10Mo alloy and Zr at 650 °C obeys the Arrhenius behavior of the activation energy close to what was previously determined by Huang *et al.* [43] at ~219 kJ/mol as reported in Table 6 and presented in Figure 27.

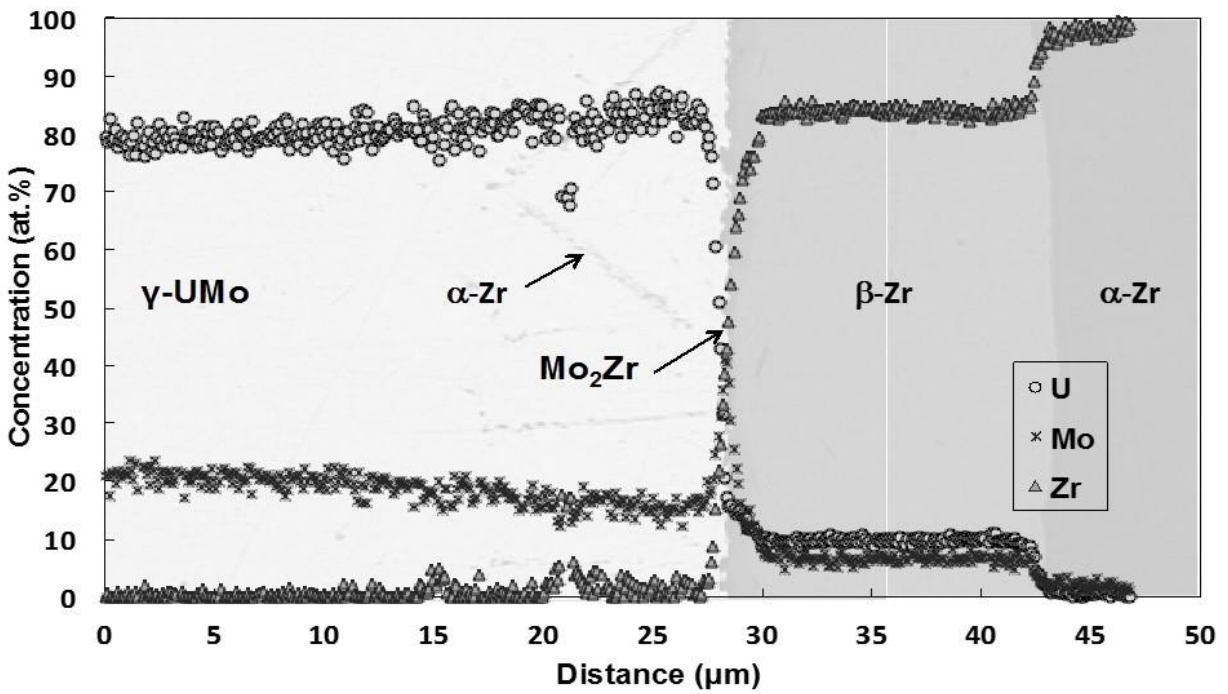


Figure 24. Concentration profiles from U10Mo vs Zr diffusion couples annealed at 650 °C for 720 hours after water-quench.

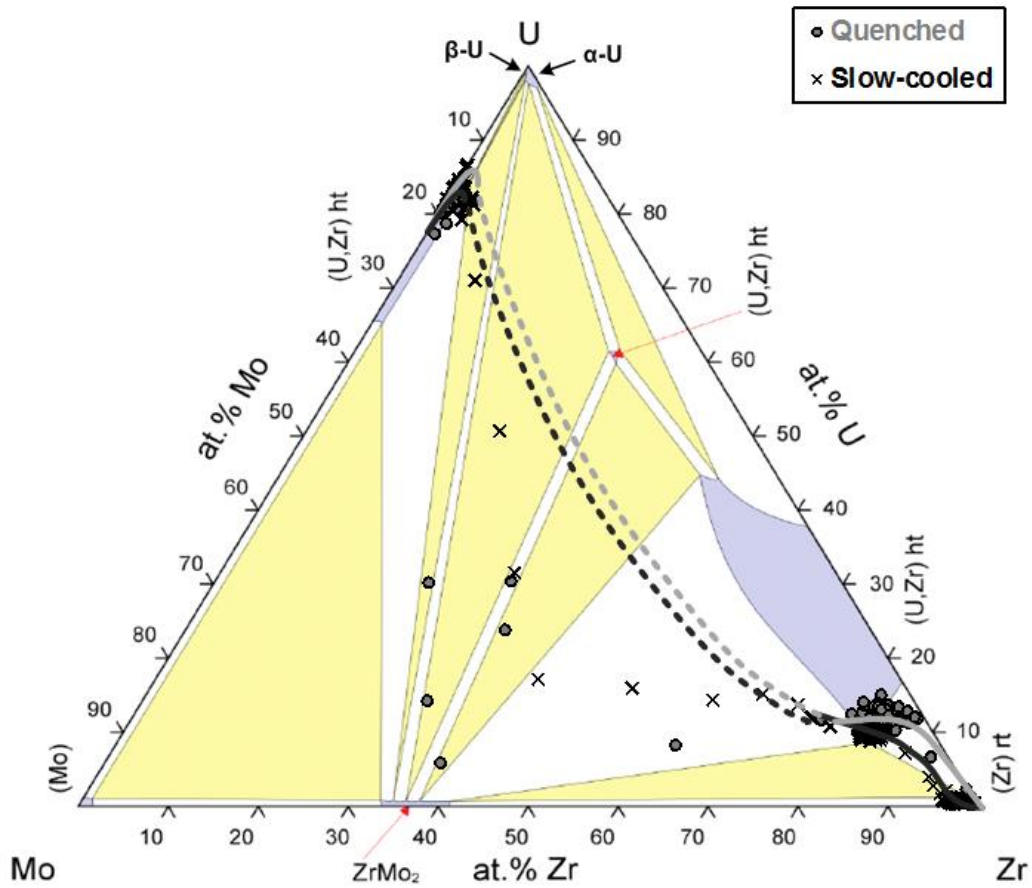


Figure 25. Estimated diffusion paths from U10Mo vs. Zr diffusion couples annealed at 650 °C for 480 hours after water-quench and furnace-cooling.

Table 5. Growth rate of diffusional interaction zone determined from U10Mo vs. Zr diffusion couple annealed at 650 °C followed by water-quench.

Temperature (°C)	Annealing time (hour)	Measured Thickness (μm)	Growth rate (m ² /s)
650	240	17.2 ± 0.8	7.75 × 10 ⁻¹⁶
	480	53.1 ± 1.0	
	720	83.3 ± 1.3	

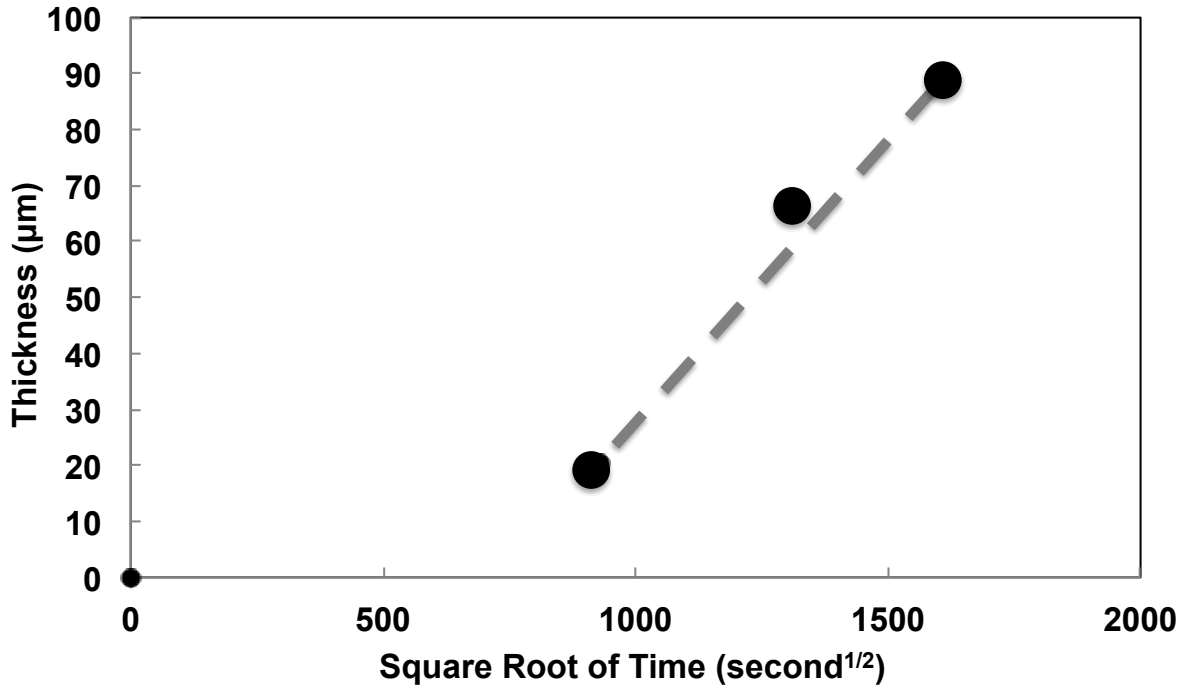


Figure 26. Thickness of the diffusional interaction zone as a function of time for the U10Mo vs Zr diffusion couples annealed at 650 °C followed by water-quench.

Table 6. Growth rate of interaction zone of U10Mo vs. Zr diffusion couples reported by Huang *et al.* [43] and this study.

Temperature (°C)	Thickness (μm)	Annealing time (hour)	Growth rate (m ² /s)	Activation Energy (kJ/mol)
1000	1130	96	1.85×10^{-12}	219.4
900	990	240	5.76×10^{-13}	
800	650	480	1.22×10^{-13}	
650	See Table 5		$7.75 (\pm 5.84) \times 10^{-16}$	

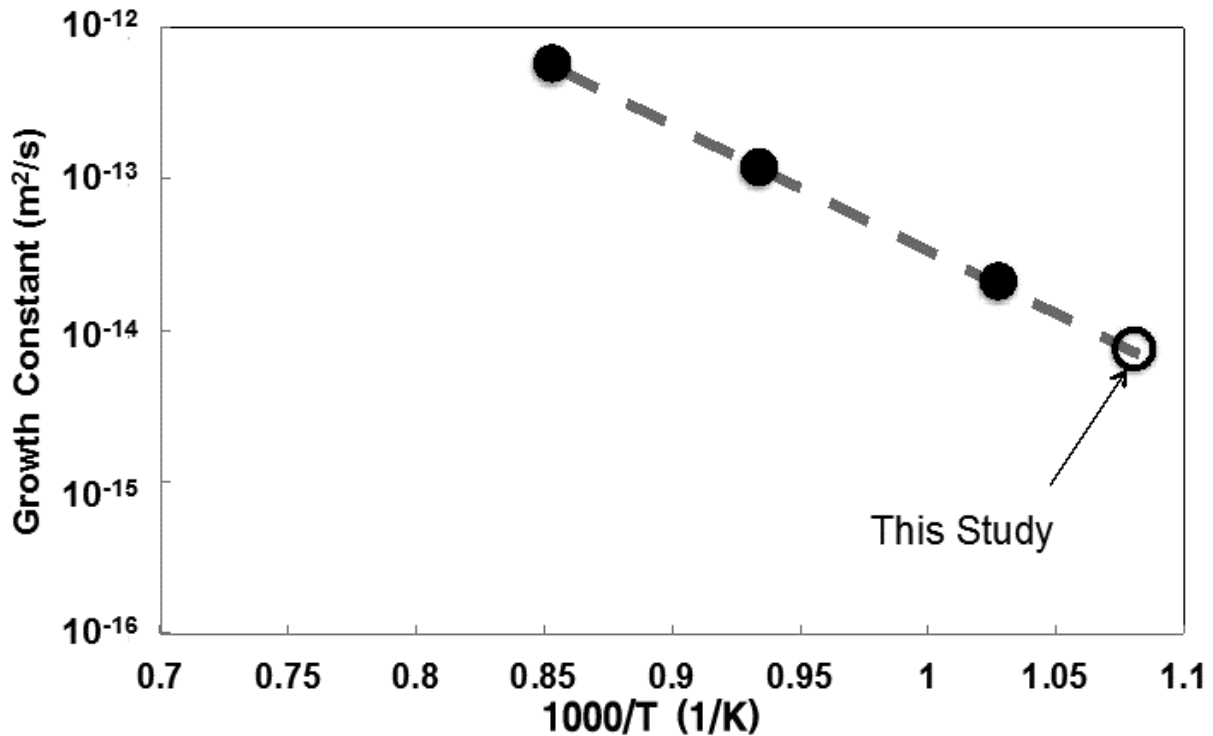


Figure 27. Temperature dependence of growth constant from U10Mo vs. Zr diffusion couples annealed at 1000, 900, 800 [43] and 650 °C.

5.4. Discussion

In this investigation, U10Mo vs. Zr diffusion couples were annealed at 650 °C for 240, 480 and 720 hours to examine the development of phase constituents and microstructure, and to quantify the growth kinetics of the interdiffusion–reaction zone. In all diffusion couples, including the one furnace-cooled after 480 hours of anneal, a thick layer of β Zr and a thin layer of β U were observed to develop. A discontinuous layer of Mo_2Zr was found between the β Zr and β U layers, and within the β U layer, small α Zr precipitates were found. Acicular α Zr and blocky $\text{U}_6\text{Zr}_3\text{Mo}$

phases were also observed within the γ U(Mo). The phase constituents and microstructural development are schematically summarized in Figure 23. While the complex diffusion microstructure was analyzed by TEM with small samples without any image analysis, the phase constituents followed the local phase equilibrium consistently with the ternary isothermal phase diagram at 650 °C, excluding the presence of α Zr and U_6Zr_3Mo . These two phases appear to form during cooling, both water-quench and furnace-quench. There was no significant deviation in diffusion paths for the couples quenched in water and furnace-cooled after anneal for 480 hours. This similarity of phase constituents and concentration profiles between water-quenched and furnace-cooled samples indicates that the cooling-rate is not a significant factor that needs to be controlled during the co-rolling and HIP'ing of a monolithic fuel plate.

Phase constituents and microstructural development reported in this study are different from those previously reported by Perez *et al.* [39] and Jue *et al.* [46]. Notably the UZr_2 phase layer was not observed in this study. However, these previous studies have reported the phase constituents and microstructural development following the monolithic fuel plate processing: repeated soaking at 650 °C and co-rolling followed by HIP, typically carried out at temperature (520 - 580 °C) lower than 650 °C. The ternary phase equilibrium for the U-Mo-Zr system changes drastically between this temperature range [8], and can produce changes in observed phase constituents and microstructure. This changes in observation as a function of temperature, either independently or sequentially, warrant fundamental investigations of interdiffusion and reaction in the U-Mo-Zr system between 650 and 500 °C, relevant to overall monolithic fuel plate processing.

The phase constituents, microstructure and concentration profile found in this study as a

function of time, in general, agree well with the results reported by Huang *et al.* [43] for diffusion couples at high temperature. In particular, the diffusion couple annealed at 700 °C by Huang *et al.* [43], with terminal Zr as the α Zr, is very similar to the results obtained in this study. First, Zr is an excellent candidate for diffusion barrier between U-Mo fuel and Al cladding alloy with an additional benefit of U uphill diffusion, which is reported by both Huang *et al.* [43] and this study. Second, the phase constituents and microstructure reported are also similar, although this study examined more details with TEM and SAED analyses for the Mo_2Zr , βU , $\text{U}_6\text{Mo}_3\text{Zr}$ and αZr phases distributed within the interaction zone.

Although the growth of the interaction zone required an assumption of a certain incubation period, the growth constant with diffusion couples annealed at 650 °C for 240, 480, and 720 hours was calculated to be $k = 7.75 (\pm 5.84) \times 10^{-16} \text{ m}^2/\text{s}$. This, combined with those reported by Huang *et al.* [43], exhibited an excellent Arrhenius temperature-dependence with activation energy of 219 kJ/mol. However it should be noted that the diffusion work performed by Huang *et al.* [43] at 600 °C for 960 hours showed negligible interdiffusion and reaction, and the current work supports that the interdiffusion and reaction between U10Mo and Zr is influenced by other factors, including the possible presence of an incubation period. To understand the nature of the incubation period, if any, a future investigation would require understanding of nucleation/growth of intermetallic layers and/or dissolution of native oxide scale (i.e., experimental procedure).

A future investigation with respect to the irradiation behavior should focus on the presence of αZr and βU phases, based on this study. Preliminary research [16] on the irradiation behavior of U10Mo with a Zr diffusion barrier has indicated, by optical microscopy, possible void formation

where these phases are located, i.e., a few micrometers away from the Mo_2Zr layer, toward the $\gamma\text{U}(\text{Mo})$. This is the location where the βU exists and the acicular αZr phase extends into the $\gamma\text{U}(\text{Mo})$. Depletion of Mo from the $\gamma\text{U}(\text{Mo})$ solid solution by the formation of the Mo_2Zr phase can destabilize the $\gamma\text{U}(\text{Mo})$ into the βU phase. While the γU has complete solubility with Zr, the βU phase has a very low solubility (and that for the αU phase is even lower).

CHAPTER 6: U vs. Zr DIFFUSION COUPLES

6.1. Background

U and Zr are being considered as main elements for metallic fuel and diffusion barrier, respectively. U-based metallic fuels have high burnup ability, high thermal conductivity, compatibility for fabrication and advantage of recycling [1-3]. Properties of Zr are low neutron absorption, high melting point, good corrosion resistance and good compatibility for fabrication process. U-Zr alloy, BCC γ phase above 688 °C at 20 at.% Zr, has been investigated with additional elements such as Mo and Pu [90].

U alloying with Mo retains the BCC γ phase, and is an excellent metallic fuel for test and research reactors with Zr diffusion barrier reported as one of potential candidates for diffusion barrier [38, 40-43]. Thus, the U-Mo alloy and Zr diffusion barrier have been utilized for the monolithic fuel plate containing the largest U density [39, 44, 45, 47, 51].

The U-Zr alloys also has been investigated for the metallic fuel for fast reactors with additional elements such as the actinides, Pu, Am, Np and etc, under the AFCI program [1, 91]. Transmutation of the actinides produced from spent fuel in the U-Zr fuel reduces quantities, radiotoxicity and long term heat-capacity. From irradiated U-Zr and U-Pu-Zr fuels in EBR-II, the redistribution by Zr migration has been investigated [92-96]. The atomic migration of Zr resulted in a composition gradient in the single-phase. In order to examine the redistribution of constituents, the thermal migration flux for each element was determined from the combination of atomic mobility and heat of transport with the gradients of composition and temperature.

Ogata *et al.* [97] measured the interdiffusion coefficients for the (γ U, β Zr) solid solution in

the temperature range of 700 to 950 °C with the Zr concentration range of 0.1 to 0.95. The interdiffusion coefficients in the Zr concentration range of 0.2 to 0.4 below 950 °C were lower than results of Adda *et al.* [98] because of the reduced thermodynamic factor in the Zr concentration range. Akabori *et al.* [99] presented the interdiffusion behavior in the UZr_2 and $(\gamma\text{U},\beta\text{Zr})$ phases in the temperature ranges of 550 to 580 °C and 650 to 700 °C, respectively.

6.2. Experimental Parameters

The temperature for each heat treatment, 580, 650, 680 and 710 °C, has been indicated in U-Zr phase diagram of Figure 28. The U-Zr diffusion couples were annealed for 360, 480, 720 and 960 hours at 580 °C for time-dependent analysis.

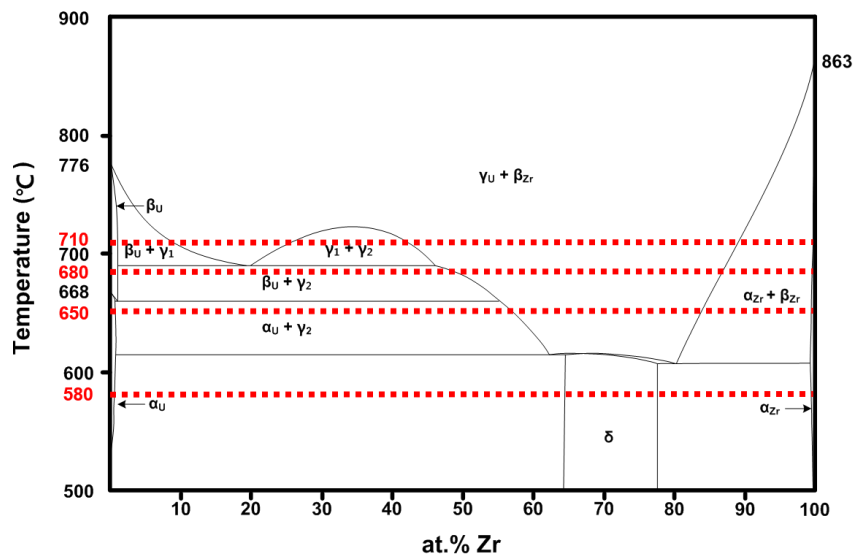


Figure 28. U-Zr equilibrium phase diagram with annealed temperatures for U-Zr isothermal diffusion couples.

6.3. Results

6.3.1. Phase constituents and microstructure

Typical BSE micrographs from the U vs. Zr diffusion couples are presented in Figure 29 and Figure 30. Figure 29(a), (b), (c) and (d) are the BSE micrographs from water-quenched diffusion couples that were annealed at 580 °C for 960 hours, at 650 °C for 480 hours, at 680 °C for 240 hours and at 710 °C for 96 hours, respectively. For the time-dependent analysis, U-Zr diffusion couples were annealed at 580 °C for 360, 480, 720 and 960 hours as shown in Figure 30. The interdiffusion and reaction in these couples produced similar microstructure and constituent phases. Based on BSE micrographs and XEDS analyses, phase constituents such as δ (UZr_2) solid solution (hP3), αZr (hP2) precipitates and $\alpha'\text{U}$ were identified as labeled in Figure 29 and Figure 30. The acicular Zr precipitates were assumed to be formed from supersaturated Zr solute in βU and αU at higher temperature during water-cooling process because αU at room temperature has no solubility of Zr. High purity βU and γU have to be stabilized as orthorhombic αU at room temperature despite water-cooling. Despite considerable research on the U-Zr system and its alloys, the α' phase has not been documented in detail. In order to ensure the accurate data for α' U, additional investigation of U-Zr solid-to-solid system is essential.

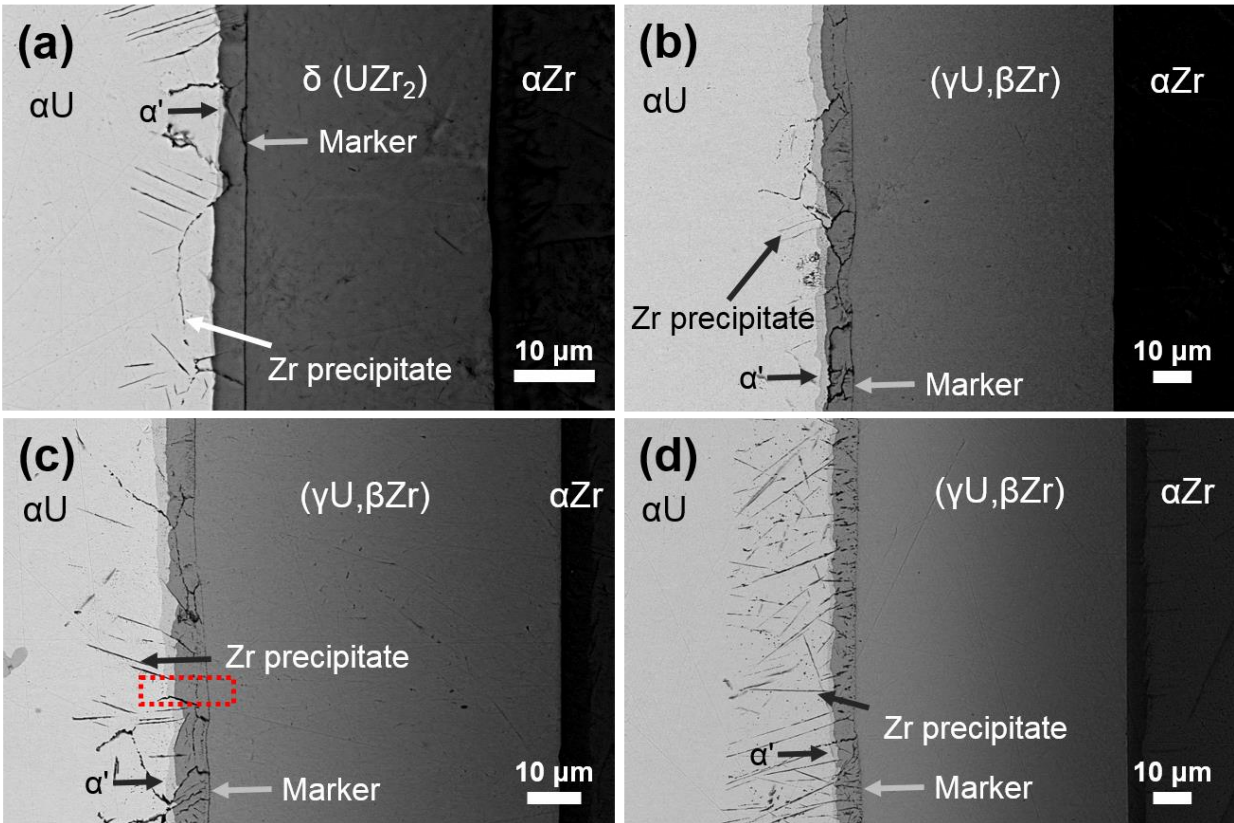


Figure 29. BSE micrographs from the water-quenched U vs. Zr diffusion couples annealed (a) at 580 °C for 960 hours, (b) at 650 °C for 480 hours, (c) at 680 °C for 240 hours, and (d) at 710 °C for 96 hours. The selected areas (red-dot rectangular) in (a) and (c) are indicated for TEM analyses.

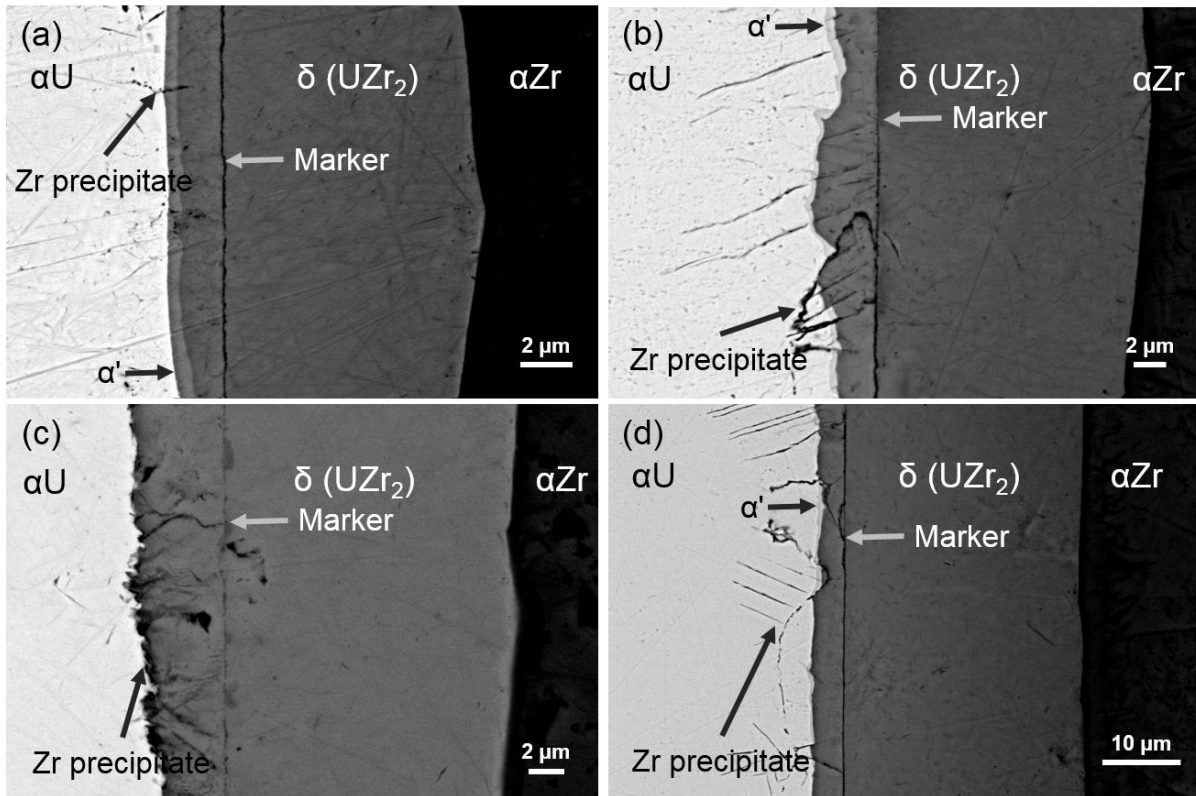


Figure 30. BSE micrographs from the water-quenched U vs. Zr diffusion couples annealed at 580 °C for (a) 360, (b) 480, (c) 720 and (d) 960 hours.

Figure 31 presents a HAADF STEM micrograph selected from the red-dotted rectangle in Figure 29(c) for the couple annealed at 650 °C for 480 hours. In α U phase, α Zr precipitates of relatively larger volume were formed, while in the other side, UZr_2 precipitates of relatively less volume were distributed in $(\gamma U, \beta Zr)$ phase. In particular, both α Zr and UZr_2 precipitates were found within α' phase layer. The SAED patterns were employed to identify the layers of α U (Orthorhombic) and $(\gamma U, \beta Zr)$ (BCC). The α U was formed by allotropic transformation of β U into α U during cooling in water. HR-TEM micrograph with FFT analysis was used to identify the nano-scale Zr precipitates as presented in Figure 33.

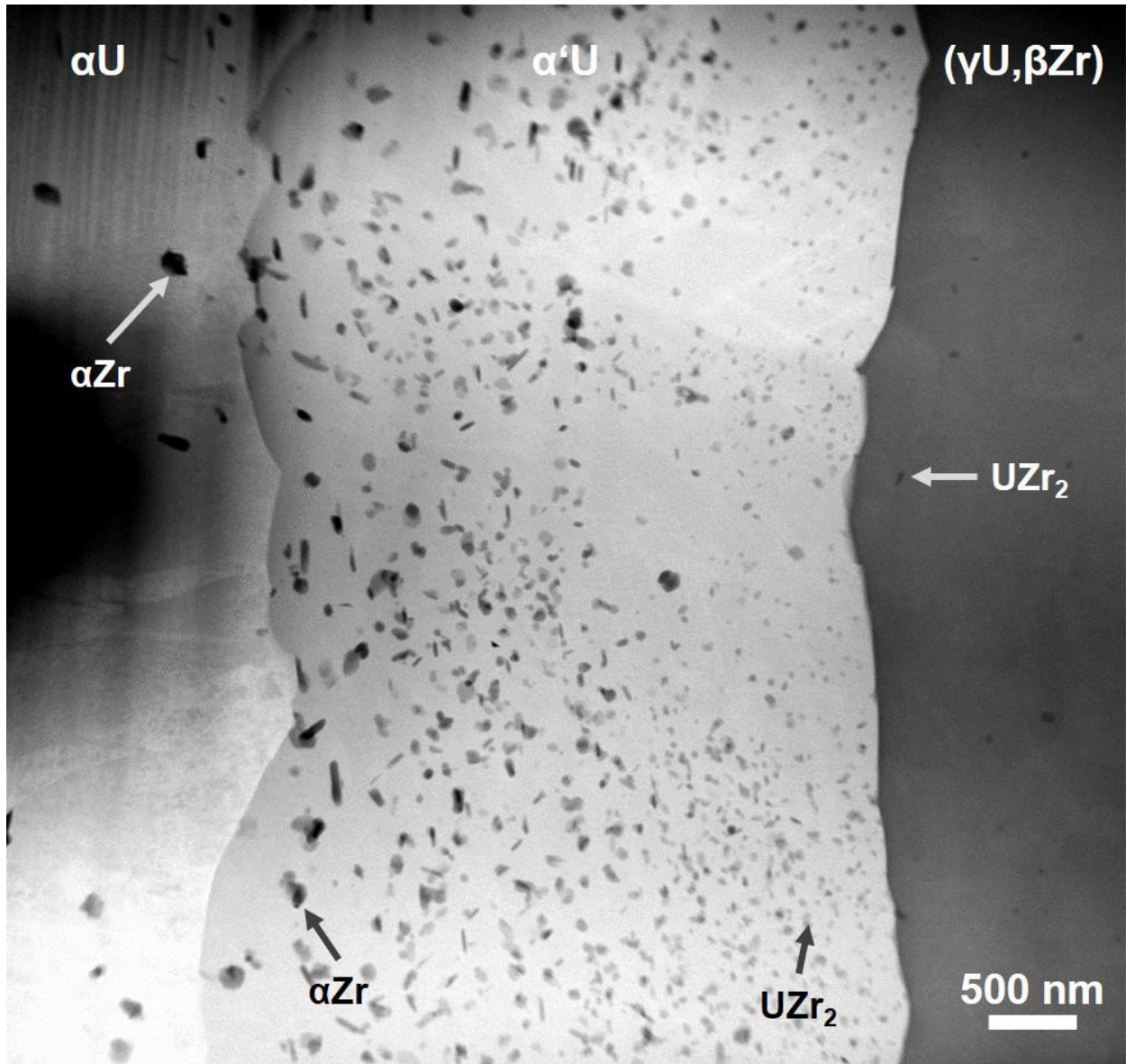


Figure 31. High angle annular dark field micrographs of the water-quenched U vs. Zr diffusion couple annealed at 650 °C for 480 hours selected from Figure 29(c).

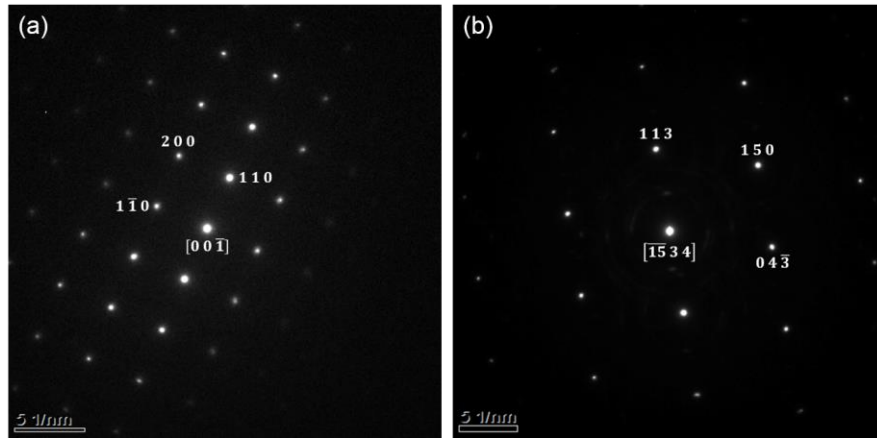


Figure 32. Selected area diffraction patterns of (a) $(\gamma\text{U},\beta\text{Zr})$ solid solution and (b) αU .

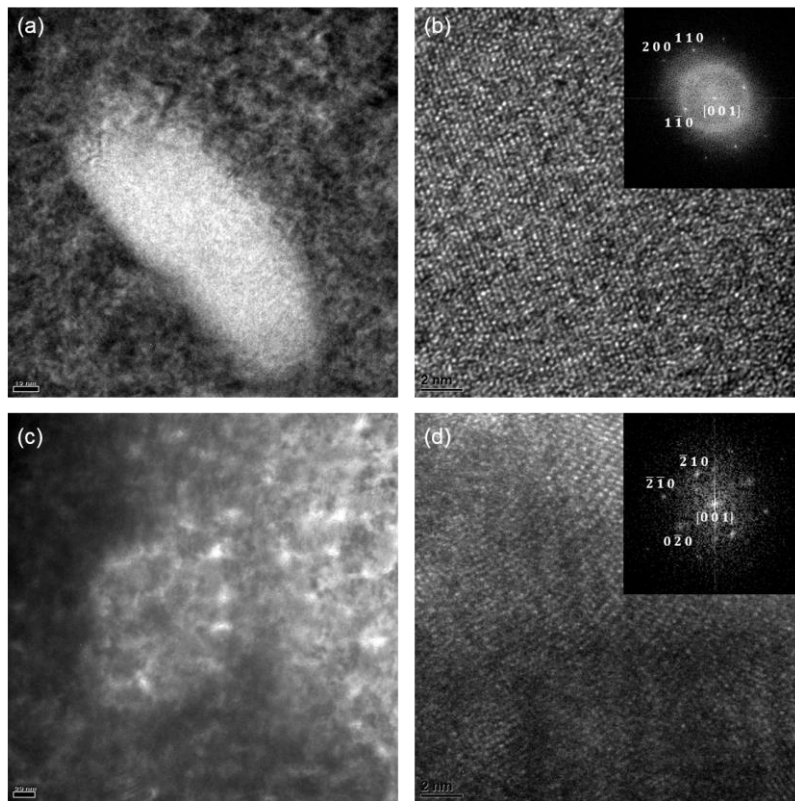


Figure 33. The precipitate flakes for (a) BF and (b) HR-TEM with FFT analysis of αZr (hP2), and (c) BF and (d) HR-TEM with FFT analysis of UZr_2 (hP3).

The crystallographic information of α' has never been reported. So, the α' has been examined by TEM analyses as shown in Figure 34. BF micrograph shows UZr_2 , αU and α' phases with the needle-like Zr precipitate. The red circle indicates the selected area for HR-TEM and SAED pattern for α' . The α' phase, not reported, in the U-Zr phase diagram is estimated as a reduced-volume orthorhombic structure of lattice parameter $a \times b \times c = 2.65 \times 5.40 \times 4.75$ (Å). The α' phase was characterized without compositional gradient from TEM XEDS analysis. Table 7 summarizes the crystallographic information. In the result of Akabori *et al.* [99], a U-rich precipitates of less than 1 μm in size were observed in the U68Zr vs. U75Zr diffusion couple annealed at 520 °C for 2400 hours near the initial interface. Although suspected as the α' phase, the identification was not conducted because of the limited resolution in SEM.

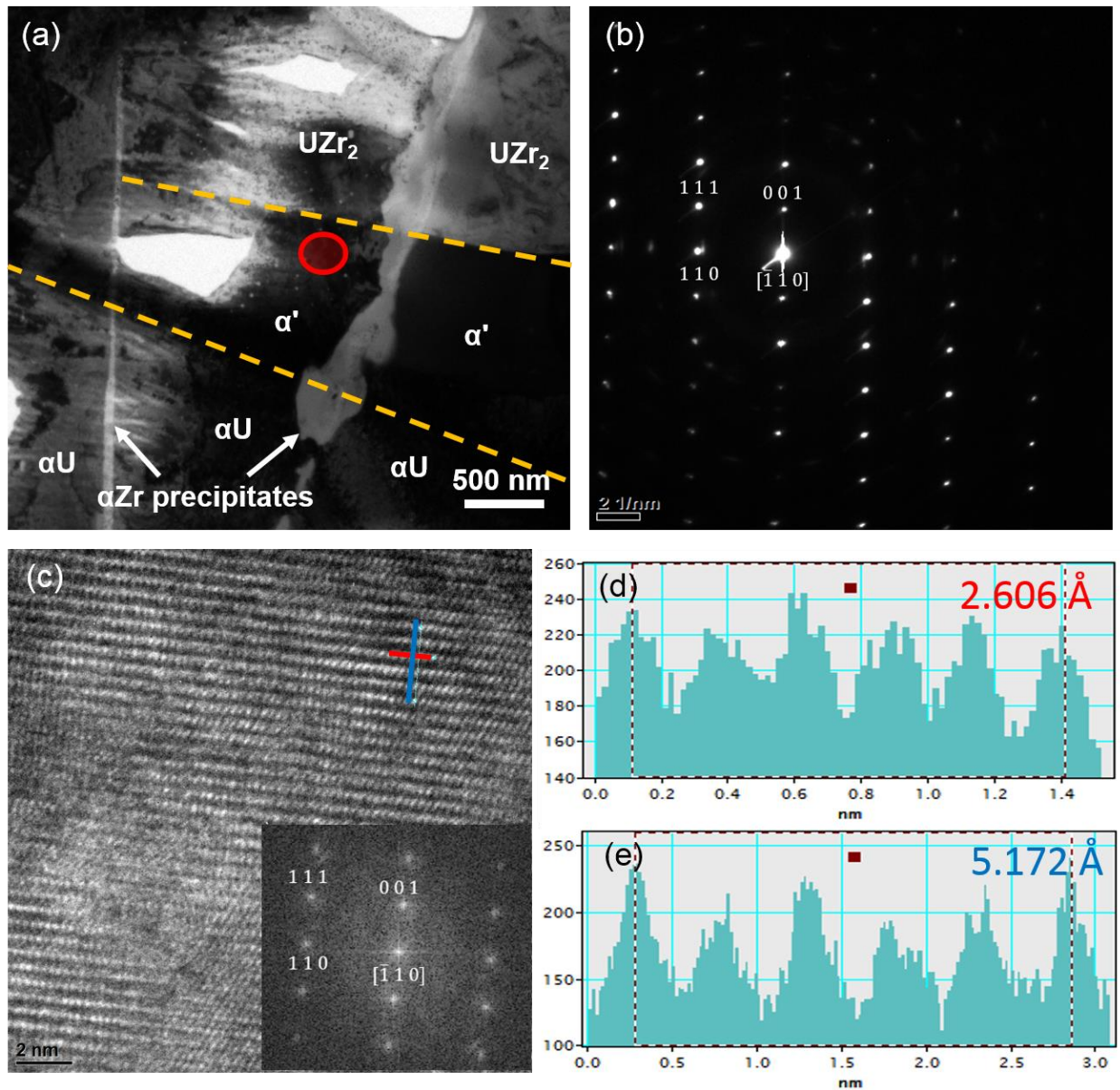


Figure 34. (a) BF micrograph of the water-quenched U vs. Zr diffusion couple annealed at 580 °C for 960 hours selected from Figure 29(a). (b) SAED pattern and (c) HR-TEM micrograph with FFT analysis selected from the red circle area in (a). Intensities of the pixel at the positions for lattice parameter (d) a and (e) b measured from the red and blue lines, respectively.

Table 7. Crystallographic data for each phase.

Phase	P.S.	a (Å)	b (Å)	c (Å)	Volume (Å ³)	Density (g/cm ³)	Molar volume (m ³ /mol)
αU	oC4	2.854	5.869	4.955	83.0	19.046	1.25 × 10 ⁻⁵
βU	tP30	10.759	10.759	5.656	654.7	18.110	1.31 × 10 ⁻⁵
γU	cI2	3.474	3.474	3.474	41.9	18.860	1.26 × 10 ⁻⁵
δ (UZr ₂)	hP3	5.030	5.030	3.080	67.5	10.346	1.35 × 10 ⁻⁵
(γU,βZr)	cI2	~ 3.524	~ 3.524	~ 3.524	~ 43.8	~ 9.939	~ 1.32 × 10 ⁻⁵
αZr	hP2	3.232	3.232	5.147	46.6	6.505	1.40 × 10 ⁻⁵
βZr	cI2	3.545	3.545	3.545	44.6	6.798	1.34 × 10 ⁻⁵

6.3.2. Diffusion kinetics

Thickness of the interdiffusion and reaction zone was measured from the terminal ends of the U and Zr, defined by $\partial C/\partial x = 0$. The concentration profile and the corresponding interdiffusion flux profile for each U-Zr diffusion couples as a function of thickness are presented in Figure 35. The marker plane, x_m , shifted to the U-rich side from the original interface, x_0 , for all U-Zr diffusion couples in the laboratory frame. Therefore, U diffusion into the Zr-rich side is faster than Zr diffusion into the U-rich side. The flux and the interdiffusion coefficient could be estimated using x_0 . The interdiffusion coefficients can be calculated from Equation (11), The Boltzmann-Matano method, for αU with Zr precipitate, and (γU,βZr) solid solution (or δ-UZr₂ below 615 °C) using

semi-quantitative method of SEM XEDS. Figure 36 displays the interdiffusion coefficients as a function of Zr-concentration for each temperature. According to Gibbs phase rule, no two phase region can exist in an isothermal, isobaric binary system. However, a region of α U and Zr precipitates was observed, likely due to the higher solubility at high temperatures. When the diffusion couple was quenched to room temperature, the Zr solute atoms precipitated out as a result of the low solubility. It is thus assumed that the average composition at a plane containing α U and Zr precipitates represents the composition of the solid solution at high temperature. Semi-quantitative analysis was carried out using these averages to create representative composition profiles. Additionally, the variation of interdiffusion coefficient for each phase as a function of the total molar volume can be ignored because the total molar volume for each phase does not vary significantly as reported in Table 7.

Sauer-Freise with Wagner analysis was employed to calculate the integrated interdiffusion coefficients for the reaction layers using Equation (15) because the α' phase has a negligible concentration gradient. The integrated interdiffusion coefficients of U-Zr system as a function of temperature are presented in Figure 37. The vertical grey dot line separates (γ U, β Zr) and δ phases at about 615 °C. The steep slope for the integrated interdiffusion coefficients of the α U with Zr precipitate phase is largest, the other side, the lowest activation energy of α' phase was estimated because of the lowest slope. The activation energies and pre-exponential factors were estimated using the samples annealed above 650 °C because the change of largest thicknesses, (γ U, β Zr) and δ , at 615 °C can affect the kinetics properties. The integrated interdiffusion coefficient, pre-exponential factor and activation energy for each phase were reported in Table 8.

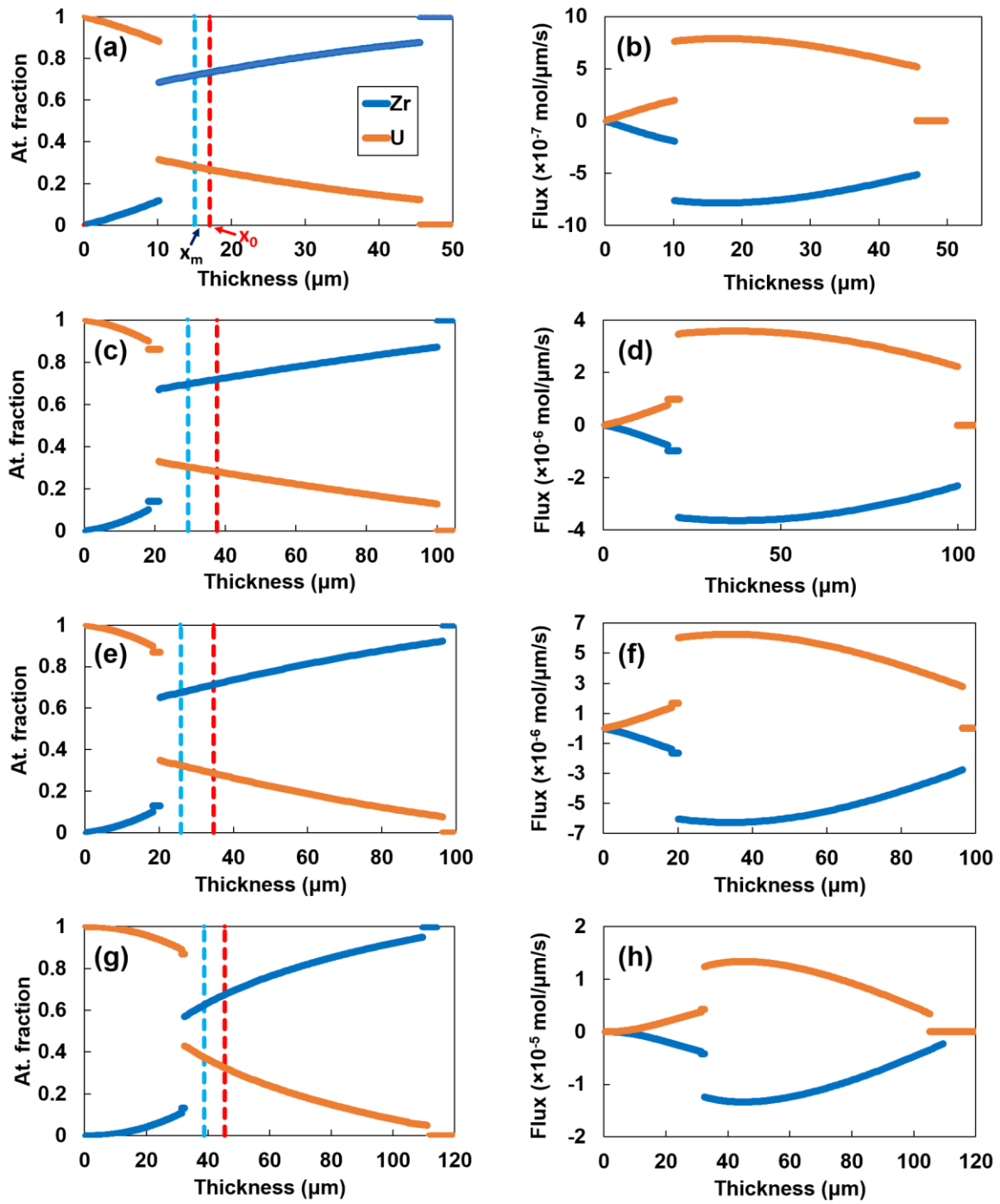


Figure 35. (a, c, e, g) Concentration profiles and (b, d, f, h) flux profiles for U-Zr diffusion couples annealed (a, b) at 580 °C for 960 hours, (c, d) at 650 °C for 480 hours, (e, f) at 680 °C for 240 hours and (g, h) at 710 °C for 96 hours.

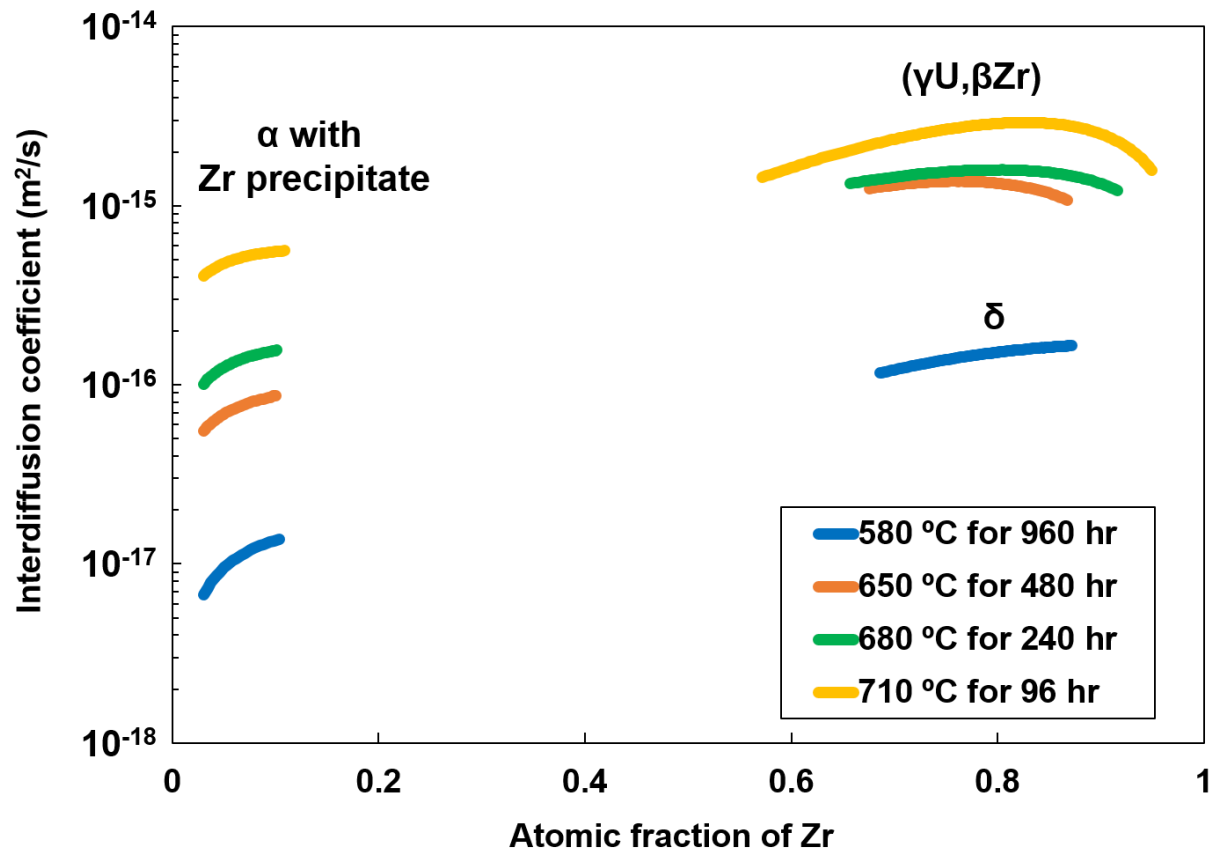


Figure 36. Interdiffusion coefficients determined using the Boltzmann-Matano method as a function of composition (at.% Zr).

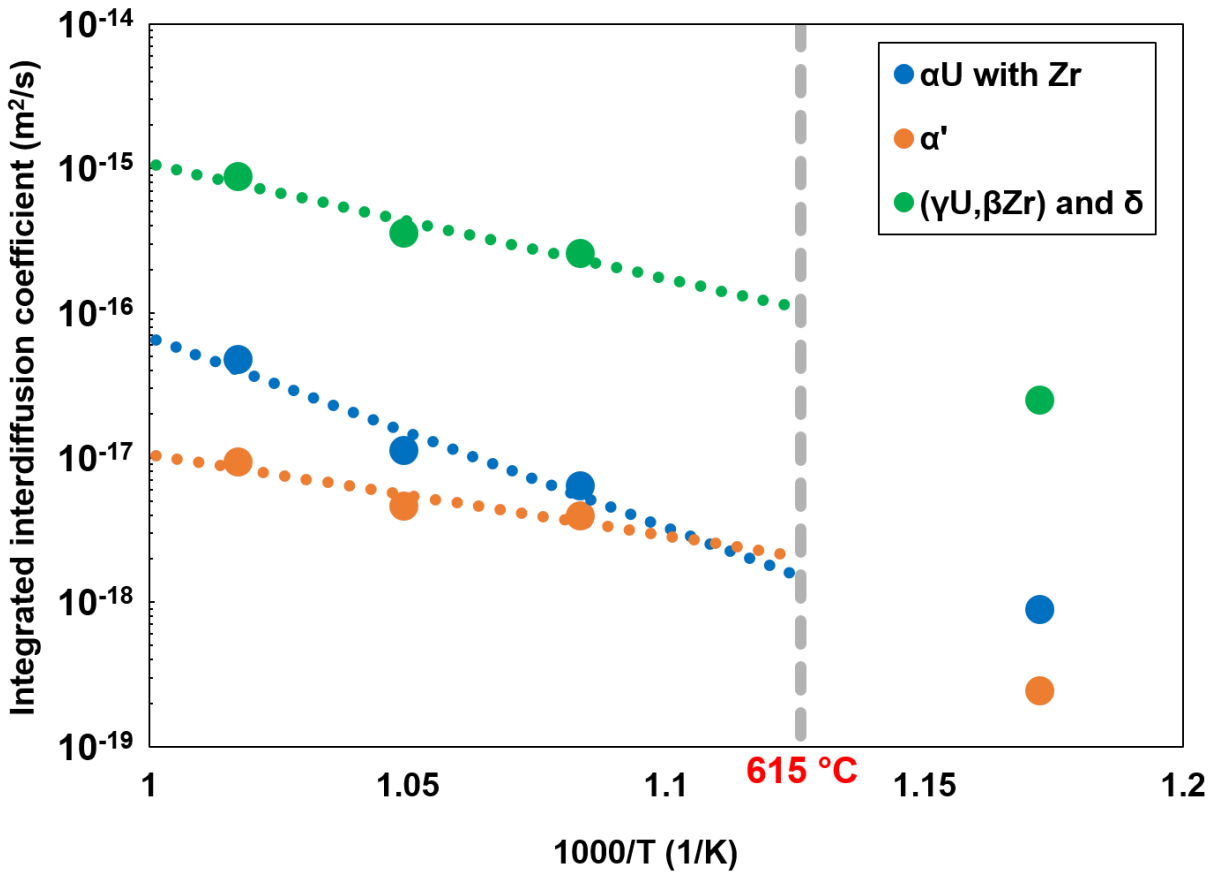


Figure 37. Integrated interdiffusion coefficients determined according to Sauer-Freise with Wagner analysis as a function of temperature.

Table 8. Integrated interdiffusion coefficient (\tilde{D}^{int}), pre-exponential factor (\tilde{D}_0^{int}) and the corresponding activation energy (\tilde{Q}^{int}) for Zr in each phase.

Anneal Parameter		αU with Zr precipitate	α'	$(\gamma\text{U},\beta\text{Zr})$ and δ
580 °C 960 h	\tilde{D}^{int} (m ² /s)	8.84×10^{-19}	2.43×10^{-19}	2.49×10^{-17}
650 °C 480 h	\tilde{D}^{int} (m ² /s)	6.29×10^{-18}	3.92×10^{-18}	2.57×10^{-16}
680 °C 240 h	\tilde{D}^{int} (m ² /s)	1.11×10^{-17}	4.56×10^{-18}	3.56×10^{-16}
710 °C 96 h	\tilde{D}^{int} (m ² /s)	4.71×10^{-17}	9.29×10^{-18}	8.69×10^{-16}
\tilde{D}_0^{int} (m ² /s)		3.54×10^{-5}	1.11×10^{-3}	4.84×10^{-12}
\tilde{Q}^{int} (kJ/mol)		223.23	251.66	107.58

Figure 38 plots the interdiffusion coefficients determined for 71 at.% Zr as a function of temperature for Akabori *et al.* [99], Ogata *et al.* [97] and this study. Overall, the interdiffusion coefficients of this study are larger than previous results. However, the slope for this study is slightly less than those for Akabori and Ogata.

The marker planes (x_m) were found in the (γ U, β Zr) solid solution at 650, 680 and 710 °C and δ -UZr₂ at 580 °C. The diffusion flux of U was larger than that of Zr at the marker plane within the lattice fixed frame. It allows to determine intrinsic diffusion coefficients of elements at the marker plane using Heumann analysis described by Equation (16). The intrinsic diffusion coefficient for each element at the marker plane as a function of temperature was plotted in Figure 39. Table 9 summarizes the intrinsic diffusion coefficients of U and Zr for each temperature, and interdiffusion coefficients calculated by the Darken equation (\tilde{D}^D) using Equation (17) and the Boltzmann-Matano analysis (\tilde{D}^{BM}) using Equation (11). The determined \tilde{D}^D and \tilde{D}^{BM} are consistent.

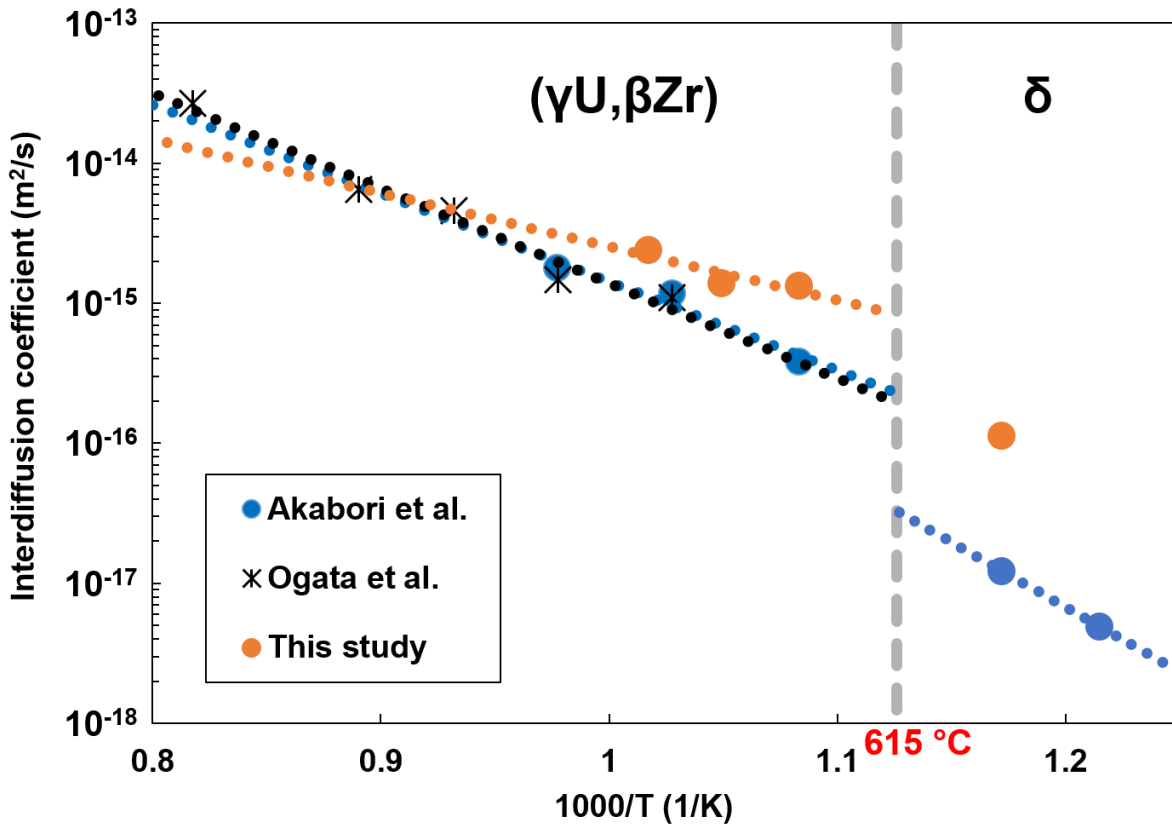


Figure 38. The interdiffusion coefficients at 71 at.% Zr as a function of temperature for Akabori *et al.* [99], Ogata *et al.* [97] and this study.

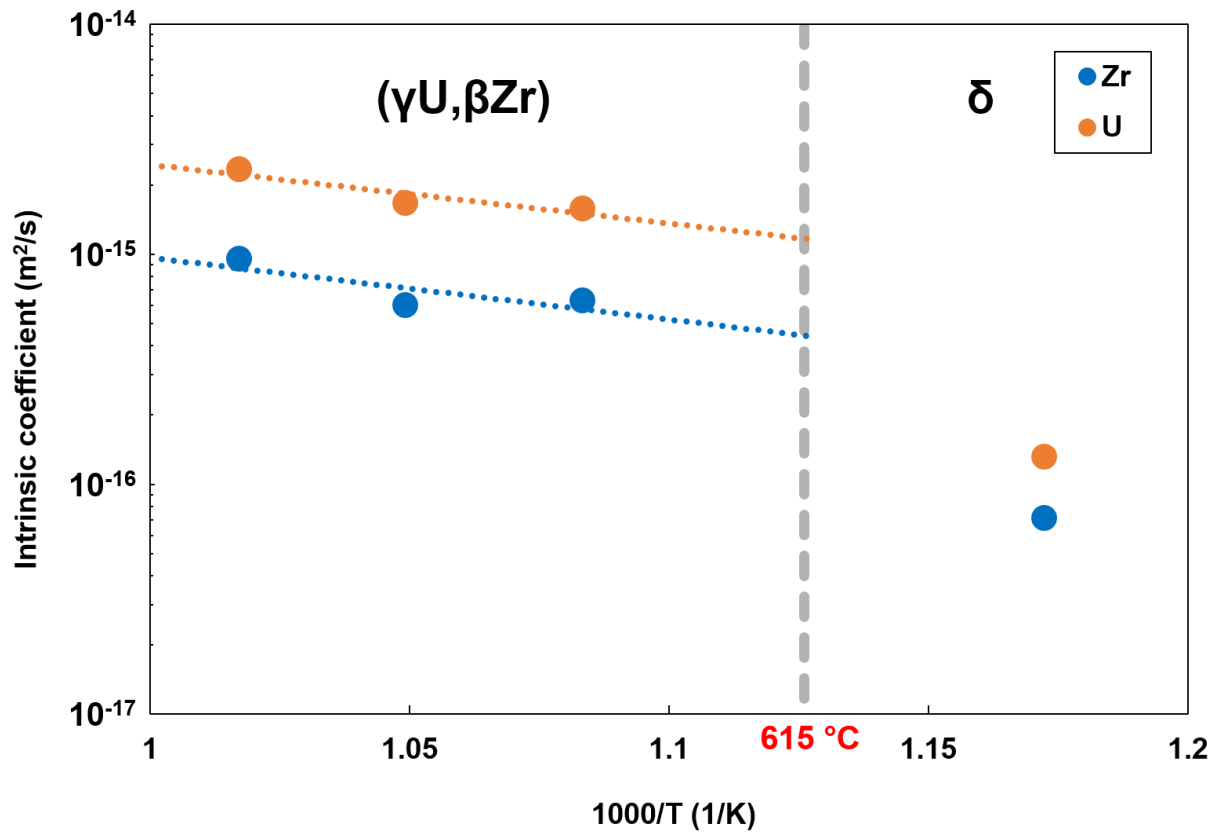


Figure 39. Intrinsic diffusion coefficient for (γU,βZr) as a function of temperature.

Table 9. Intrinsic diffusion coefficients (D_{Zr} and D_U), and interdiffusion coefficients determined by the Darken equation (\tilde{D}^D) and the Boltzmann-Matano method (\tilde{D}^{BM}). Pre-exponential factor and activation energy for each diffusion coefficient.

Temperature (°C)	Zr at.%	U at.%	D_{Zr} (m ² /s)	D_U (m ² /s)	\tilde{D}^D (m ² /s)	\tilde{D}^{BM} (m ² /s)
580	71.4	28.6	7.10×10^{-17}	1.31×10^{-16}	1.14×10^{-16}	1.15×10^{-16}
650	69.3	30.7	6.27×10^{-16}	1.57×10^{-15}	1.28×10^{-15}	1.28×10^{-15}
680	67.5	32.5	5.99×10^{-16}	1.66×10^{-15}	1.31×10^{-15}	1.30×10^{-15}
710	62.6	37.4	9.49×10^{-16}	2.33×10^{-15}	1.81×10^{-15}	1.81×10^{-15}
Pre-exponential factor (m ² /s)			5.10×10^{-13}	9.14×10^{-13}	3.45×10^{-13}	3.34×10^{-13}
Activation energy (kJ/mol)			51.38	48.81	42.90	42.65

The thicknesses with standard deviation were determined from measurement using image analysis of SEM BSE. Table 10 presents the measured thicknesses with standard deviations for the annealed time-dependent analysis at 580 °C. The growth of the interaction zone does not follow the parabolic growth as shown in Figure 40. It should be analyzed considering the incorporation of incubation time (156.3 hours) caused by a nucleation barrier for relevant phases or experimental variables such as oxidized surfaces. Table 11 summarizes the diffusion anneal parameters, layers developed, layer thicknesses, growth constants (k_p), pre-exponential factors and activation energies (Q_k). The parabolic growth constant and activation energy for each layer was calculated using Equation (3) and Equation (4), respectively. The growth constants were presented as a function of temperature, and obeyed the Arrhenius relationship as shown in Figure 41. The pre-exponential factors and activation energies of (γ U, β Zr) solid solution having the largest thickness and total interaction zone are very similar. The activation energy for α U with Zr precipitate was larger than that for (γ U, β Zr) solid solution.

Table 10. Total thickness for each U-Zr system annealed at 580 °C.

Temperature (°C)	Annealing time (hour)	Measured Thickness (μ m)
580	360	14.60 \pm 0.46
	480	27.90 \pm 1.37
	720	26.95 \pm 1.13
	960	46.49 \pm 3.13

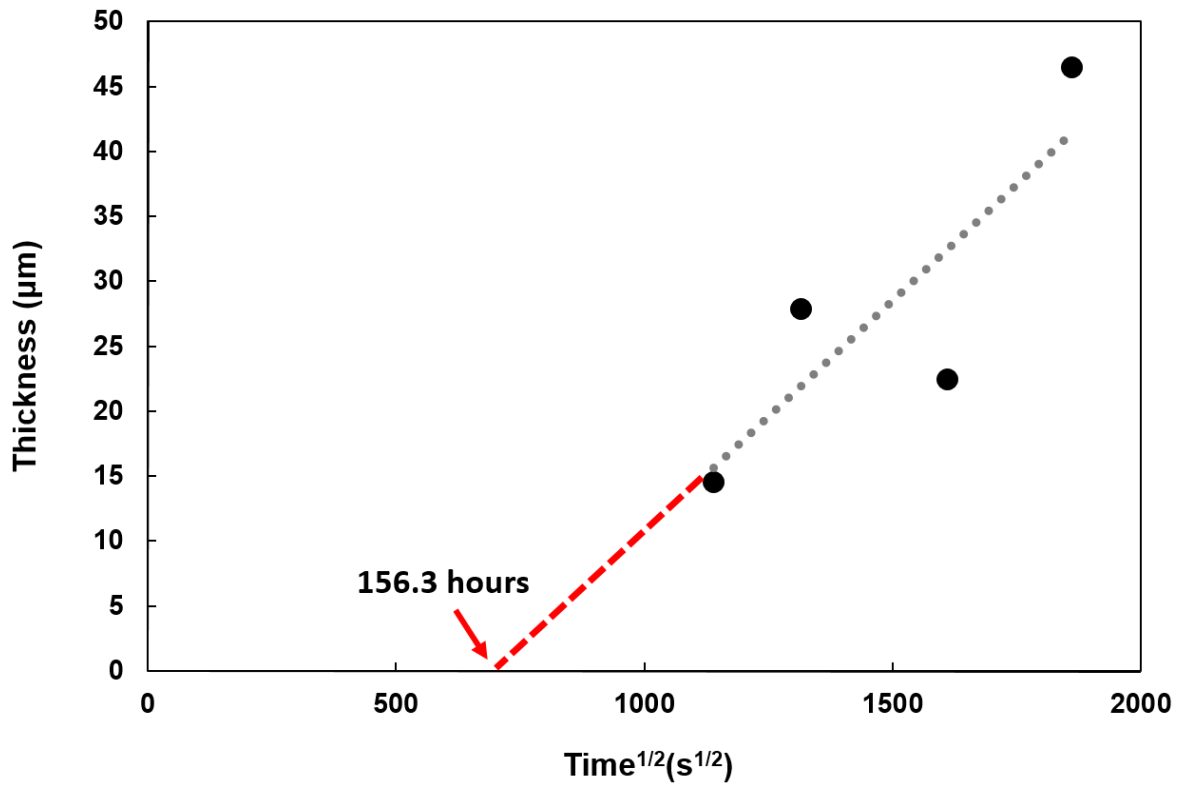


Figure 40. Thickness of the diffusional interaction zone as a function of time for the U vs. Zr diffusion couples annealed at 580 °C followed by water-quench.

Table 11. Layer thickness, parabolic growth constant and the corresponding activation energy for each layer in U-Zr system.

Anneal Parameter		α U with Zr precipitate	α'	$(\gamma$ U, β Zr) and δ	Total reaction zone
580 °C 960 h	Thickness (μ m)	11.99 ± 3.80	0.56 ± 0.34	34.93 ± 1.40	46.49 ± 3.13
	k_p (m^2/s)	1.75×10^{-17}	4.54×10^{-20}	1.77×10^{-16}	3.13×10^{-16}
650 °C 480 h	Thickness (μ m)	12.68 ± 5.01	2.94 ± 0.26	76.32 ± 0.39	91.96 ± 2.78
	k_p (m^2/s)	4.65×10^{-17}	2.50×10^{-18}	1.69×10^{-15}	2.45×10^{-15}
680 °C 240 h	Thickness (μ m)	16.92 ± 2.50	1.98 ± 0.39	72.31 ± 0.56	90.62 ± 3.36
	k_p (m^2/s)	1.66×10^{-16}	2.27×10^{-18}	3.02×10^{-15}	4.75×10^{-15}
710 °C 96 h	Thickness (μ m)	29.34 ± 1.26	1.38 ± 0.41	77.31 ± 1.14	106.25 ± 1.40
	k_p (m^2/s)	1.25×10^{-15}	2.76×10^{-18}	8.65×10^{-15}	1.63×10^{-14}
k_0 (m^2/s)		1.66×10^{-4}	4.58×10^{-6}	3.43×10^{-4}	3.45×10^{-4}
Activation Energy (kJ/mol)		209.35	229.97	199.45	194.30

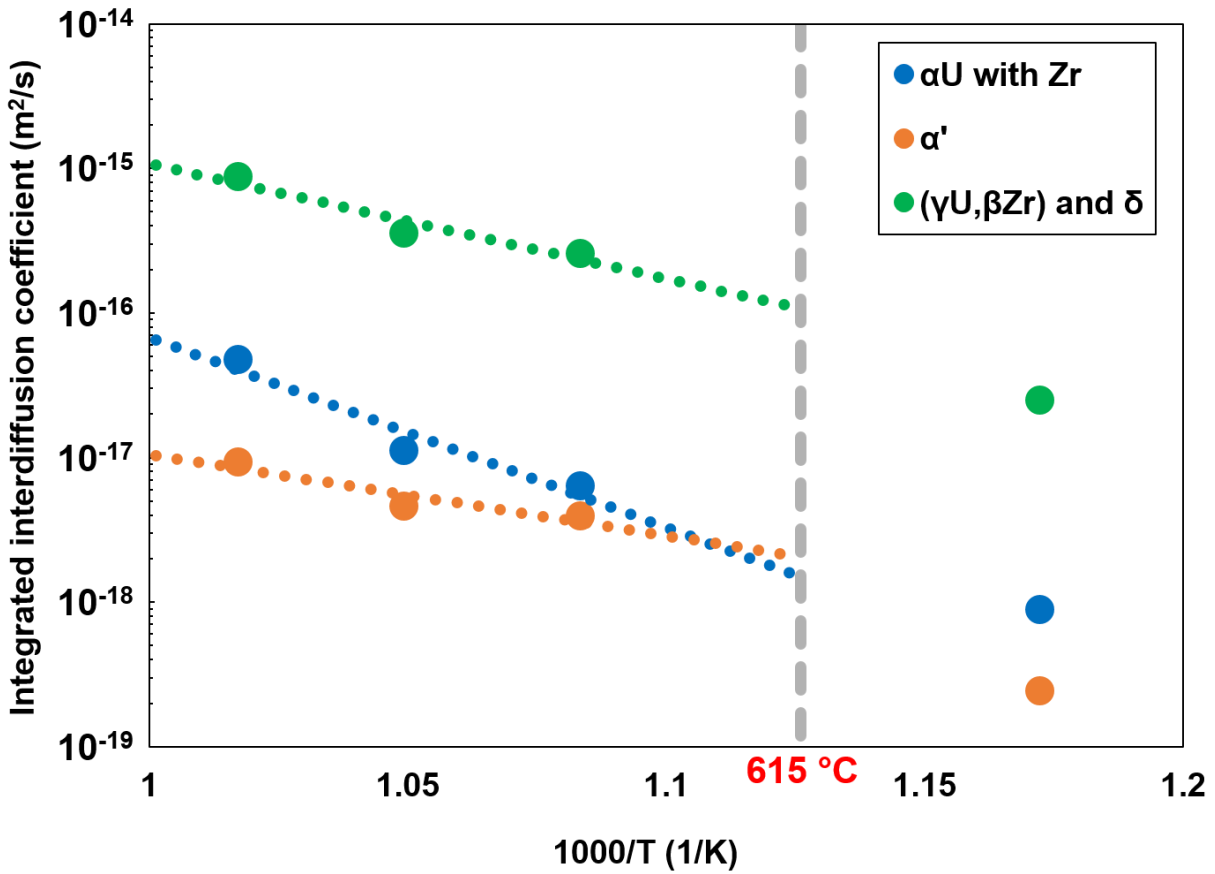


Figure 41. Temperature dependence of growth constants determined from the U vs Zr diffusion couples annealed at 580 °C for 960 hours, at 650 °C for 480 hours, at 680 °C for 240 hours and at 710 °C for 96 hours.

6.4. Discussion

Table 12 summarize incubation times, growth constants, pre-exponential factors and activation energies to compare the kinetic factors of U-Zr and U10Mo-Zr systems annealed at 650 °C. The incubation times of U-Zr and U10Mo-Zr systems were estimated to be similar. This suggests that the incubation time could be influenced by experimental environment for Zr during

preparation of the surface.

The growth constant of U-Zr was about 20 times as large as the growth constant of U10Mo-Zr even if there is no significant difference of the activation energy between the U-Zr and U10Mo-Zr system. This corresponds that the pre-exponential factor of U-Zr system is about 20 times larger than that of U10Mo-Zr system.

The α U phase was observed in all U-Zr diffusion couples because α U phase is thermodynamically transformed from β U or γ U [100]. While cooling U from 840 °C, it took about 0.2 second and 0.4 second for transformations of γ into β and β into α , respectively. Faster allotropic transformation of α U from β U or γ U as increasing purity of U has been reported by Peterson *et al.* [64]. The β U phase stabilized from depletion of Mo from U10Mo alloy could be retained because it included about 5 wt.% Mo.

Table 12. Incubation times, growth constants, pre-exponential factors and activation energies for the U-Zr and U10Mo-Zr diffusion couples annealed at 650 °C.

Kinetics factor	U-Zr	U10Mo-Zr
Incubation time (hours)	156	159
Growth constant (m ² /s)	1.63×10^{-14}	7.75×10^{-16}
Pre-exponential factor (m ² /s)	7.13×10^{-2}	3.53×10^{-4}
Activation energy (kJ/mol)	237.9	219.4

CHAPTER 7: HOT ISOSTATIC PRESSED U10Mo MONOLITHIC FUEL PLATE

7.1. Background

During fuel fabrication at elevated temperature and irradiation, interactions between the U-Mo fuel and the Al-alloy matrix/cladding transpire due to interdiffusion [29-32, 34-37, 101]. Microstructural changes and phase transformations due to these interactions may cause profound effects on overall performance of the fuel system including bond strength [102]. A diffusion barrier of Zr has been studied as a means to mitigate the metallurgical interactions [39, 43]. Understanding the diffusional interaction between U10Mo fuel alloy and Zr diffusion barrier, and consequent mechanical behavior has been a subject of many recent investigations [39, 43, 103].

Decomposition of γ U10Mo into α U and γ' U₂Mo occurred because the HIP process was carried out near the eutectoid temperature. Meyer *et al.* [104] reported the chemical banding by inhomogeneous Mo composition existed, and Jue *et al.* [46] presented decomposed areas of α and γ' from γ due to heat treatment near the eutectoid temperature. The low- (~ 5 wt.%) and high-Mo (~ 13 wt.%) phases were assumed as α and γ' , respectively, and formed from decomposition of γ . In this study, the analyses for phase transformation of U10Mo alloy as functions of HIP parameters, temperature, holding time and ramp-cool rate, were carried out.

Orlov *et al.* [105] demonstrated the introduction of the carbon impurity by annealing uranium ingot with carbon isotope additions from 550 to 950 °C. They concluded that the carbon impurity diffused into the uranium, and formed both the UC within uranium and U(CO) on the surface of the uranium. According to Nomine *et al.* [72], low solubility of each impurity in uranium

causes chemical compound such as the randomly distributed UC phase in U-Mo alloy. Burkes *et al.* [106] examined the mechanical behaviors of U10Mo alloy with carbon, nitrogen and oxygen impurities, and concluded that the failure mode from tensile test was sensitive to impurity content. Hoge [107] also found that carbon content below 250 ppm is desired to prevent reduction of ductility and tensile strength, based on deleterious mechanical effects of carbon on U10Mo alloys. The focus on current investigation is on the influence of UC and UO₂ on the diffusional bonding of U10Mo and Zr through co-rolling and HIP'ing. In this study, the anomalous features are the U10Mo–Zr bonding with limited interdiffusion and reaction (i.e., absence of distinguishable interaction zone consisting of α U, Mo₂Zr and UZr₂) typically impeded by the UC and UO₂ phases randomly present in the U10Mo alloy.

7.2. Experimental Parameters

The fabrication parameters for HIP process are: temperature, hold time and ramp-cool rate with pressure of 103 MPa. Table 3 summarized the sample ID for each condition for fabrication.

7.3. Results

7.3.1. Phase constituents and microstructure of typical features at U10Mo/Zr and Zr/AA6061 interfaces

Figure 42 presents a typical BSE micrograph of a specimen (56-345-280 in Table 3) produced according to the process described in Experimental Details. The light gray region in the middle is the U10Mo monolithic fuel, the dark gray region around is the AA6061 alloy, and the intermediate gray layer between is the Zr diffusion barrier. The sample identified “AR” without HIP does not have AA6061 alloy cladding. Figure 43 shows a typical BSE micrograph of the sample AR, which was fabricated by co-rolling of U10Mo alloy and Zr only (i.e., before HIP). The constituent phases observed in this sample by SEM are UZr_2 , Mo_2Zr and αU . The UZr_2 phase was adjacent to Zr, the αU phase was found between the UZr_2 and U10Mo. The Mo_2Zr was found as discontinuous precipitates within the αU phase. These agree well to the previous observation made by Perez *et al.* [39] who, in addition, found trivial presence of Zr and $\gamma\text{U}(\text{Zr})$ phases.

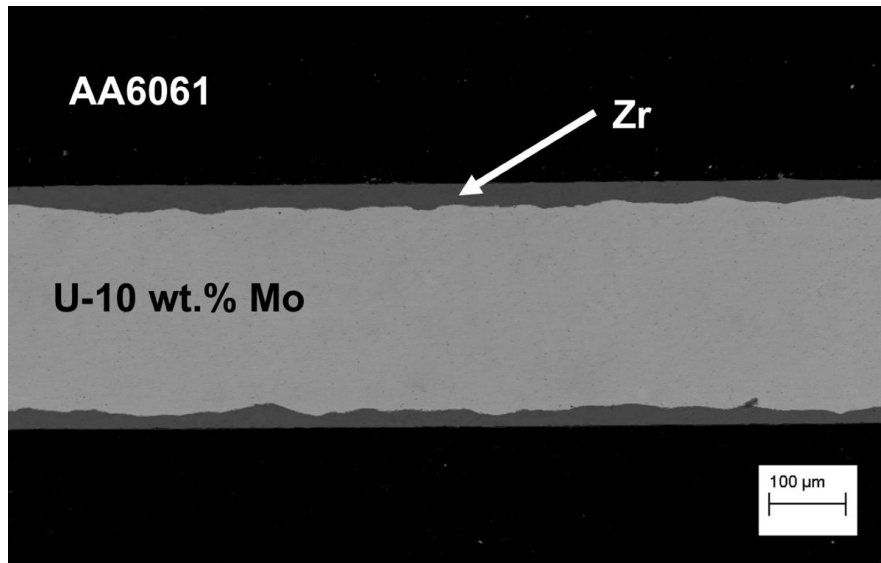


Figure 42. Typical backscatter electron micrograph of the U10Mo monolithic fuel encased in AA6061 with Zr diffusion barrier, produced by co-rolling and HIP'ing (sample 56-345-280, HIP'ed at 560 °C for 345 minutes with 280 °C/hour).

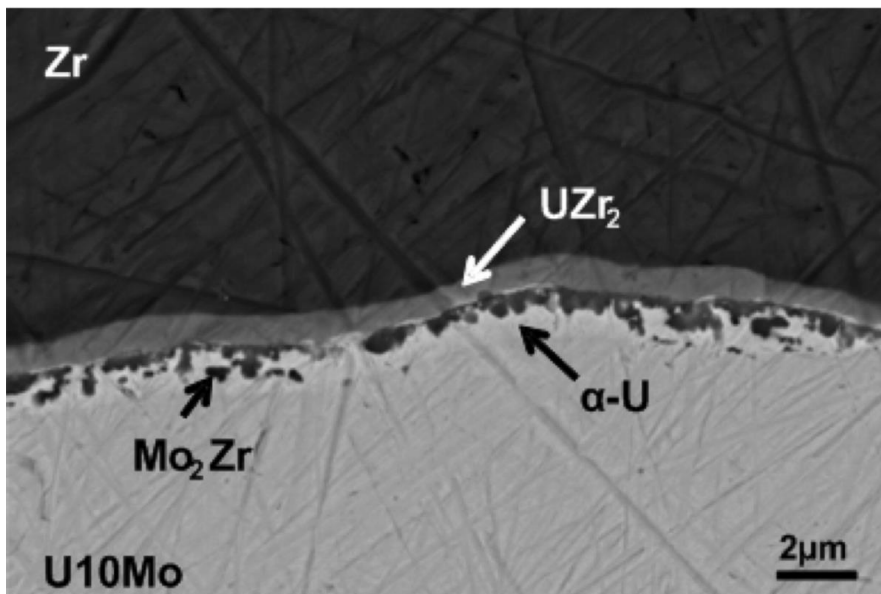


Figure 43. Backscatter electron micrograph from U10Mo monolithic fuel laminated with Zr diffusion barrier via co-rolling (sample AR, as co-rolled prior to HIP).

All HIP'ed fuel plate specimens exhibited similar microstructure, and representative results from the sample 56-345-280, which underwent a HIP procedure at 560 °C for 345 minutes with 280 °C/hour, are presented in Figure 44. In Figure 44(a), BSE micrograph shows that the interface between the U10Mo fuel and Zr diffusion barrier, even after HIP'ing at 560 °C for 345 minutes with 280 °C/hour, still consists of UZr_2 , Mo_2Zr and αU phases. Figure 44(b) shows the interface between Zr barrier and AA6061 cladding for the same sample. At this interface, only the $(\text{Al,Si})_3\text{Zr}$ phase was positively identified by SEM, contrary to various binary and ternary intermetallics observed by Perez *et al.* [39]. Therefore, TEM samples were prepared from the sample 56-345-280 at U10Mo-Zr and Zr-AA6061 interfaces.

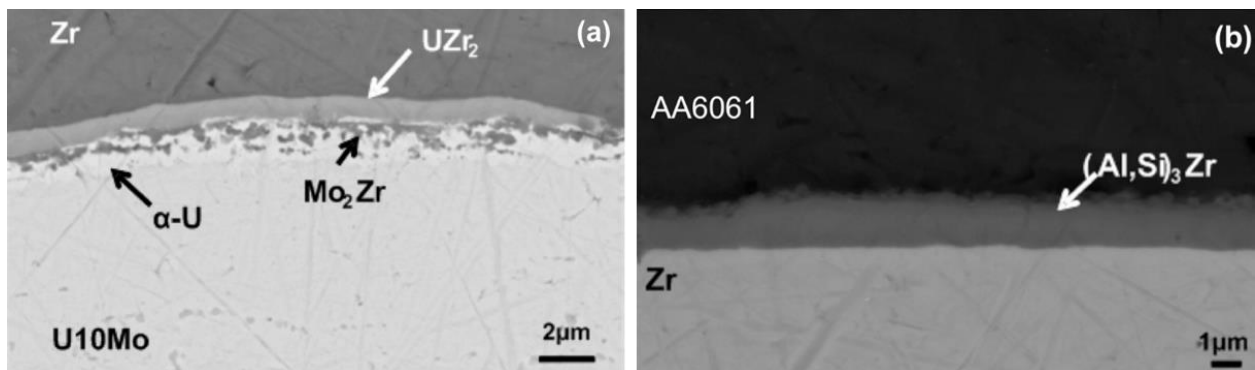


Figure 44. Backscatter electron micrographs from (a) the interface between U10Mo monolithic fuel and Zr diffusion barrier, and (b) the interface between Zr diffusion barrier and AA6061 cladding alloy (sample 56-345-280, HIP'ed at 560 °C for 345 minutes with 280 °C/hour).

The interfaces between the U10Mo and Zr, and the Zr and AA6061 were examined using analytical TEM using HAADF, SAED and XEDS. Figure 45 shows HAADF micrographs for (a) U10Mo-Zr interface, and (b) Zr-AA6061 interface from the sample 56-345-280. At the U10Mo-

Zr interface, a continuous layer of UZr_2 phase with an approximate composition of 34.1 at.% U - 3.6 at.% Mo - 62.3 at.% Zr was found adjacent to the Zr diffusion barrier. The αU having the composition of 99.8 at.% U with negligible amount of Mo and Zr was observed next to the UZr_2 phase containing the precipitates of Mo_2Zr with approximate composition of 6.0 at.% U – 59.6 at.% Mo – 34.4 at.% Zr. A small amount of Mo_2Zr precipitates was also found within the UZr_2 away from the Zr diffusion barrier: see arrow in Figure 45(a). These observations of phase constituents were augmented by SAED presented in Figure 46 for (a,b) $\gamma\text{U}_{10}\text{Mo}$, (c,d) αU , (e,f) Mo_2Zr , and (g,h) UZr_2 . SAED patterns from two zone axes are presented in Figure 46 for each phase. It should be noted that some distinction in contrasts in Figure 45 is a result of thickness variation, and do not represent other phases such as pure Zr and $\gamma\text{U}(\text{Zr})$ observed by Perez *et al.* [39] who identified these phases by qualitative XEDS and convergent beam diffraction (CBED) only. In this study, only the αU , Mo_2Zr , and UZr_2 were found by SAED as the products of diffusional interaction.

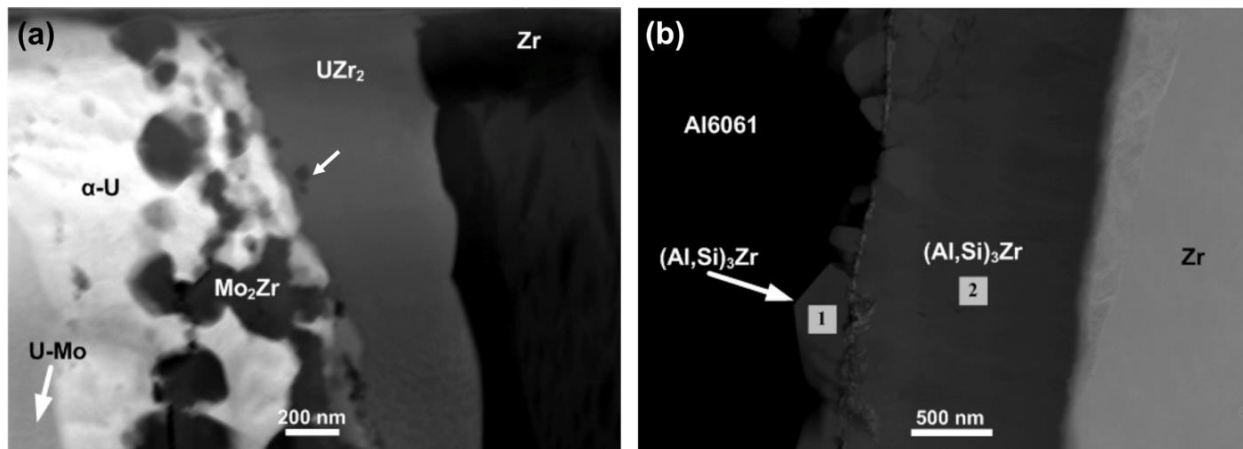


Figure 45. High angle annular dark field TEM micrographs from (a) the interface between U10Mo monolithic fuel and Zr diffusion barrier, and (b) the interface between Zr diffusion barrier and AA6061 cladding alloy (sample 56-345-280, HIP'ed at 560 °C for 345 minutes with 280 °C/hour). An arrow in (a) corresponds to the small Mo_2Zr precipitate found within the UZr_2 away from the Zr diffusion barrier.

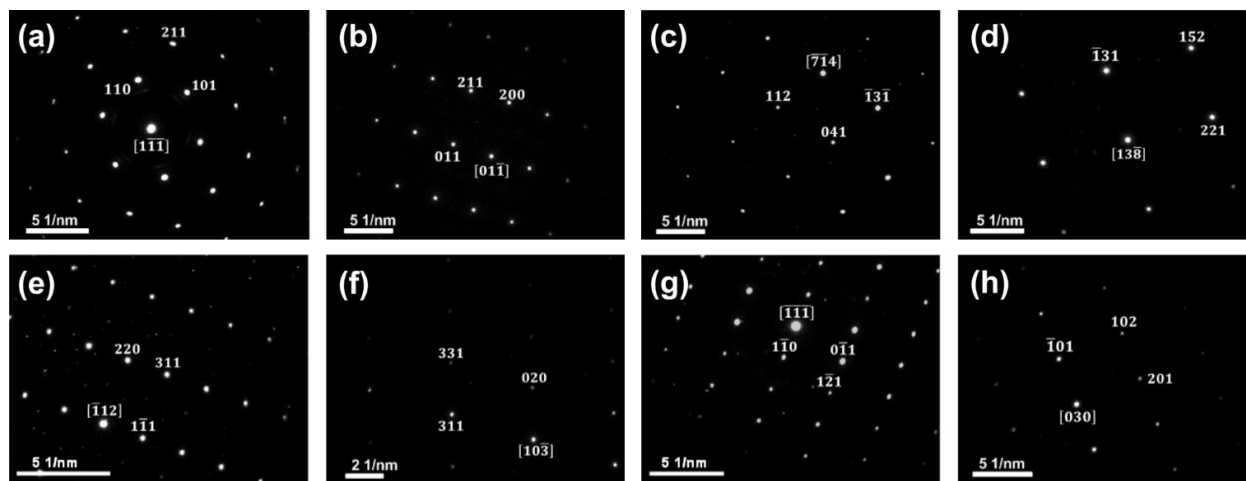


Figure 46. Selected area electron diffraction patterns from (a,b) $\gamma\text{U}(\text{Mo})$ solid solution, (c,d) αU , (e,f) Mo_2Zr , and (g,h) UZr_2 phases at the interface between U10Mo monolithic fuel and Zr diffusion barrier (sample 56-345-280, HIP'ed at 560 °C for 345 minutes with 280 °C/hour).

Figure 45(b) presents the product of diffusional interaction between the Zr diffusion barrier and AA6061 for the sample 56-345-280. A thick continuous layer of $(\text{Al,Si})_3\text{Zr}$ phase adjacent to the Zr was observed with SAED identification shown in Figure 47(a). An approximate composition of $(\text{Al,Si})_3\text{Zr}$ phase was determined to be 58.3 at.% Al - 14.2 at.% Si – 27.5 at.% Zr, although the Si content, and the corresponding Al content, varied from location to location. The protrusions shown in Figure 45(b) adjacent to the AA6061 cladding alloy was also identified by SAED as $(\text{Al,Si})_3\text{Zr}$ despite the difference in microstructure. The crystallographic information for all the phases observed in this study is summarized in Table 13.

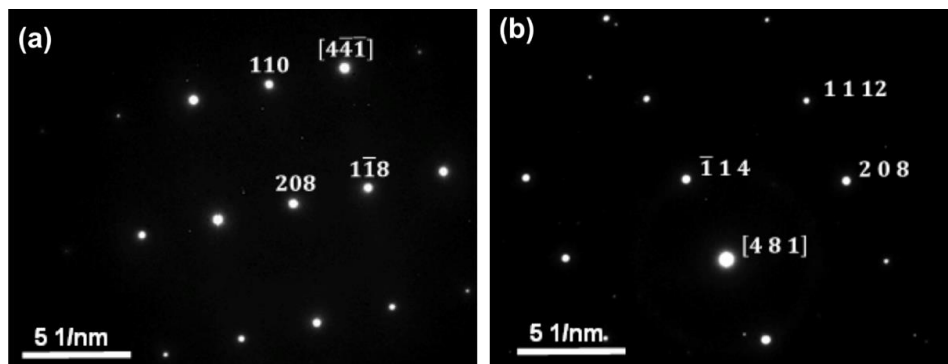


Figure 47. Selected area electron diffraction patterns from (a) the continuous layer of $(\text{Al,Si})_3\text{Zr}$ adjacent to Zr diffusion barrier and (b) the discontinuous $(\text{Al,Si})_3\text{Zr}$ protrusions adjacent to AA6061 at the interface between Zr diffusion barrier and AA6061 cladding alloy (sample 56-345-280, HIP'ed at 560 °C for 345 minutes with 280 °C/hour).

Table 13. Crystallographic information for all the phases observed by TEM in this investigation.

γ U	Pearson symbol	cI2
	Space group	Im3m (229)
	$a \times b \times c$ (Å)	$3.47 \times 3.47 \times 3.47$
	$\alpha \times \beta \times \gamma$ (°)	$90 \times 90 \times 90$
α U	Pearson symbol	oC4
	Space group	Cmcm (63)
	$a \times b \times c$ (Å)	$2.85 \times 5.86 \times 4.96$
	$\alpha \times \beta \times \gamma$ (°)	$90 \times 90 \times 90$
Mo ₂ Zr	Pearson symbol	cF24
	Space group	Fd3m (227)
	$a \times b \times c$ (Å)	$7.58 \times 7.58 \times 7.58$
	$\alpha \times \beta \times \gamma$ (°)	$90 \times 90 \times 90$
UZr ₂	Pearson symbol	hP3
	Space group	P6/mmm (191)
	$a \times b \times c$ (Å)	$5.03 \times 5.03 \times 3.08$
	$\alpha \times \beta \times \gamma$ (°)	$90 \times 90 \times 120$
(Al,Si) ₃ Zr	Pearson symbol	tI16
	Space group	I4/mmm (139)
	$a \times b \times c$ (Å)	$4.01 \times 4.01 \times 17.28$
	$\alpha \times \beta \times \gamma$ (°)	$90 \times 90 \times 90$

7.3.2. Diffusion and kinetics analyses at U10Mo/Zr and Zr/AA6061 interfaces

The numerical data were measured using at least 12 random locations for each direction of each sample (i.e., longitudinal and transverse). Figure 48 shows the measured thickness of the interaction layer between the U10Mo and Zr barrier after HIP'ing at 560 °C as a function of time. The layer consisting of the α U, Mo₂Zr, and UZr₂ phases did not exhibit any significant growth given the standard deviation. It is important to note that this insignificant growth is not a result of experimental error or uncertainty, since the growth of the (Al,Si)₃Zr interaction layer was clearly observed at the interface between Zr and AA6061 in the same samples as presented in Figure 49. Thus, to improve the adhesion quality of fuel plate at the interface between the U10Mo and Zr barrier, HIP can be carried out for prolonged period without apprehension for the excessive growth of the interaction layer consisting of α U, Mo₂Zr, and UZr₂ at the U10Mo/Zr interface.

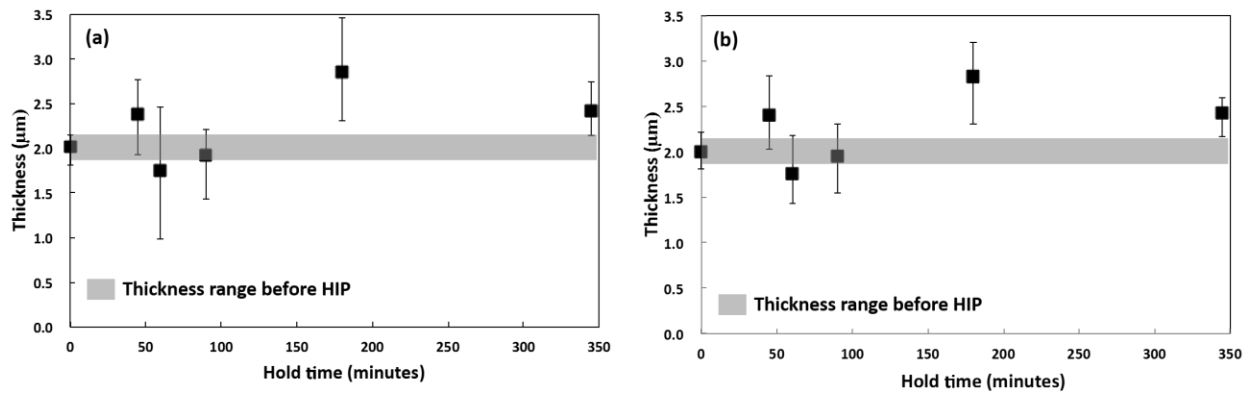


Figure 48. Measured thickness of interaction layer between the U10Mo monolithic fuel and Zr barrier after HIP'ing at 560 °C as a function of time in (a) longitudinal and (b) transverse directions.

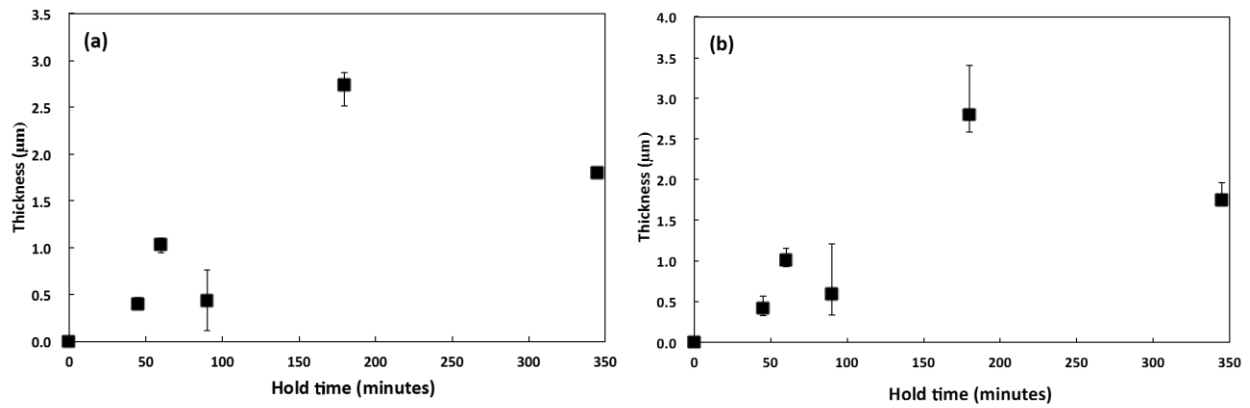


Figure 49. Measured thickness of interaction layer between the Zr barrier and AA6061 after HIP'ing at 560 °C as a function of time in (a) longitudinal and (b) transverse directions.

Similar observation was made as a function of HIP temperature ranging from 520 to 580 °C. Figure 50 presents the measured thickness of interaction layer between U10Mo and Zr barrier after HIP'ing for 90 minutes as a function of temperature. A remarkable stability of the interaction layer thickness was observed. Again, the growth of the $(Al,Si)_3Zr$ interaction layer was clearly observed as a function of HIP temperature at the interface between Zr and AA6061 in the same samples as presented in Figure 51. This demonstrates that the insignificant growth observed at the U10Mo/Zr interface is genuine, and HIP can be carried out with a variation in temperature from 520 to 580 °C without apprehension for the excessive growth of the interaction layer consisting of αU , Mo_2Zr , and UZr_2 at the U10Mo/Zr interface.

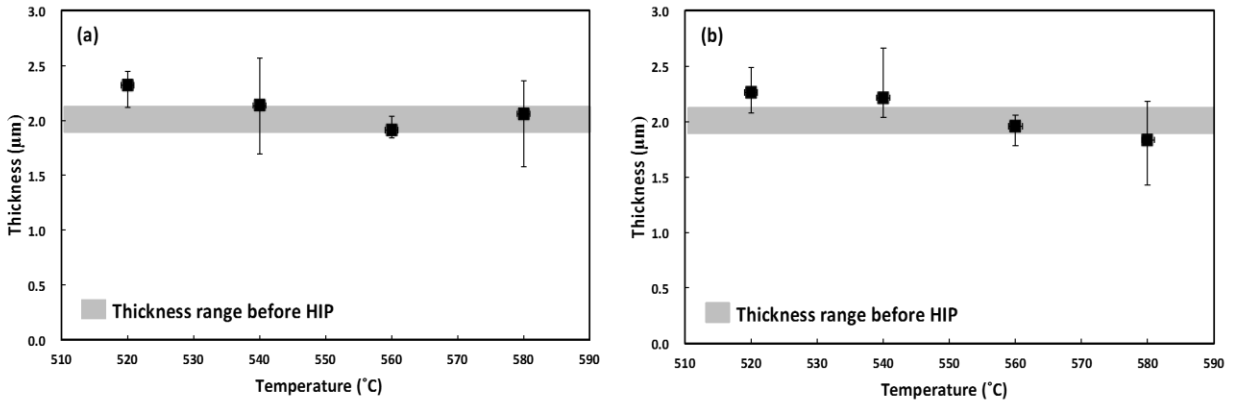


Figure 50. Measured thickness of interaction layer between the U10Mo monolithic fuel and Zr barrier after HIP'ing for 90 min as a function of temperature range from 520 to 580 °C in (a) longitudinal and (b) transverse directions.

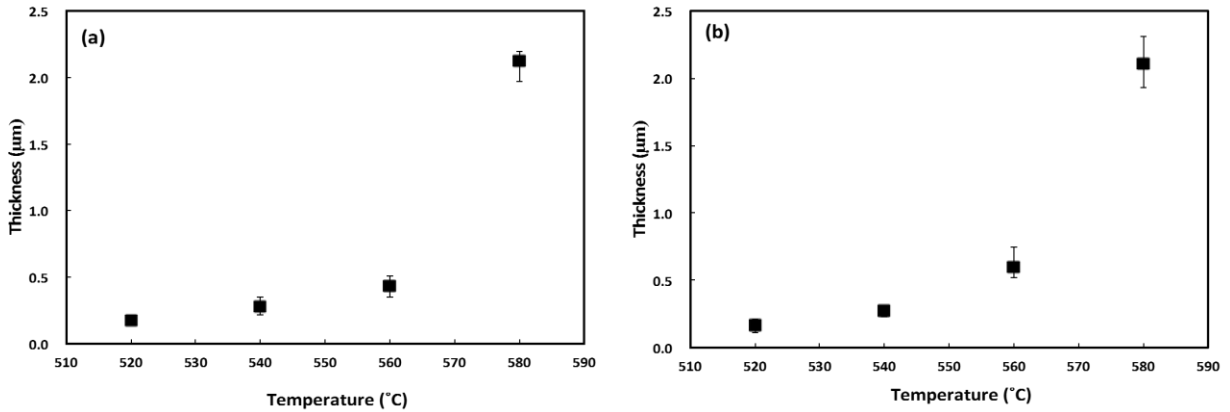


Figure 51. Measured thickness of interaction layer between the Zr barrier and AA6061 after HIP'ing for 90 min as a function of temperature range from 520 to 580 °C in (a) longitudinal and (b) transverse directions.

Growth kinetics analyses for the diffusional interaction between the U10Mo fuel and Zr barrier could not be carried out since there was no observable growth given the time and temperature ranges examined in this investigation. For the growth of interaction layer between the Zr diffusion barrier and AA6061, correlations between the thickness and HIP parameters, namely the temperature and time was established using the assumption of diffusion-controlled growth, Equation (3), and Arrhenius temperature-dependence, Equation (4). The growth of diffusional interaction layer between the Zr diffusion barrier and AA6061 during HIP'ing at 560 °C was examined as a function of time to yield a growth constant of $k_p \sim 0.015 \text{ m/sec}^{-1/2}$. The temperature-dependence of k_p , as seen in Figure 52 followed the Arrhenius behavior, and yielded a growth activation energy of $448.57 \pm 23.92 \text{ kJ/mol}$ in rolling direction and $466.51 \pm 31.27 \text{ kJ/mol}$ for the transverse direction. Given the standard deviation determined from the variation in thickness measurement, these two values of activation energy are similar regardless of direction observed. Calculated growth constants from each sample, averaged among both longitudinal and transverse directions are reported in Table 14.

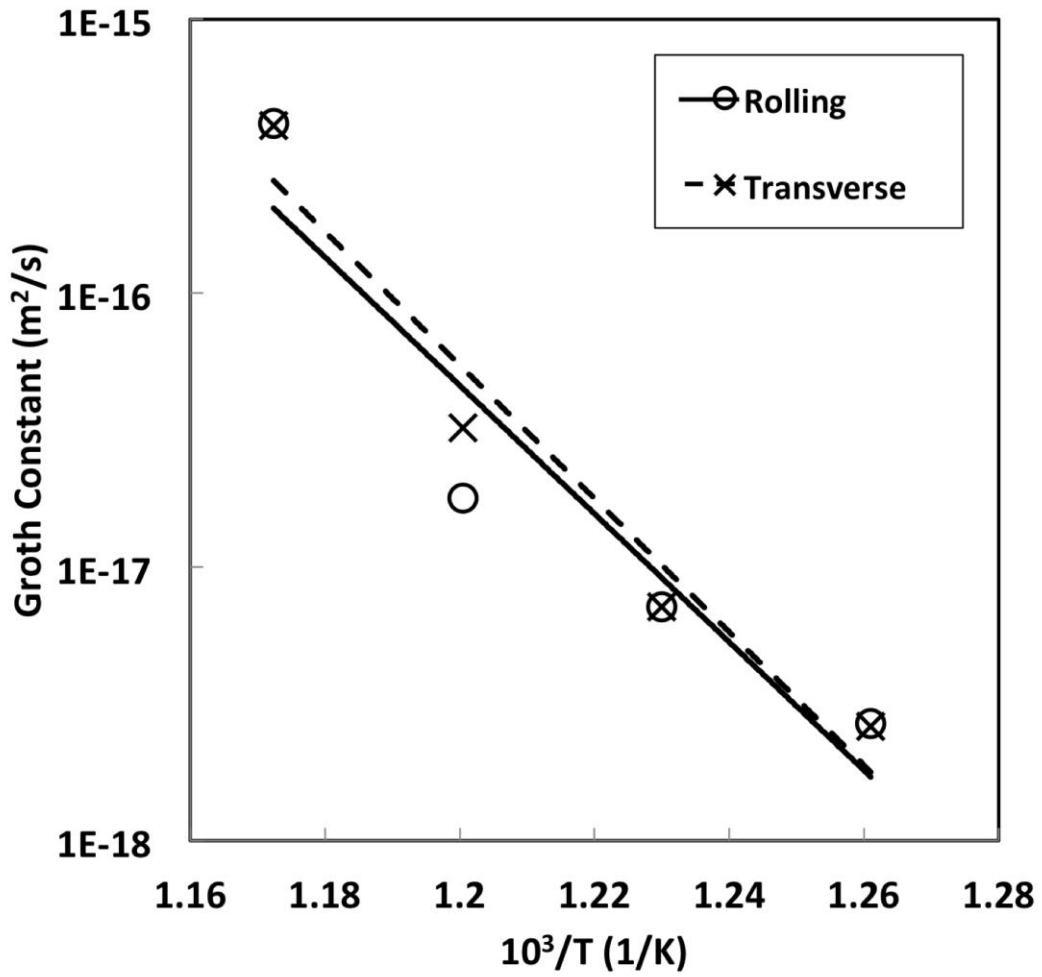


Figure 52. Temperature dependence of growth constant determined for the interaction layer developed at the interface between the Zr barrier and AA6061 during HIP'ing.

Table 14. The average growth constants and activation energy calculated from the layer growth at the interface between Zr and AA6061 as functions of HIP parameters.

Sample	Thickness (μm)	k_p (m^2/s)	Q (kJ/mol)
52-90-280	0.169	2.64×10^{-18}	457.54 \pm 27.60
54-90-280	0.278	7.16×10^{-18}	
56-45-280	0.405	3.03×10^{-17}	
56-60-280	1.017	1.44×10^{-16}	
56-90-280	0.515	2.45×10^{-17}	
56-180-280	2.769	3.55×10^{-16}	
56-345-280	1.777	7.63×10^{-17}	
58-90-280	2.114	4.14×10^{-16}	

7.3.3. Phase transformation of γ U within U10Mo

The AR sample before HIP process exhibited a small amount of cellular structure which consists of α U, γ U and γ' as shown in Figure 53. The cellular structure is assumed as the initial feature prior to development of lamellar structure, and is also assumed to nucleate at heterogeneous sites, such as grain boundaries. Only the cellular structure without any lamellar features were observed in the AR sample. The cellular structure is also characterized by the Mo depleted regions surrounding the Mo-rich γ' nuclei as shown by the inset in Figure 53. Based on these observations, AR sample is assumed to exhibit features characteristic of an U10Mo alloy corresponding to a time coordinate of 25 hours in the U10Mo TTT diagram as labeled in Figure 7. In other words, subsequent HIP and the corresponding characterization results assume that the starting coordinates for U10Mo alloy fuel in TTT diagram is at 25 hours as labeled in Figure 7.

Figure 54 shows microstructure of U10Mo fuel alloy HIP'ed at 560 °C for 90 hours with a RC rate variation of 280, 70 and 35 °C/hour. The micrograph in Figure 54(a) from the U10Mo alloy with the higher RC rate of 280 °C/hour shows cellular regions along grain boundaries of U10Mo alloy. Cellular structure is better defined than the AR sample, and some of the cellular reaction was observed within the grains of the U10Mo solid solution. For U10Mo alloy HIP'ed with RC rate of 70 °C/hour, a clear development of lamellar structure was observed in addition to the cellular structure as shown in Figure 54 (b). The lamellar structure is assumed to begin from the cellular precipitates along the grain boundaries, and grow into the grain of γ -(U10Mo). The largest volume fraction of lamellar structure region was observed in the sample with 35 °C/hour RC rate. The lamellar structure of α and γ' is presented in detail with a higher magnification BSE

micrograph in Figure 55. Figure 56 shows that the volume fraction estimated for the lamellar structure region resulting from decomposition of γ increases as the RC rate decreases. This observation corresponds to the fact that slow RC rate exposes the U10Mo alloy in the three phase ($\alpha+\gamma+\gamma'$) region the longest as illustrated on the TTT diagram in Figure 57.

A selected region highlighted by black rectangle in Figure 54 (c) was prepared by FIB-INLO for TEM analyses presented in Figure 58 and Figure 59. The SAED patterns presented in Figure 59 were collected from circled regions in Figure 58 (a). The HAADF and bright-field images shown in Figure 58 along with SAED patterns presented in Figure 59 were employed to identify the decomposition of BCC- γ into alternating orthorhombic- α and tetragonal- γ' lamellar structure. Other regions consisted of γ and α , without γ' . Therefore, the presence of transition region from $\alpha+\gamma$ to $\alpha+\gamma+\gamma'$ in the TTT diagram appears to be consistent with the current TEM analyses.

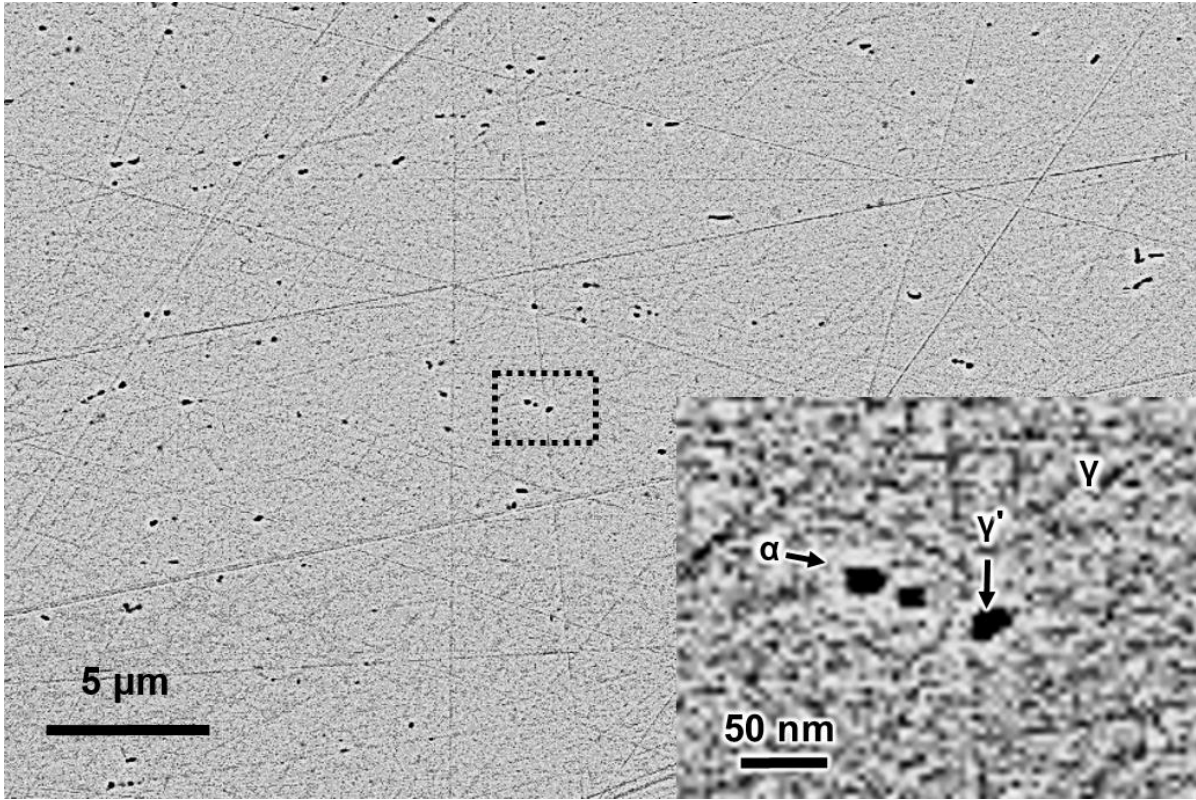


Figure 53. Cellular structure resulted from decomposition of γ into α and γ' in the microstructure of AR sample.

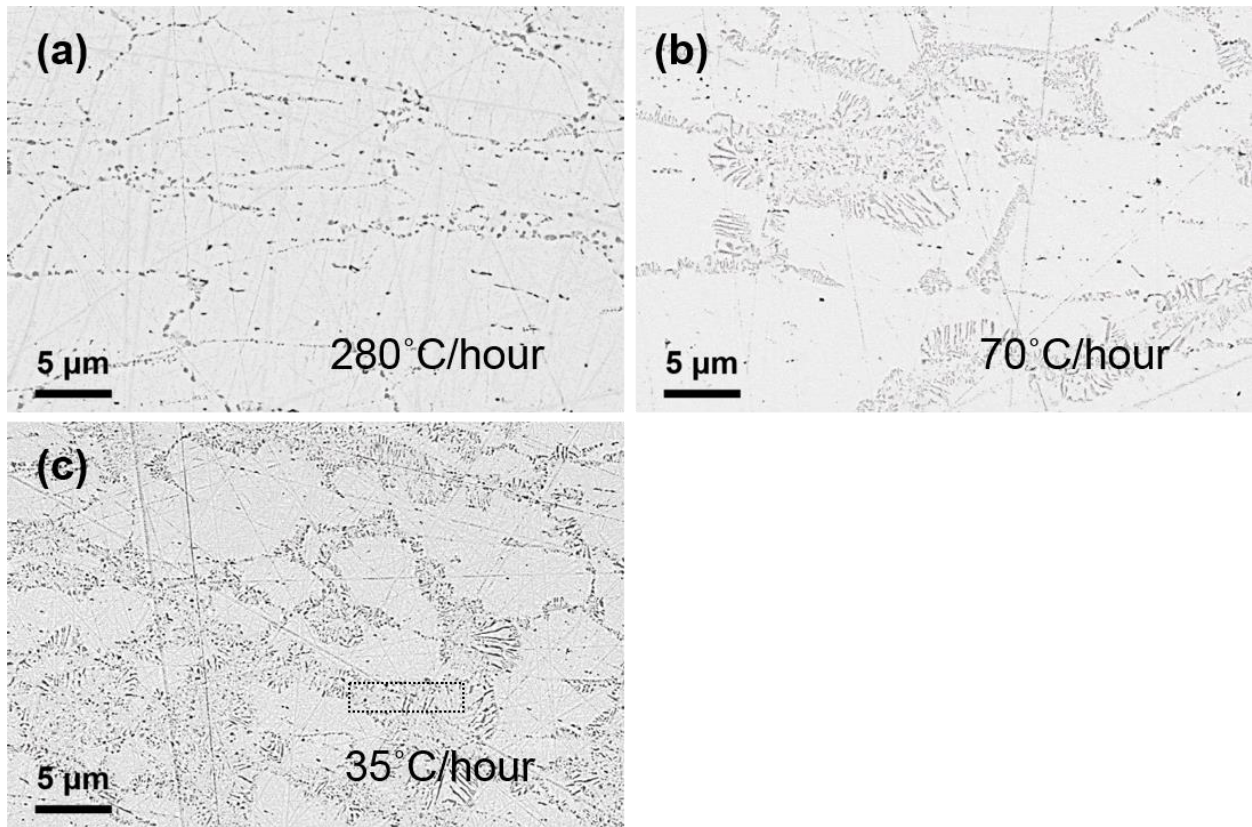


Figure 54. Backscattered electron micrographs for the U10Mo of HIP fuel plates co-rolled at 560 °C for 90 minutes with variation in ramping and cooling rate: (a) 280, (b) 70, and (c) 35 °C/hour.

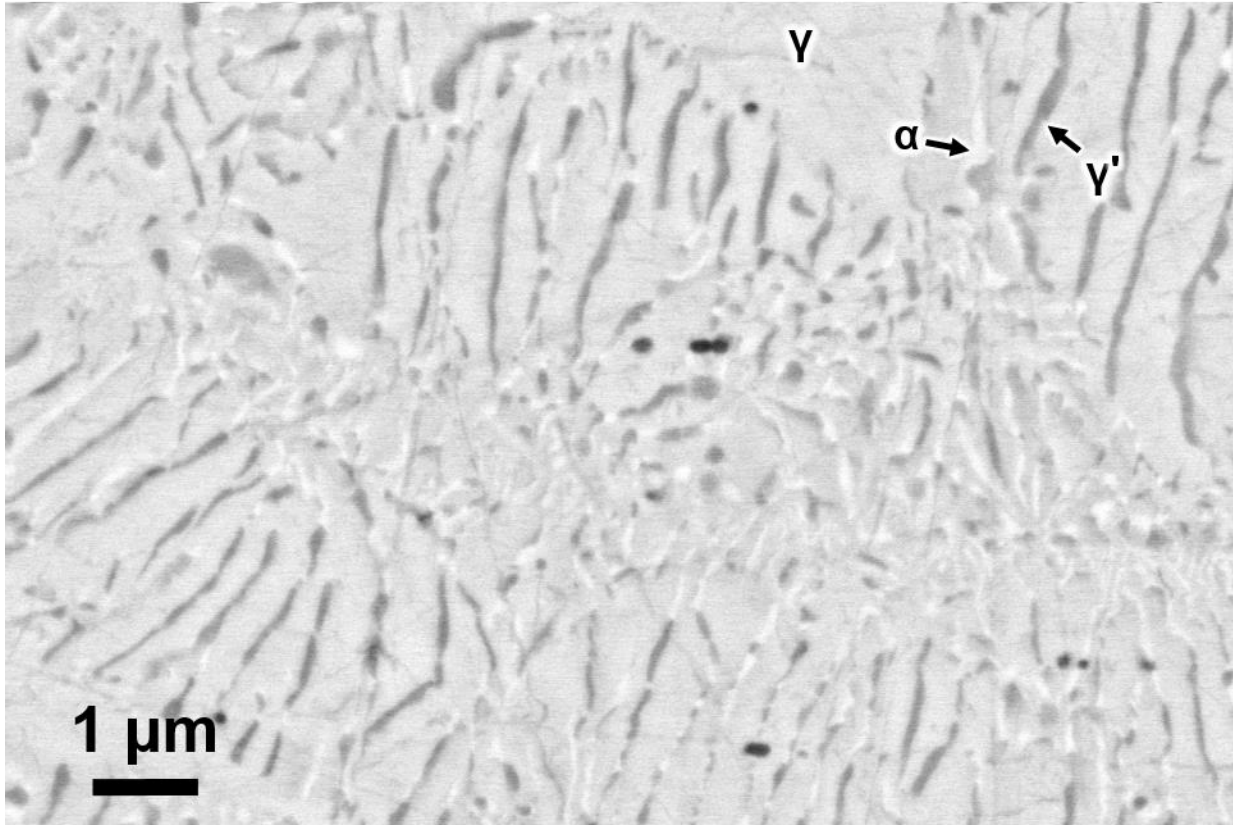


Figure 55. High magnification BSE of lamellar structure for the U10Mo of HIP fuel plates controlled at 560 °C for 90 minutes with ramping and cooling rate of 35 °C/hour.

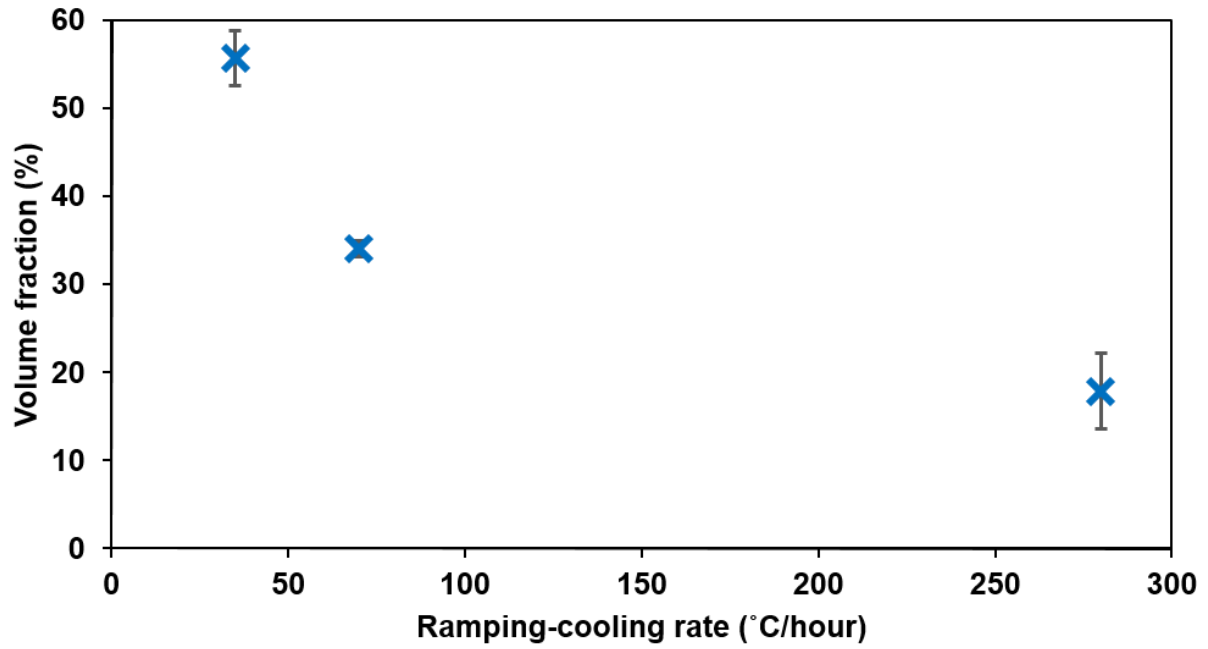


Figure 56. The volume fraction of decomposed constituents area in the U10Mo alloy as a function of ramping and cooling rate.

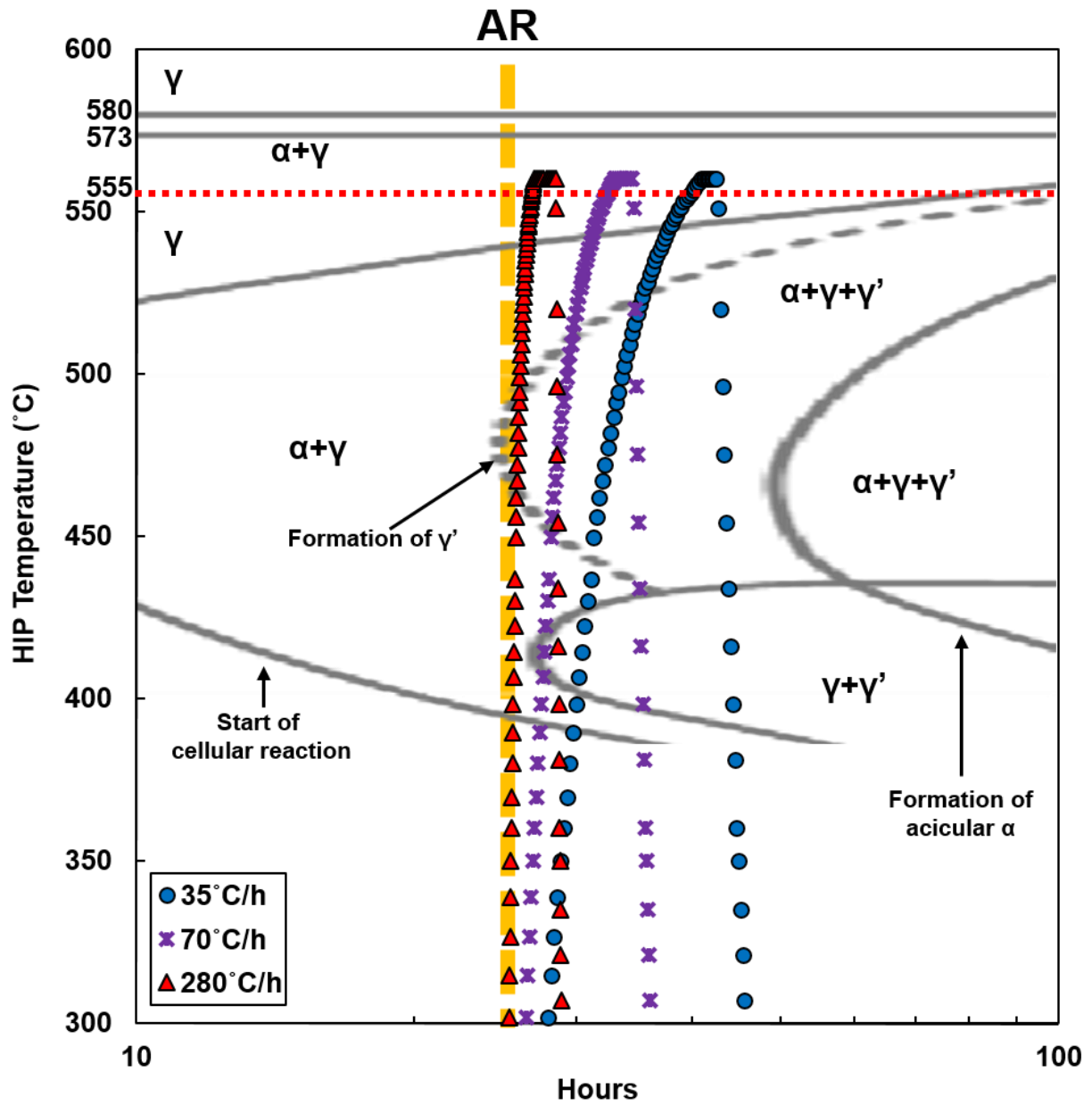


Figure 57. The heat treatment traces on the TTT diagram of U10Mo for the ramping and cooling rates of 35, 70 and 280 °C/hour at 560 °C for 90 minutes.

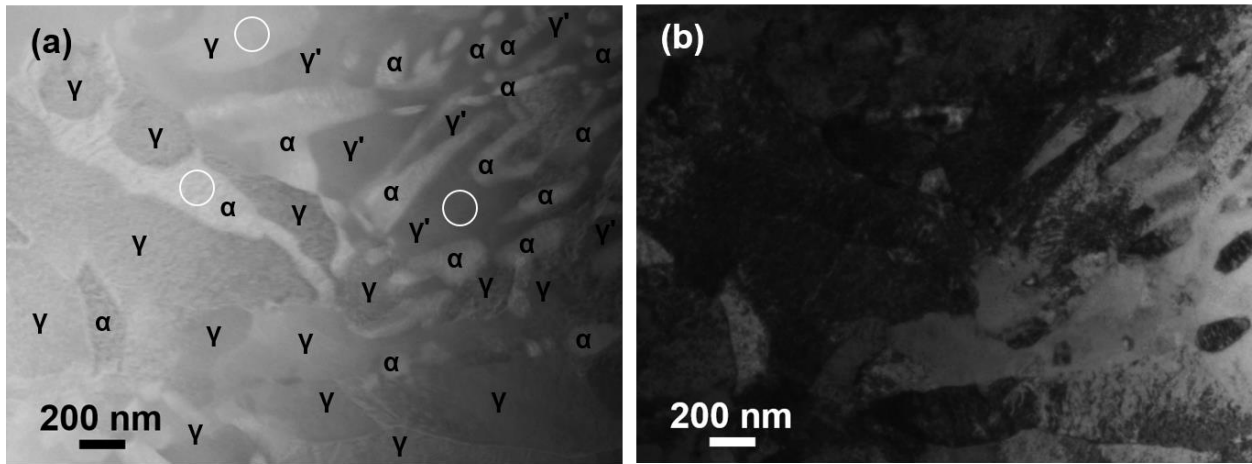


Figure 58. TEM (a) HAADF and (b) BF micrographs for the reaction zone by decomposition of γ U10Mo into α U and γ' U₂Mo in 56-90-35 HIP'ed at 560 °C for 90 minutes with 35 °C/hour.

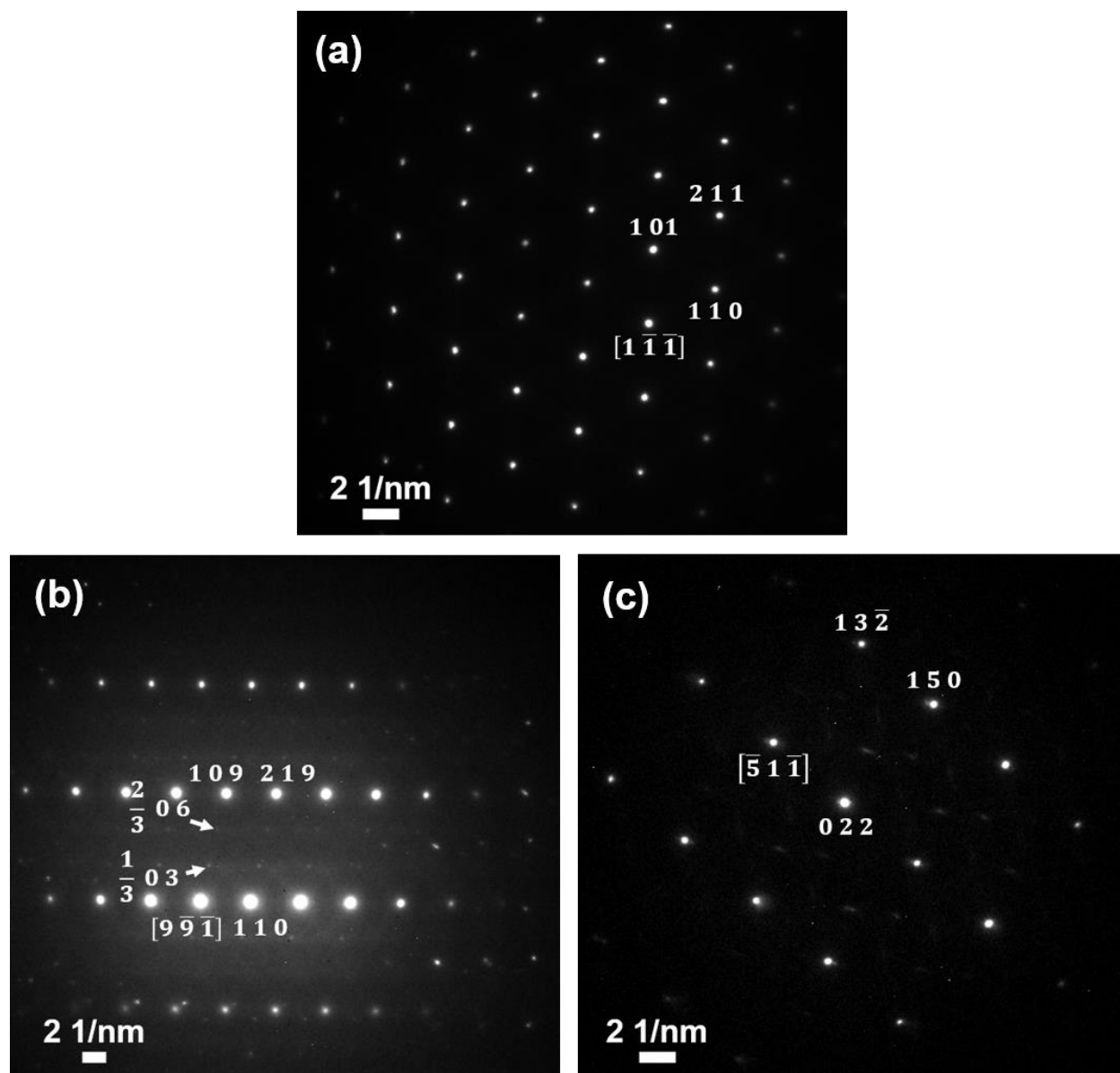


Figure 59. Selected area electron diffraction patterns from the decomposition reaction zone of 56-345-35 HIP'ed at 560 °C for 345 minutes with 35 °C/hour (a) $\gamma\text{U}_{10}\text{Mo}$, (b) $\gamma\text{U}_2\text{Mo}$ and (c) αU .

Figure 60 shows microstructural variation in U10Mo fuel alloy as a function of HIP temperature. The time at HIP temperature and RC rate remained constant for 90 minutes and 280°C/hour, respectively, for these samples. In general, the volume fractions of cellular and lamellar structure regions decreased with an increase in HIP temperature as presented in Figure 61. The HIP temperature variation examined in this study is close to the transition that separates γ and $\alpha+\gamma$ (and $\alpha+\gamma$ and γ) on the upper-left-corner of the TTT- diagram as presented in Figure 62.

Effects of HIP holding time was examined with U10Mo alloys HIP'ed at 560°C with RC rate of 280°C/hour as presented in Figure 63. There was no significant change in the amount of decomposed region because, upon heating, a transformation from $\alpha+\gamma'$ (or $\alpha+\gamma+\gamma'$) into $\alpha+\gamma$ in the temperature range of 555 to 580°C is expected as shown in Figure 64. Given the HIP temperature of 560°C, the volume fraction of decomposed region showed no significant trend with HIP holding time, up to 345 minutes, as shown in Figure 65.

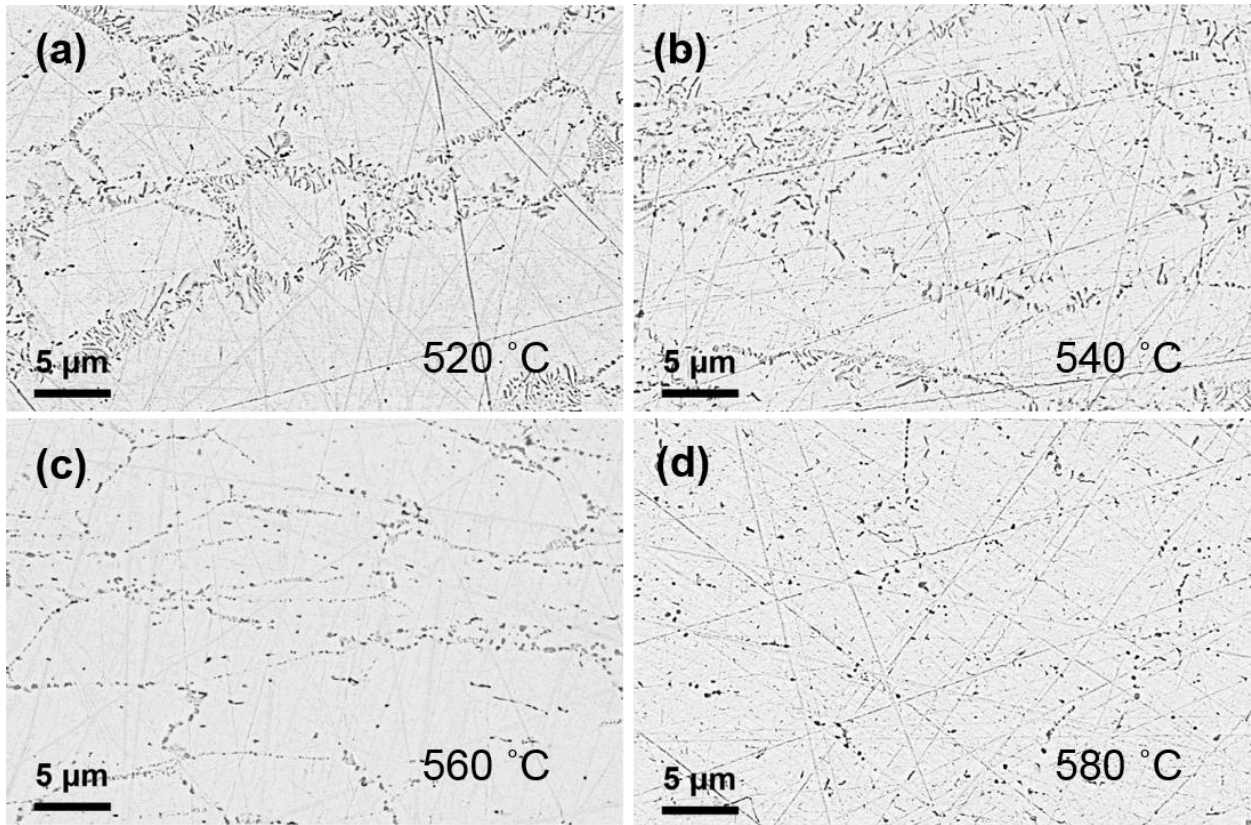


Figure 60. Backscattered electron micrographs for the U10Mo of HIP fuel plates co-rolled for 90 minutes with ramping and cooling rate of 280 °C/hour at: (a) 520, (b) 540, (c) 560 and (d) 580 °C.

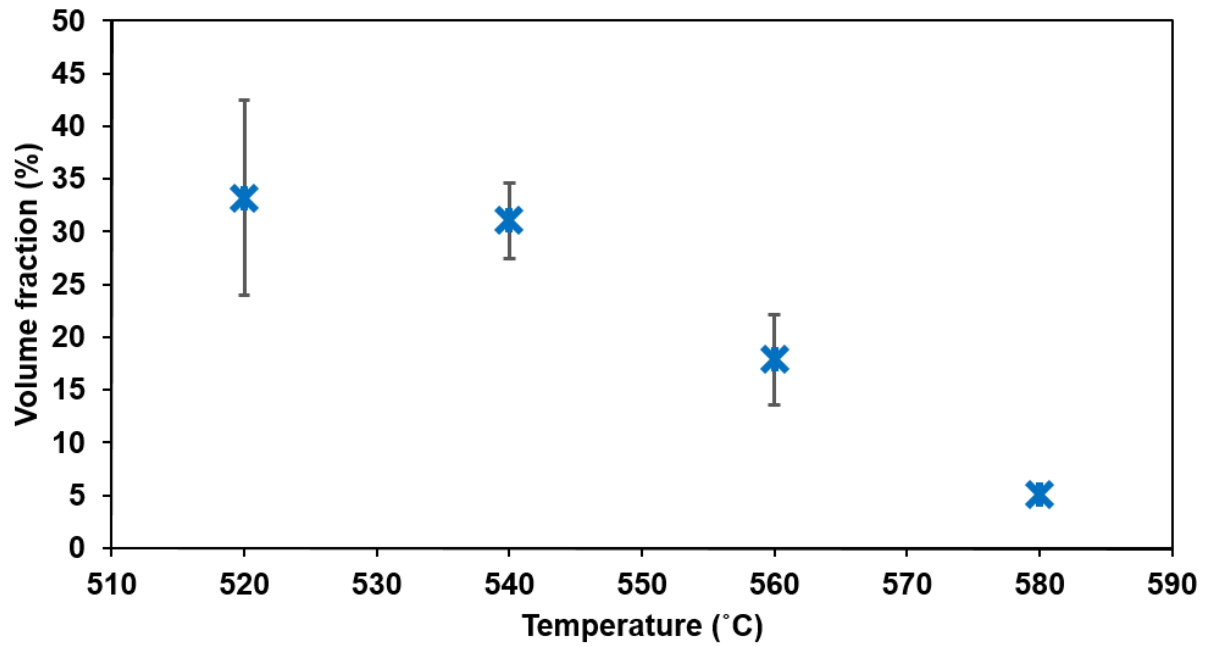


Figure 61. The volume fraction of decomposed constituents area in the U10Mo alloy as a function of HIP'ed temperature.

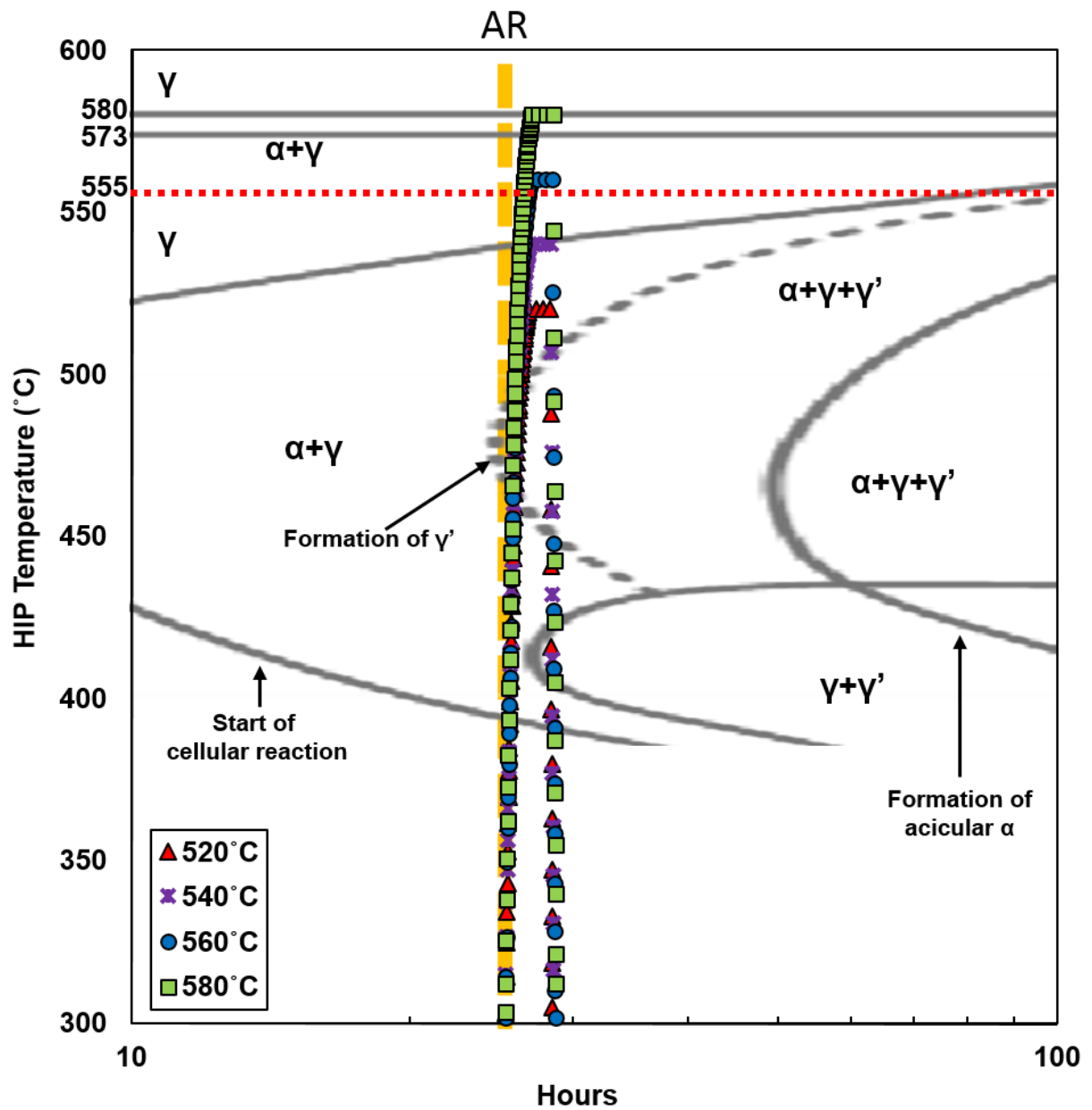


Figure 62. The heat treatment traces on the TTT diagram of U10Mo for the HIP'ed temperature of 520, 540, 560 and 580 °C for 90 minutes with 280 °C/hour.

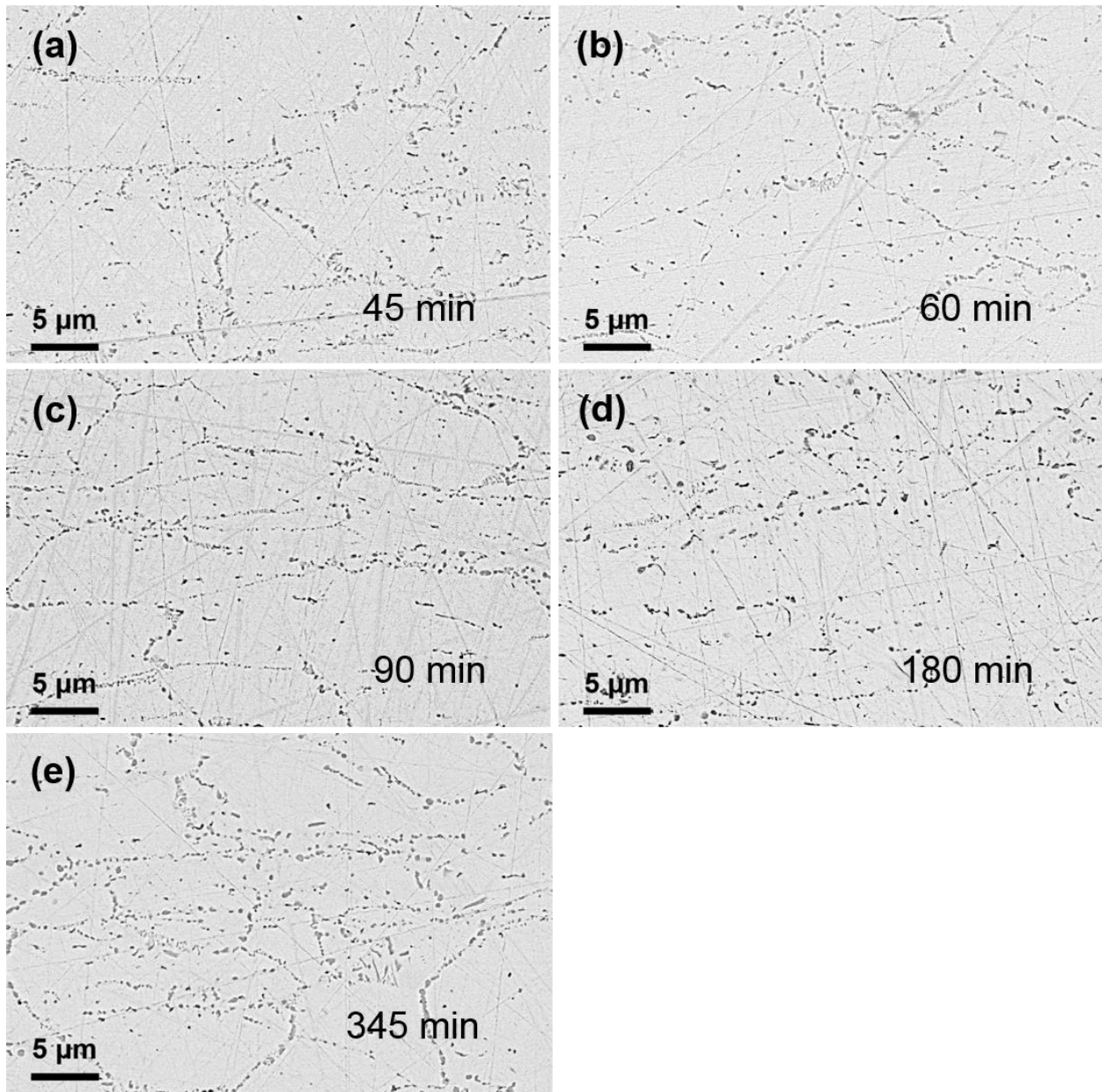


Figure 63. Backscattered electron micrographs for the U10Mo of HIP fuel plates co-rolled at 560 °C with ramping and cooling rate of 280 °C/hour for: (a) 45, (b) 60, (c) 90, (d) 180 and (e) 345 minutes.

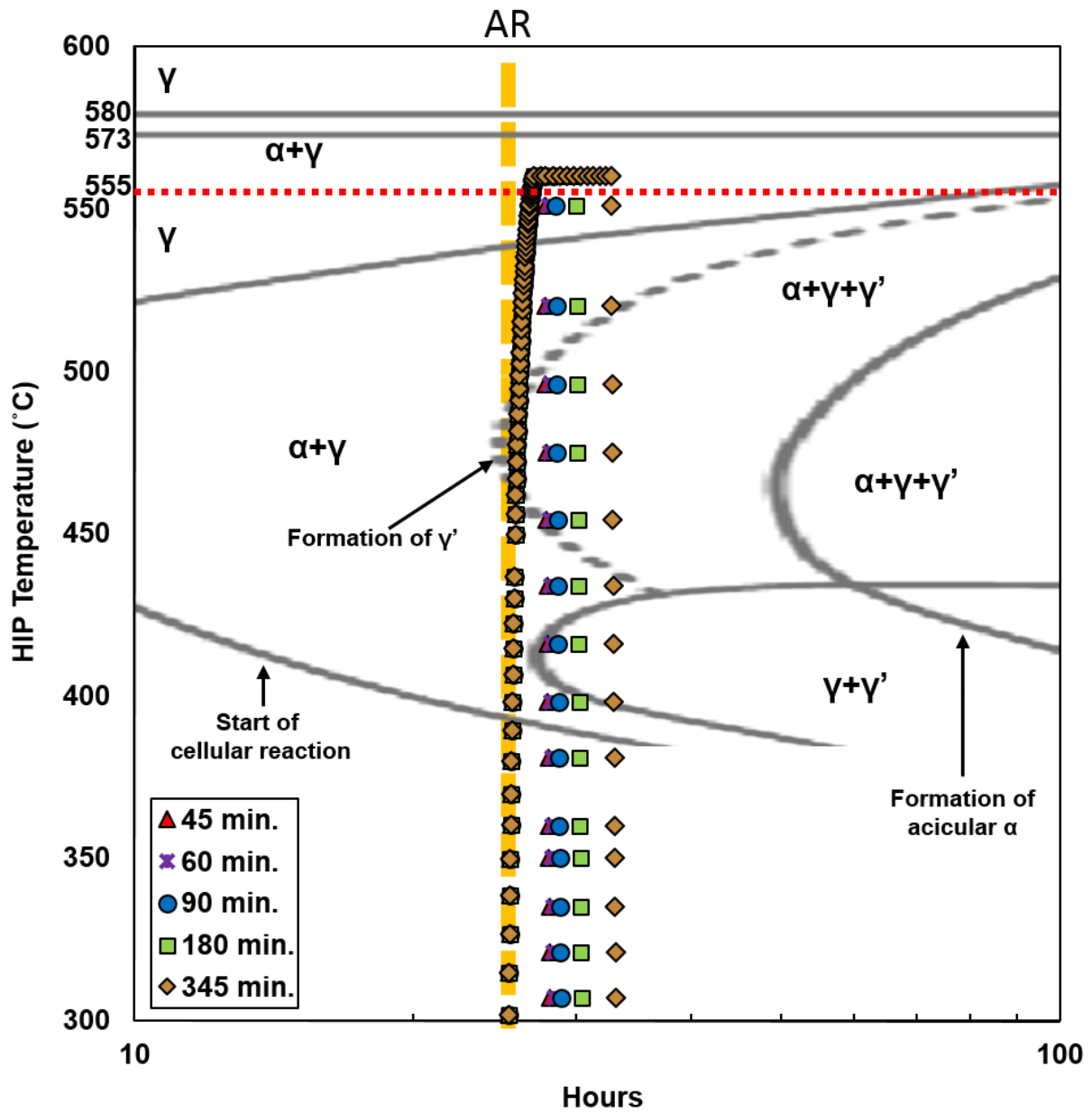


Figure 64. The heat treatment traces on the TTT diagram of U10Mo for the HIP'ed holding time of 45, 60, 90, 180 and 345 minute at 560 °C with 280 °C/hour.

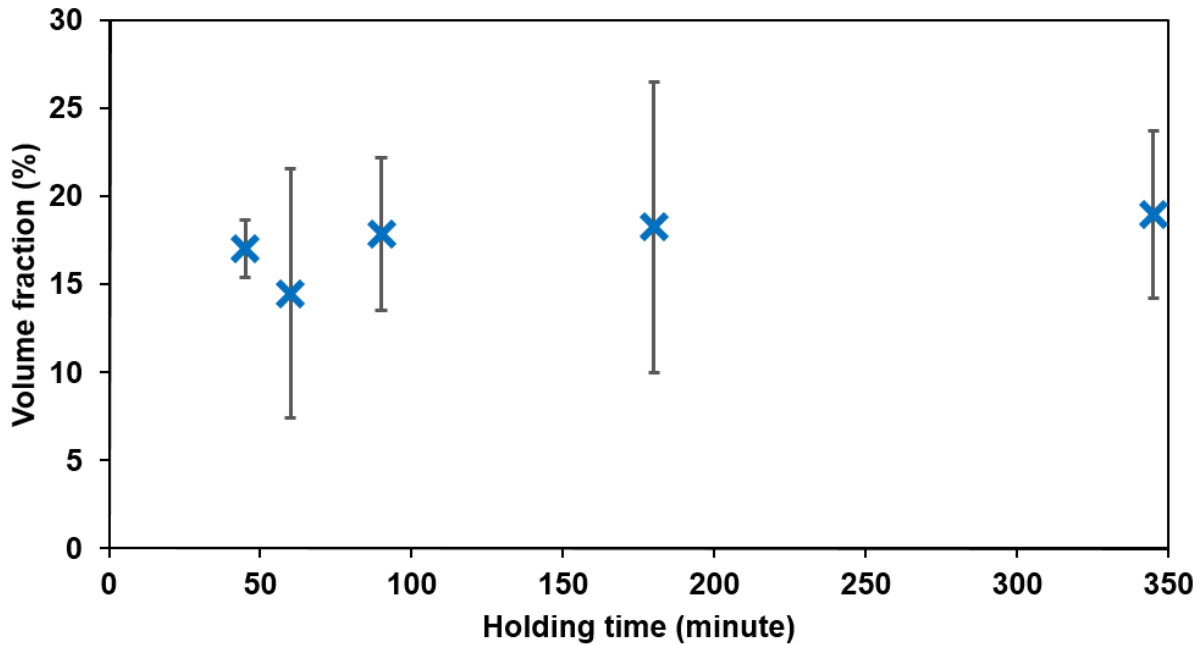


Figure 65. The volume fraction of decomposed constituents area in the U10Mo alloy as a function of HIP'ed temperature.

7.3.4. Phase constituents and microstructure of anomalous features

There were several randomly-distributed inclusions (identified as UC and UO₂ by TEM) observed within the U10Mo alloys, and some located near the interface between the U10Mo alloy and α Zr diffusion barrier appeared to influence the phase and microstructural development. Figure 66 presents BSE micrographs that are considered “microstructural anomalies” in this investigation: Figure 66(a) presents a BSE micrograph from the region where apparent presence of these inclusions has limited the interdiffusion and reaction between U10Mo and Zr diffusion barrier; Figure 66(b) presents a BSE micrograph from the region where limited interdiffusion and reaction

was observed between U10Mo and Zr diffusion barrier without the apparent presence of the inclusions, at least by SEM. Two TEM samples were prepared by FIB-INLO as indicated in Figure 66 to elucidate the phase constituents of the inclusions and characterize the regions of limited interdiffusion and reaction. The region of limited interaction in Figure 66(a) to the right-hand-side of the apparent UC and UO₂ inclusions, is assumed to be similar to that presented in Figure 66(b) studies by TEM.

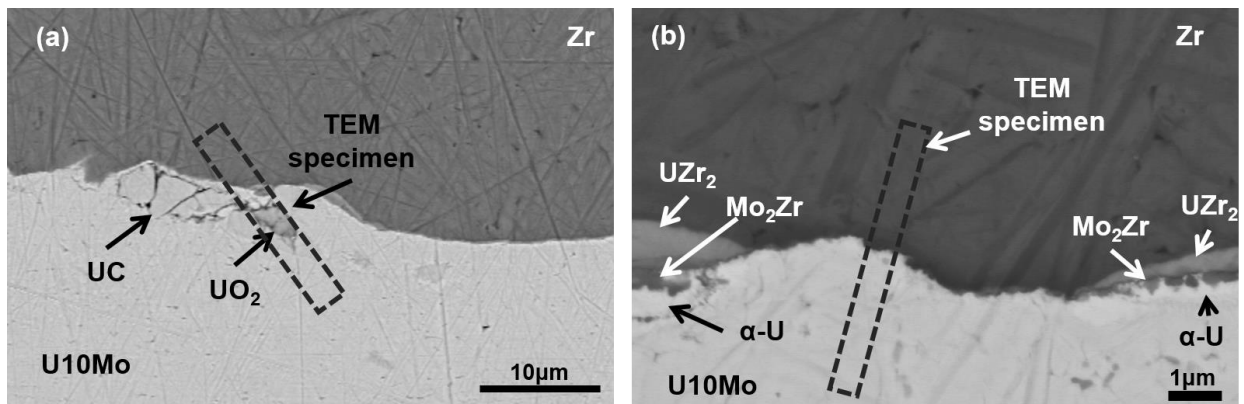


Figure 66. (a) Anomalous microstructure associated with the UC and UO₂ phases, and (b) the imperfect reaction zone in U10Mo alloy (from sample 56-345-280, HIP'ed at 560 °C for 345 minutes with 280 °C/hour).

Figure 67 presents (a) HAADF scanning TEM (STEM) and (b) BF micrographs of inclusions in TEM sample prepared from Figure 66(a). The UC phase was identified via SAED patterns along the $[\bar{1} 1 2]$ and $[1 \bar{1} \bar{1}]$ beam directions as shown in Figure 68. The UO₂ phase, consisted of many fine grains, some containing a significant amount of C, was identified by HR-TEM micrographs with fast Fourier transformation (FFT) analyses as presented in Figure 69. The UC and UO₂ phases were identified as cF8, Fm-3m (225) with $a = 4.955 \text{ \AA}$ and cF12, Fm-3m (225)

with $a = 5.467 \text{ \AA}$, respectively. The crystallographic details for the UC and UO_2 phases along with typical chemical compositions observed by semi-quantitative standard-less XEDS are reported in Table 15.

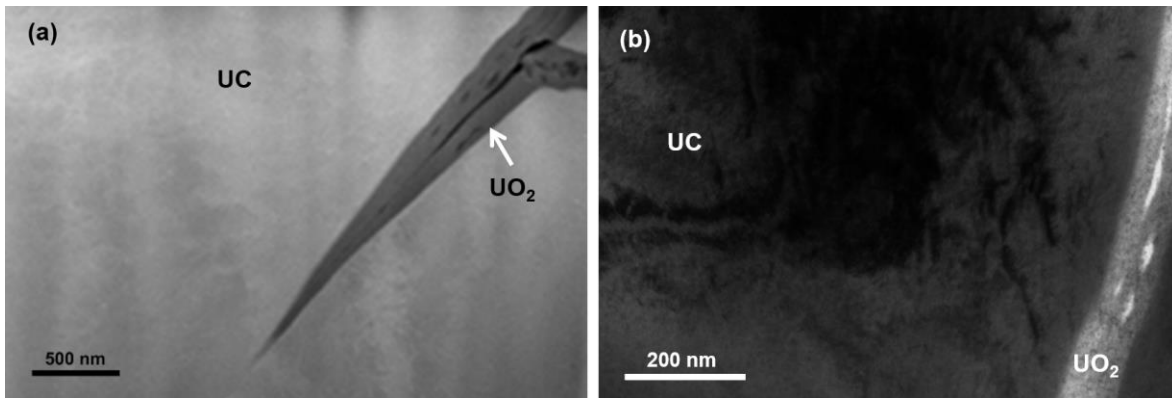


Figure 67. (a) High angle annular dark field (HAADF) scanning transmission electron microscopy (STEM) micrograph and (b) bright field (BF) micrograph from the UC and UO_2 inclusion phases (TEM specimen prepared from Figure 66(a) from sample 56-345-280, HIP'ed at $560 \text{ }^\circ\text{C}$ for 345 minutes with $280 \text{ }^\circ\text{C}/\text{hour}$).

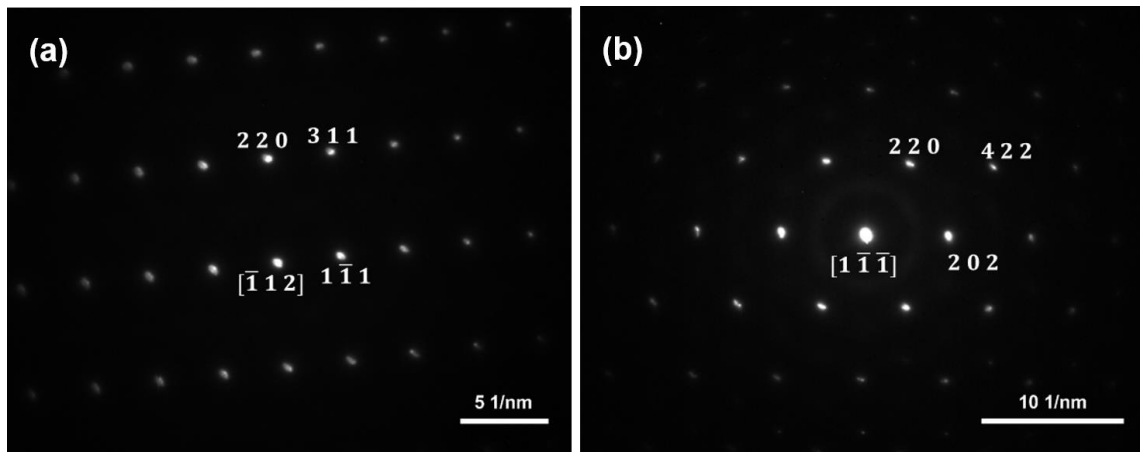


Figure 68. Selected area electron diffraction patterns from the UC phase in (a) $[\bar{1} 1 2]$ and (b) $[1 \bar{1} \bar{1}]$ beam directions (TEM specimen prepared from Figure 66(a) from sample 56-345-280, HIP'ed at $560 \text{ }^\circ\text{C}$ for 345 minutes with $280 \text{ }^\circ\text{C}/\text{hour}$).

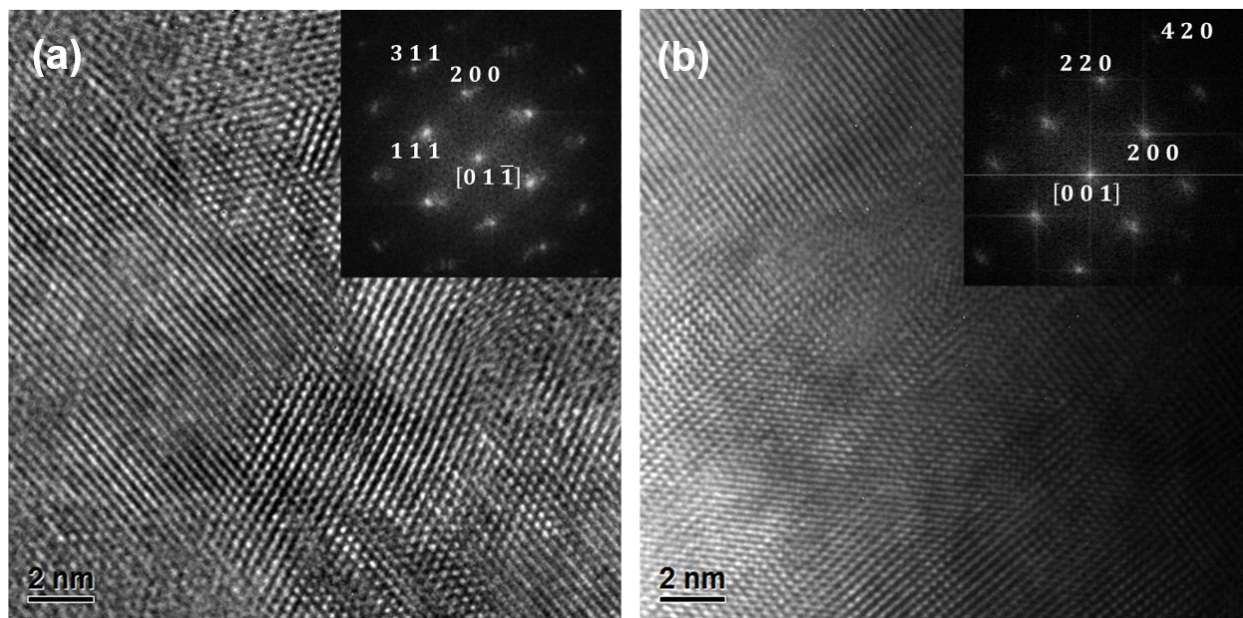


Figure 69. High resolution TEM micrographs with the fast Fourier transform analysis along the $[0\ 1\ \bar{1}]$ and $[0\ 0\ 1]$ beam directions for the UO_2 phase (TEM specimen prepared from Figure 66(a) from sample 56-345-280, HIP'ed at $560\ ^\circ\text{C}$ for 345 minutes with $280\ ^\circ\text{C}/\text{hour}$).

Table 15. Crystallographic details, properties, and chemical compositions for the UC, UO₂ and γ (U10Mo) phases [52, 60, 71, 81, 106, 108-113]. The chemical compositions reported are typical values observed in this study by semi-quantitative standard-less XEDS.

Phase	UC	UO ₂	γ (U10Mo)	
Pearson Symbol	cF8	cF12	cI2	
Space group	Fm-3m (225)	Fm-3m (225)	Fm-3m (225)	
Lattice parameter (Å)	4.955	5.467	3.409	
Elastic modulus (kg/cm ²)*	2.2×10^6	1.76×10^6	9.1×10^5	
Thermal expansion coefficient (/K)	$\sim 10^{-5}$	$\sim 10^{-5}$	$\sim 10^{-5}$	
Melting point (°C)	2275	2878	~ 1250	
Density (g/cm ³)*	13.63	10.27	17.2	
Hardness (kg/mm ²)*	923	666	316	
Composition (at.%)	U	30.2	33.1	78.4
	Mo	2.3	2.1	21.6
	Zr	0.4	1.0	N.A.
	O	0.0	10.2	N.A.
	C	67.1	53.6	N.A.

* At room temperature

Figure 70 shows a HAADF micrograph from the TEM sample that had limited interdiffusion and reaction between the U10Mo and Zr diffusion barrier without the apparent presence of the inclusions. Although not observed by SEM, a significant amount of UC and UO₂ phases was identified on the U10Mo fuel next to Zr barrier as “varying” contrasts (i.e., composition and orientation sensitive) in Figure 70. Figure 71(a) shows the presence of UC and UO₂ phases near the surface of U10Mo in contact with Zr barrier by BF TEM micrograph. Both UC and UO₂ phases were confirmed by FFT analyses as presented in Figure 71(b) and (c). Figure 72 shows the XEDS elemental mapping from the region shown in Figure 70. Presence of UC and UO₂ phases near the Zr within the γ -phase U10Mo alloy is distinguished by Mo depletion, while distinction between the UC and UO₂ is apparent by contrast in U content: higher in UC than UO₂.

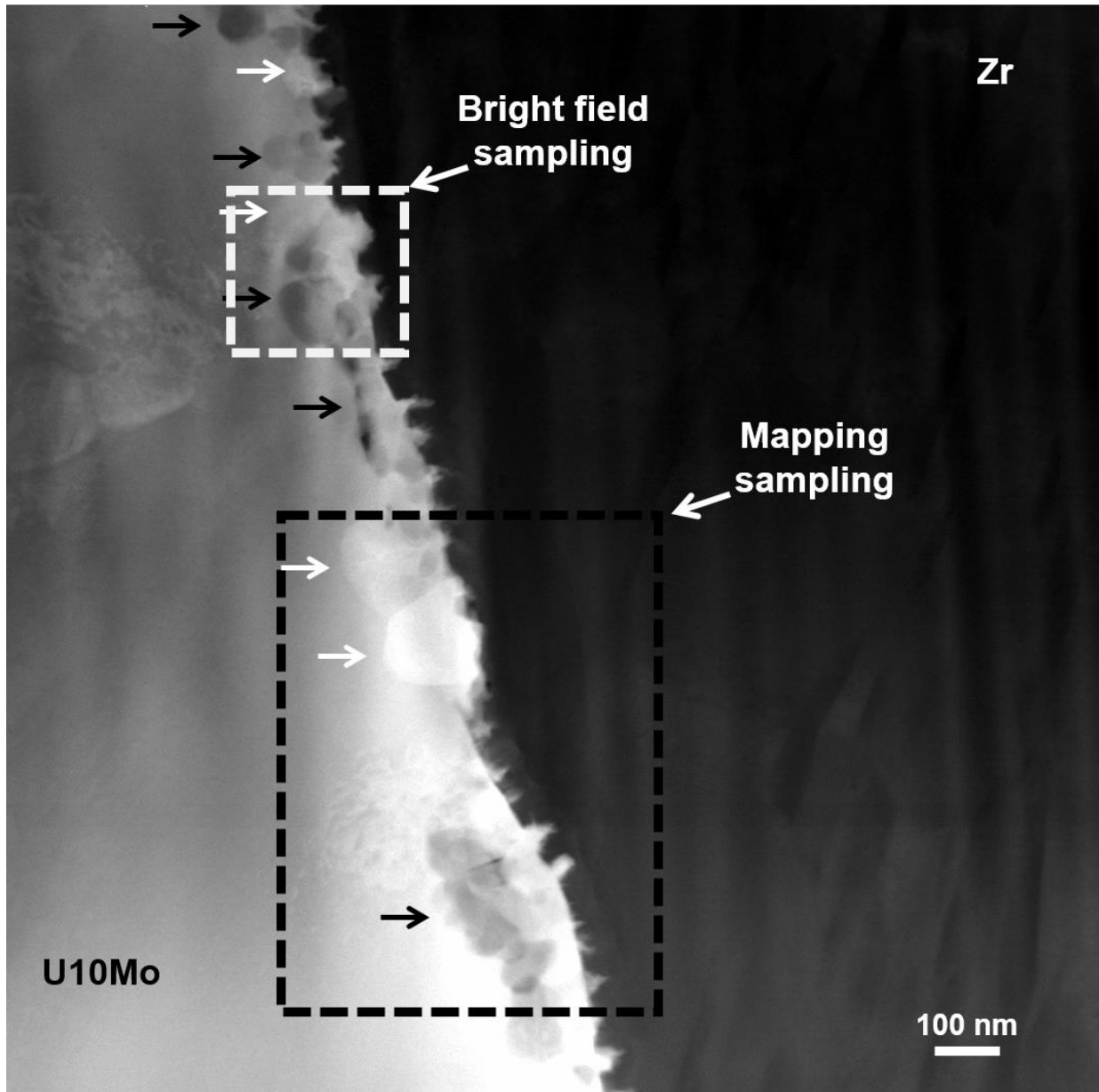


Figure 70. HAADF STEM micrograph of the region with limited interdiffusion and reaction near the interface between the U10Mo alloy and Zr diffusion barrier. Contrast developed by composition and orientation shows UC (white arrows) and UO_2 (black arrows) phases (TEM specimen prepared from Figure 66(b) from sample 56-345-280, HIP'ed at 560 °C for 345 minutes with 280 °C/hour).

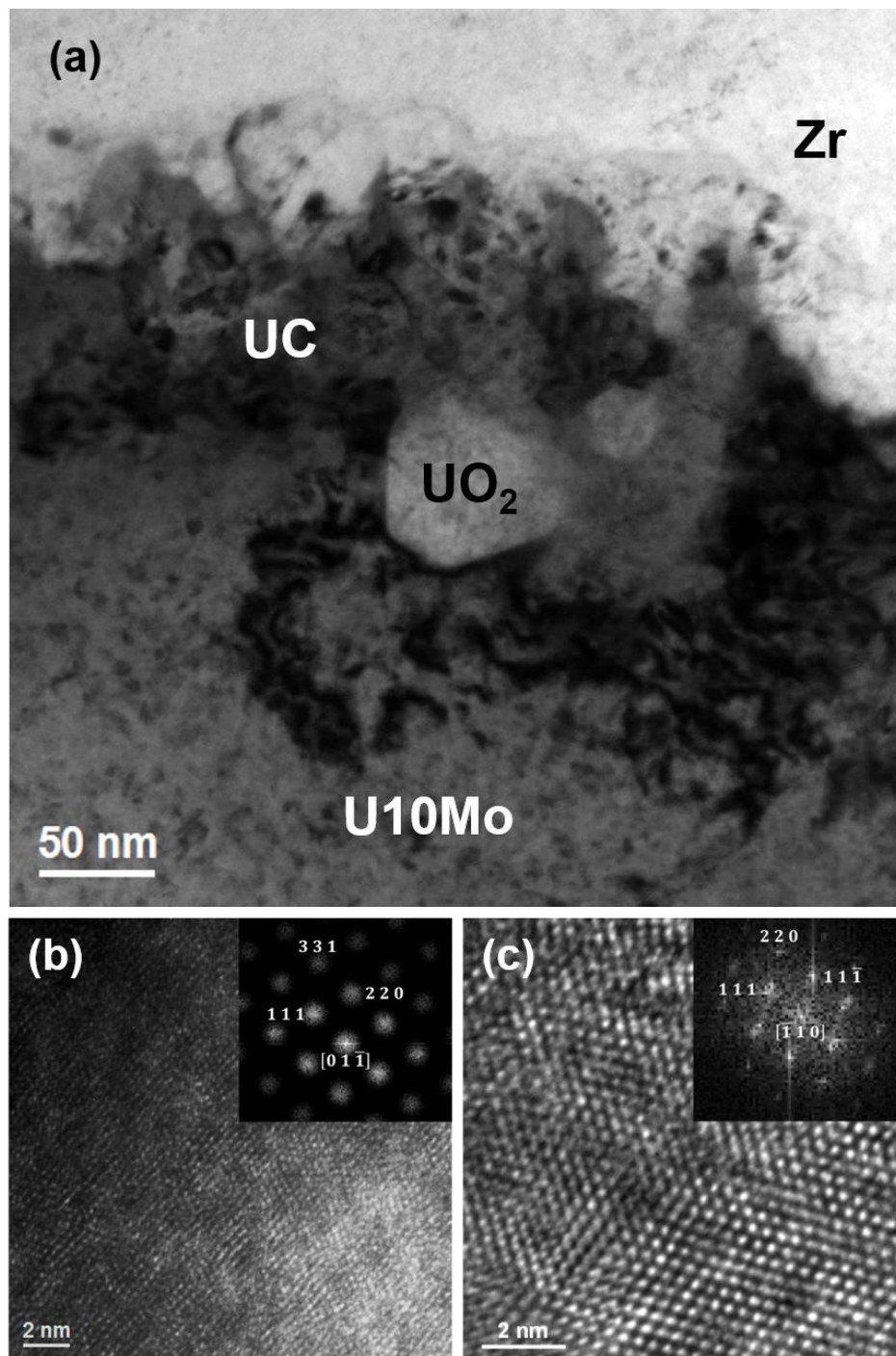


Figure 71. (a) Bright field micrograph and high resolution TEM micrographs with the fast Fourier transform analyses for the (b) UC and (c) UO₂ phases (TEM specimen prepared from Figure 66(b) from sample 56-345-280, HIP'ed at 560 °C for 345 minutes with 280 °C/hour).

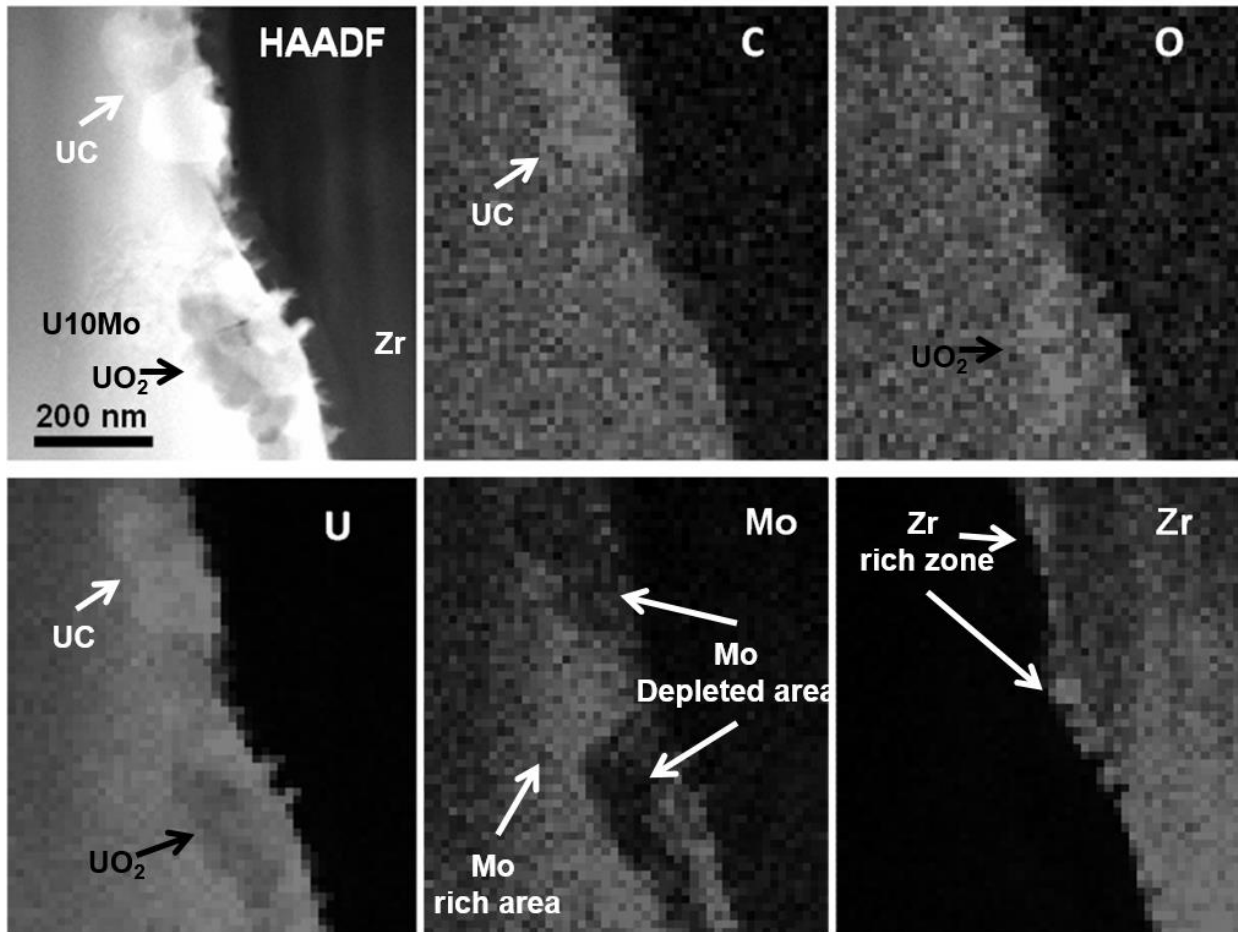


Figure 72. XEDS elemental mapping of Figure 70 (TEM specimen prepared from Figure 66(b) from sample 56-345-280, HIP'ed at 560 °C for 345 minutes with 280 °C/hour).

7.3.5. Image analyses for the anomalous features

The UC and UO₂ phases in the U10Mo alloy matrix were observed in all fuel plate samples listed in Table 16. Figure 73 shows a BSE micrograph with highlights that distinguishes the UC and UO₂ phases. Although the morphology of the UC and UO₂ phases is clearly influenced by the co-rolling, it is assumed that the area percent by image analysis approximates the volume percent

for these phases with limited plasticity. Area percent of the UC and UO₂ estimated for all samples examined in this study is listed in Table 16. The amount of these inclusions did not change during HIP: as a function of time at 560 °C as presented in Figure 74(a); and as a function of temperature after 90 minutes as presented in Figure 74(b). Therefore, the UC and UO₂ phases are presumed to come from the initial casting process, and their amount is not altered by HIP.

Table 16. HIP plate samples examined in this study along with estimated quantity of microstructural anomalies.

Sample	Area percent of the UC and UO ₂ phases in U10Mo (%)	Limited interdiffusion-reaction zone (%)
AR	1.24	18.10 ± 0.54
52-90-280	1.53	19.90 ± 0.49
54-90-280	0.49	16.65 ± 0.20
56-45-280	1.78	14.99 ± 0.39
56-60-280	1.18	20.47 ± 0.47
56-90-280	1.39	11.05 ± 0.16
56-180-280	1.41	21.71 ± 0.51
56-345-280	1.64	10.90 ± 0.38
58-90-280	1.32	9.75 ± 0.15

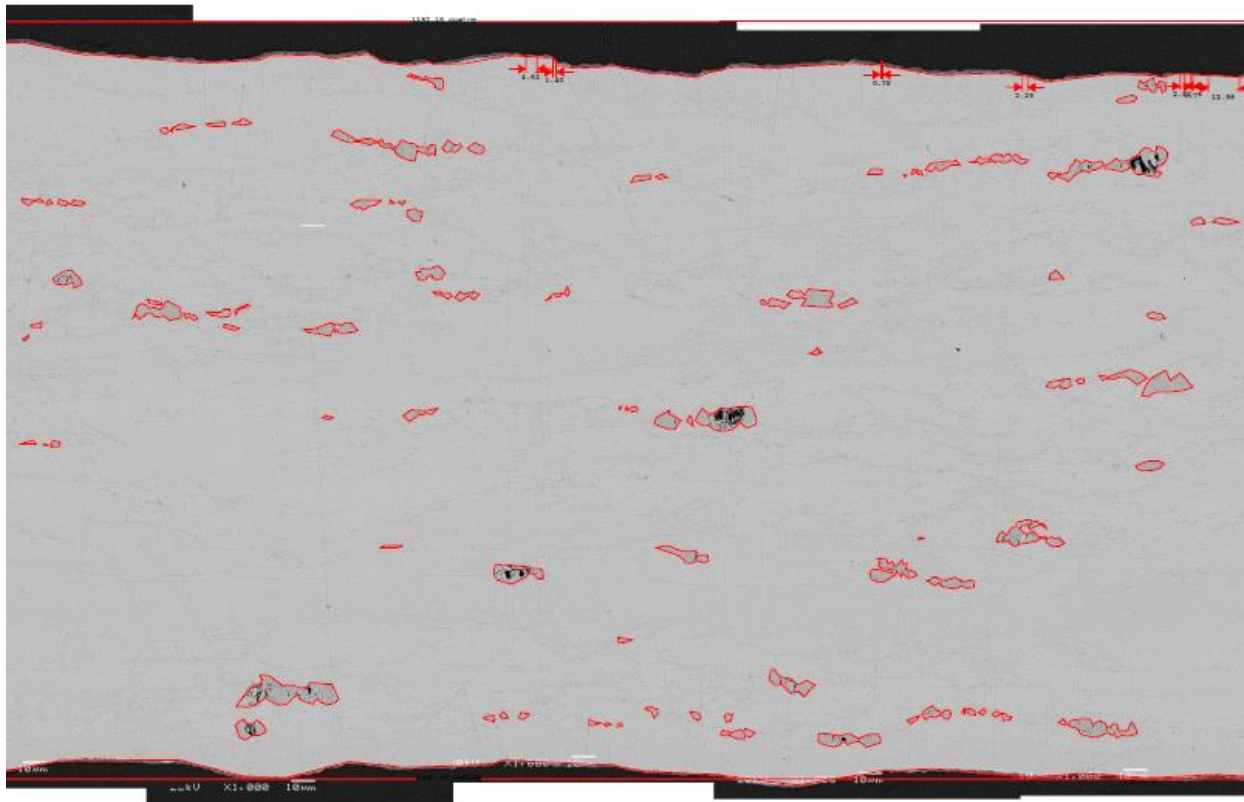


Figure 73. The measurement of area percent for the UC and UO₂ phases distributed in the U10Mo alloy.

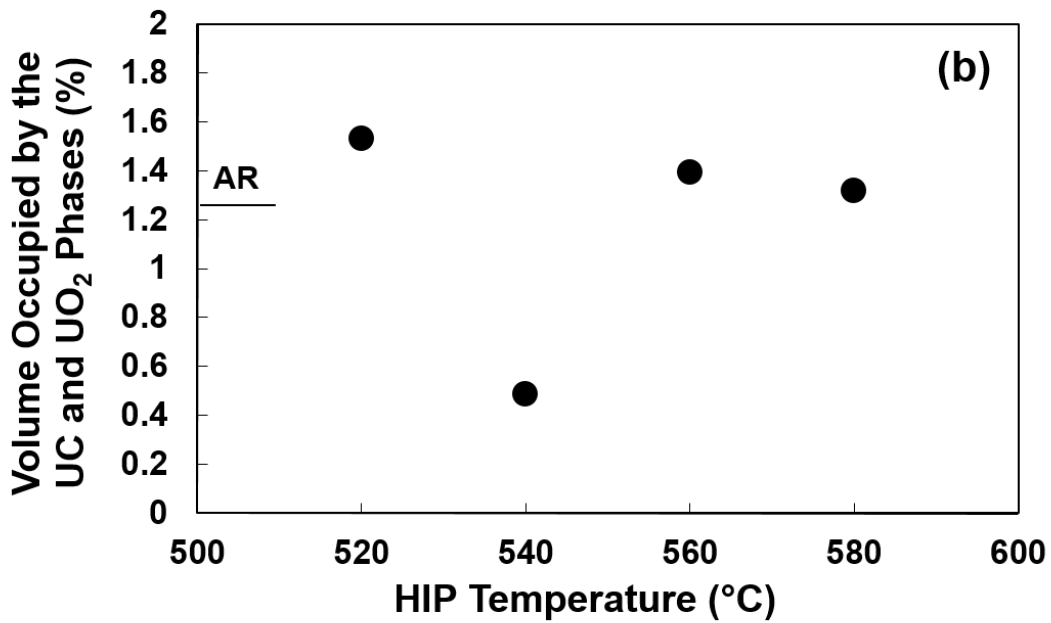
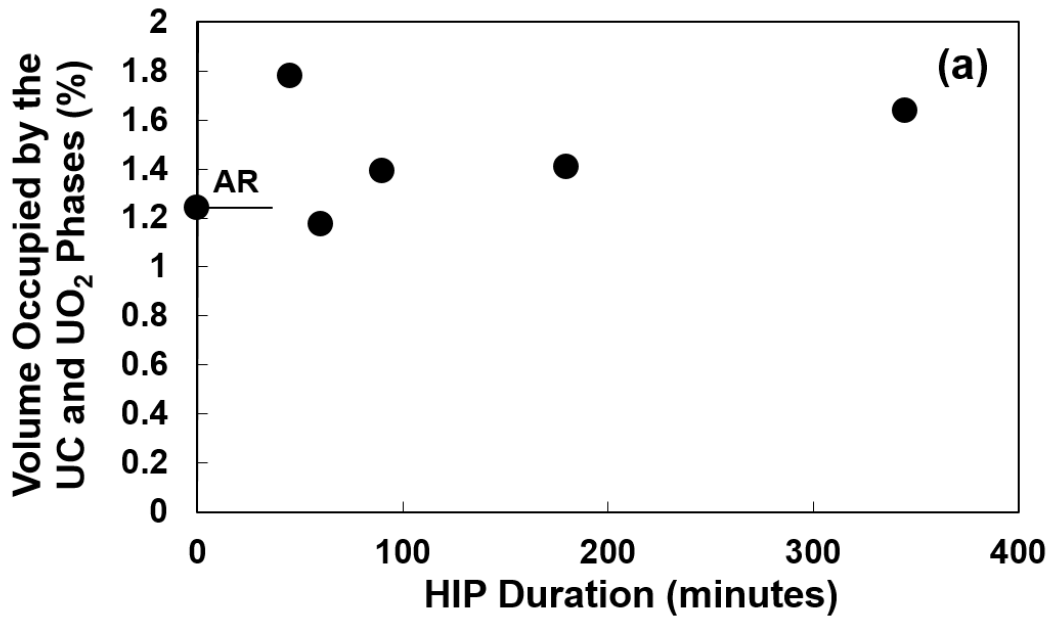


Figure 74. Estimate volume fraction of the UC and UO₂ inclusion phases distributed in the U10Mo monolithic fuel after HIP'ing (a) at 560 °C as a function of time, and (b) after 90 minutes as a function of time. “AR” refers to the estimated volume fraction in as-rolled sample prior to HIP process.

In all samples examined in this study, regions of limited interdiffusion and reaction were observed as presented in Figure 66(b). They were observed typically with the presence of UC and UO₂ phases as presented in Figure 70, Figure 71 and Figure 72. The linear length of these regions and the total length of the fuel alloy in contact with Zr barrier were measured to estimate the linear percent of regions where the interdiffusion and reaction were significantly impeded. Figure 75 shows an example to illustrate how the fractional linear length of the limited interdiffusion–reaction zone was measured (i.e., L_i/L_T) over the entire fuel plate sample. Table 16 reports the percent of length associated with limited interdiffusion and reaction. Standard deviation in percent measurement was obtained by three independent measurements.

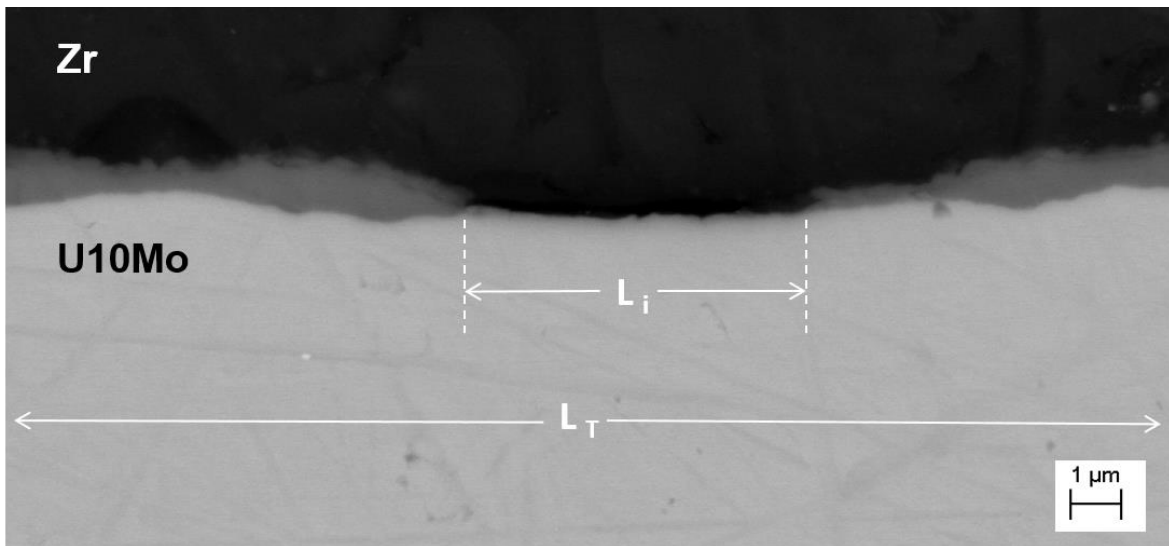


Figure 75. Illustration of the linear measurement for regions with limited interdiffusion and reaction between the U10Mo alloy and Zr diffusion barrier.

Figure 76(a) presents the amount of region with limited interdiffusion and reaction as a function of HIP temperature with a constant holding time of 90 min. Despite the interference of the UC and UO₂ phases on the interdiffusion and reaction, there is a noticeable decrease in this microstructural anomaly as a function of temperature. However, as a function of HIP time at 560 °C, no observable trend was observed as shown in Figure 76(b). A decrease in the amount of regions with limited interdiffusion and reaction may involve complex phenomena including oxide/carbide break-up, thermally-activated interdiffusion via lattice and interfaces with geometrical barriers, nucleation and growth. Within the parameters of temperature and time variation in this study, only the temperature dependence was observed.

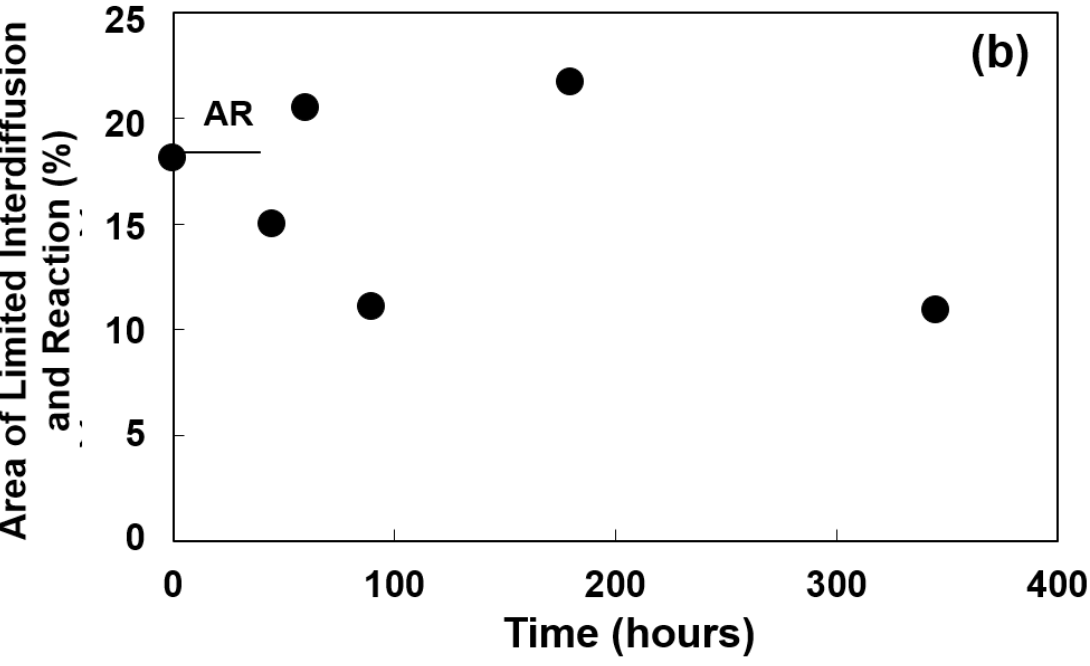
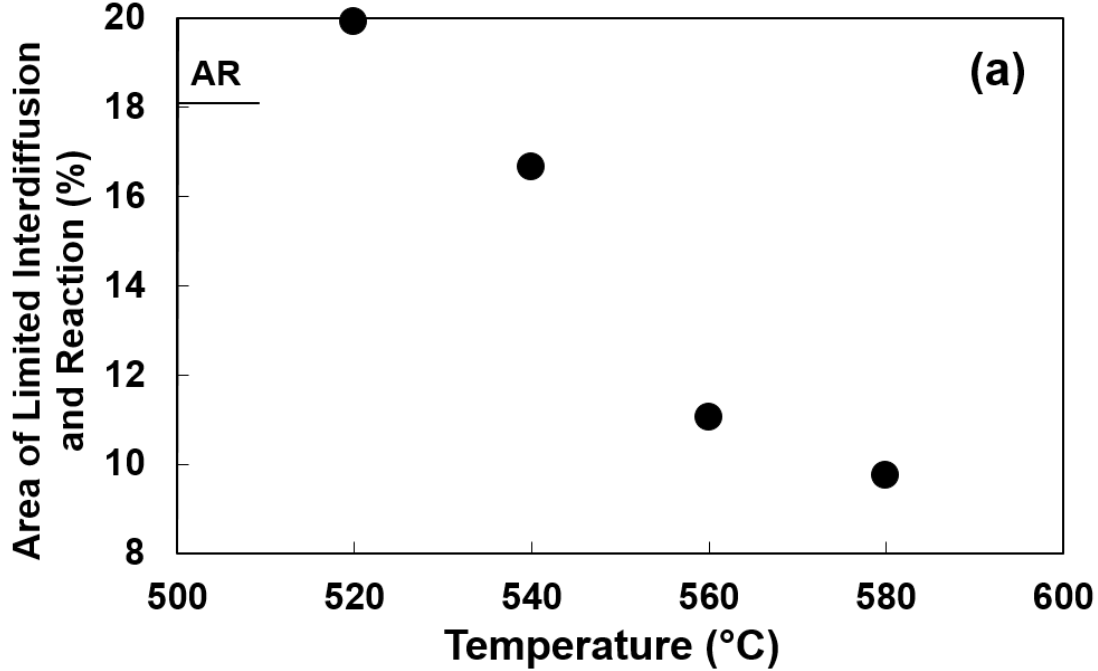


Figure 76. Estimated area of limited interdiffusion and reaction between the U10Mo and Zr diffusion barrier during HIP'ing as (a) a function of temperature after 90 minutes and (b) a function of time at 560 °C. "AR" refers to the estimated volume fraction in as-rolled sample prior to HIP process.

7.4. Discussion

The main purpose of thin Zr foil placed between the U10Mo alloy and AA6061 cladding is to minimize the diffusional interaction between the fuel and cladding alloy, because the interdiffusion between U10Mo alloy and AA6061 can nucleate and grow phases that can adversely affect the fuel performance during irradiation [30, 31, 34-37, 39]. Zr has been reported [43] as an excellent diffusion barrier based on its physical properties and solid-to-solid diffusion couples investigations.

7.4.1. The U10Mo/Zr interface

At the interface between the U10Mo and Zr, the α U, Mo_2Zr , and UZr_2 phases were observed; however, the growth of the interaction layer containing these phases during HIP'ing was negligible for the ranges of time and temperature examined in this study. The α U (Orthorhombic) can form by the decomposition of $\gamma\text{U}(\text{Mo})$. The α U with its anisotropic crystal structure can exhibit anisotropic growth and relatively high swelling rate during irradiation [101]. The continuous layer of the UZr_2 phase can develop by the reaction of Mo-depleted α U and αZr . The intermetallic phase, Mo_2Zr , would be form by Mo rejected from the decomposition of $\gamma\text{U}(\text{Mo})$ and Zr from the UZr_2 layer. Therefore, the development of Mo_2Zr phase corresponds to the depletion of Mo from $\gamma\text{U}(\text{Mo})$ which would promote the formation of α U phase upon cooling. Potentially, the excessive growth of these diffusional interaction products during fuel fabrication can adversely influence the fuel performance. However, this investigation clearly indicates that the formation and growth of the

layer occurs primarily during the co-rolling process, and the growth of the interaction layer is insignificant during HIP'ing at pressure of 100 MPa for the temperature and time range examined in this investigation.

7.4.2. The AA6061/Zr interface

At the interface between the Zr diffusion barrier and AA6061, only the $(Al,Si)_3Zr$ phase was found to grow. Although AA6061 contains only 0.4~0.8 wt.% Si, a significant amount of Si (up to 10 wt.%) was observed in the $(Al,Si)_3Zr$ phase. This indicates that the Si is moving fast due to thermodynamic driving force (i.e., formation of silicides) and/or kinetics (intrinsic diffusion coefficients of Si in Al). Formation and growth of $(Al,Si)_3Zr$ warrants a further study, particularly at lower temperature [114, 115] and with the influence of irradiation. Dickson *et al.* [115] identified phase constituents, thick Al_3Zr and thin Al_2Zr , at the Al-Zr interface and determined the activation energy of 347 kJ/mol based on the parabolic growth constants.

7.4.3. U10Mo matrix

Figure 77 outlines the decomposition mechanism of the cellular and lamellar structures. The initial phase transformation of γ into α and γ' is described in Figure 77(a). The initial shape of precipitates, which depends on total interfacial energy, results in the nucleation of cellular structure at heterogeneous sites, such as grain boundaries. The microstructures are characterized by Mo

depleted regions within the grains, surrounding the γ' nuclei. The Mo-depletion from γ results in thermodynamic instability, which subsequently increases the driving force for the transformation into α with Mo-solubility of $C_{\alpha 1} - C_{\alpha 0}$ and intermetallic γ' . The isolated γ' precipitates tend to form discontinuous layers along the grain boundaries, likely due to simultaneous bulk and grain boundary diffusion as shown in Figure 54, Figure 60 and Figure 63. Subsequent Mo-depletion causes the growth of γ' as described in Figure 77(b). As the depleted regions grow and begin to merge, the cellular structures begin to develop into lamellar structures of α and γ' , growing from the grain boundaries and into the grains. The growth of lamellar structures continues into the bulk during the period of Figure 77(c). Figure 77(d) describes the lamellar structure with equilibrium status after prolonged HIP holding time.

Repas *et al.* [63] presented the TTT diagram of U10Mo alloys in the temperature range of 300 and 580 °C to describe microstructure and constituent phases. However, in some cases, the TTT diagram shows a two phase region while this study revealed three phase lamellar or cellular decomposition regions under the same conditions. Table 17 summarizes observed phases under the given heat treatments for this study and other studies in order to compare with the TTT diagram. The previous investigations by Lopes *et al.* [116] and Kim *et al.* [117] reported early formation of γ' at 500 °C after 24 and 6 hour heat treatment, respectively. In addition, Repas *et al.* reported the phase transformations of $\alpha + \gamma'$ into $\alpha + \gamma$ at 573 °C (lower critical temperature), and $\alpha + \gamma'$ into γ at 580 °C (upper critical temperature) in the TTT diagram. However, these temperatures have been subject to some scrutiny through later investigation [4, 12, 52, 67, 74, 78, 118]. Table 18 summarizes the critical transition temperatures in U10Mo. The lower and upper critical

temperatures were reported from the other literatures as 555 ~ 560 °C and 570 ~ 580 °C, respectively. These temperatures were supported by the analysis of temperature effects with constant holding time and RC rate as shown in Figure 60, Figure 61 and Figure 62. The samples heated to 520 and 540 °C show the lamellar reaction of α and γ' within the γ matrix while little significant lamellar structure was observed in samples heated above 560 °C. This demonstrates the inversed phase transformations of α and γ' into α and γ , or α and γ into γ at 560 and 580 °C, respectively. Additional isothermal aging analysis is required to effectively demonstrate the microstructural transformations between 560 and 580 °C. Additionally, aging effects were investigated at 560 °C with RC rates of 280 °C/h in Figure 63, Figure 64 and Figure 65. The volume fraction of γ' hardly increased as HIP holding time increased because γ' was transformed into α and γ above the eutectoid temperature. Therefore, in order to retain the γ phase and to minimize phase transformation of γ into α and γ' in the U10Mo fuel, HIP heat treatments utilizing at least 560 °C and the highest RC rate are essential.

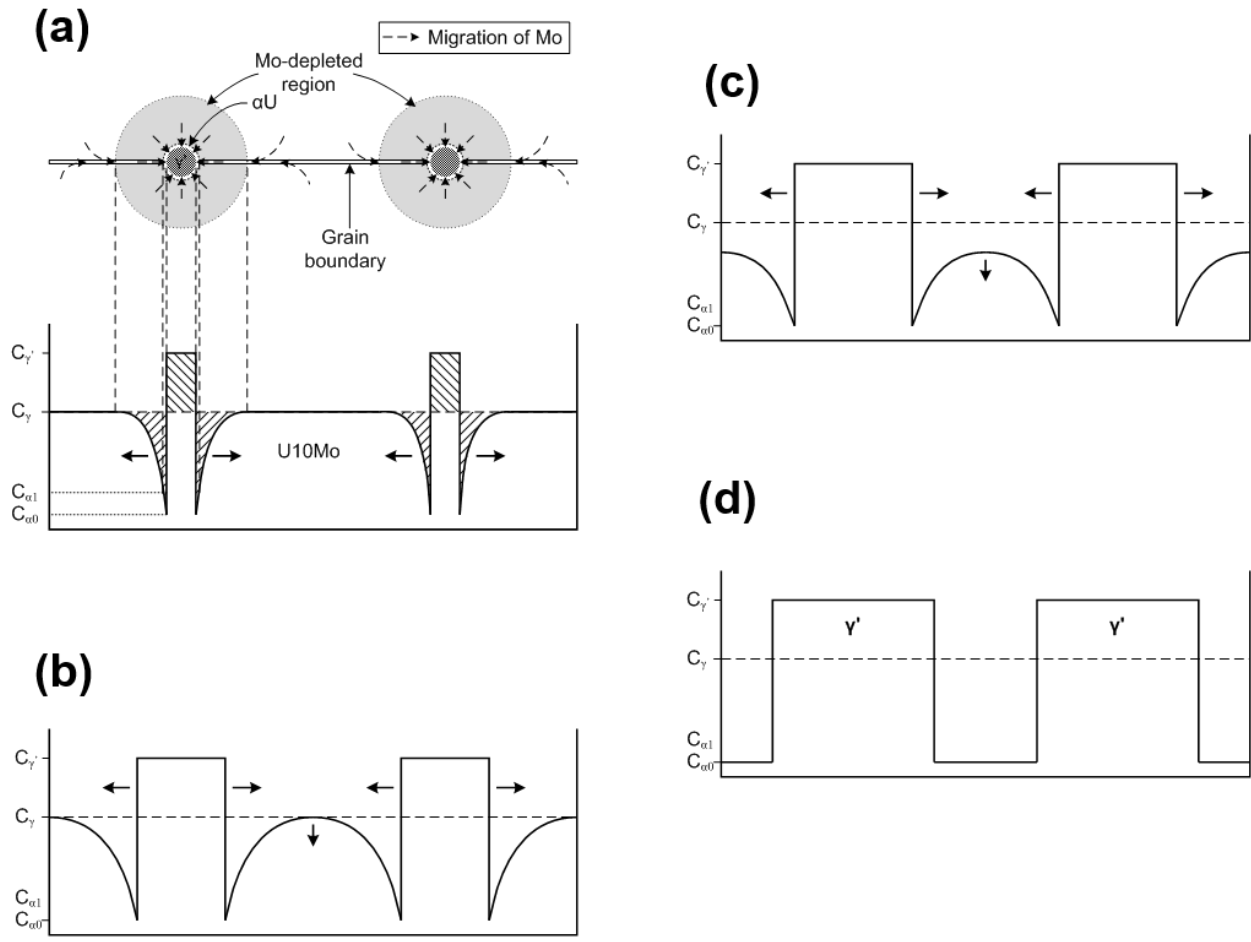


Figure 77. Schematic diagram for nucleation of cellular structure and development of lamellar structure.

Table 17. The observed phases for each heat treatment in previous researches and the indicated in TTT diagram.

	Heat treatment	In the literatures	In the TTT diagram [63]
In this study	520C for 25-26.5 hours	γ, α, γ'	γ, α
	540C for 25-26.5 hours	γ, α, γ'	γ, α
Lopes [116]	500C for 6 hours	γ, α, γ'	γ, α
Kim [117]	400C for 350 hours	γ, α, γ'	γ, α, γ'
	500C for 24 hours	γ, α, γ'	γ, α
	500C for 100 hours	γ, α, γ'	γ, α, γ'
	500C for 500 hours	α, γ'	α, γ'
Lotts [12]	450C for 336 hours	α, γ'	α, γ'

Table 18. The critical temperatures of U10Mo alloy for the phase transformations.

	$\alpha + \gamma' \rightarrow \alpha + \gamma$ at the lower critical temperature	$\alpha + \gamma \rightarrow \gamma$ at the upper critical temperature
Repas [63]	573	580
Kim [76]	N/R	> 570
Okamoto [52]	555	~ 580

7.4.4. UC and UO₂ inclusions at the U10Mo/Zr interface and U10Mo matrix

The UC and UO₂ phases in the U10Mo alloy appear to originate from the C and O impurities during the casting based on this investigation [72, 105]. Amount of these inclusions did not change during HIP'ing within the U10Mo alloy. Their presence near the surface of the U10Mo alloy in contact with Zr diffusion barrier impeded the interdiffusion and reaction that produce UZr₂ layer, discrete Mo₂Zr and α U layer after HIP. However, the region of limited interdiffusion and reaction disappeared noticeably with an increase in HIP temperature, however not with longer HIP duration examined in this study.

Distribution of UC and UO₂ inclusions in the U10Mo fuel alloy can cause unexpected physical, mechanical and chemical behavior of the monolithic fuel plate [72, 105-107]. This manuscript reported some anomalies in chemical interactions between the fuel alloy and Zr diffusion barrier. Table 16, in addition to crystallographic details and compositions, lists some of the physical and mechanical properties for the UC, UO₂ and γ (U10Mo) phases [52, 71, 72, 105-108, 110-113]. During the fabrication of the monolithic fuel plate, large differences in elastic modulus and hardness may cause crack formation within the low-toughness phase. Cracks were frequently observed in the UO₂ phase as presented in Figure 66 and Figure 67 in this study.

7.4.5. U10Mo-Zr system vs. U10Mo/Zr interface in HIP fuel plates

The following similarities of U10Mo-Zr system and U10Mo/Zr interface in HIP fuel plates were exhibited:

1. Formation of $(\text{Mo,U})_2\text{Zr}$ phase (Mo_2Zr phase in U10Mo-Zr system due to negligible U composition) promoted destabilization of U10Mo into U rich phase (αU or βU).
2. The increasing concentration of U with decreasing Mo composition demonstrates Zr effectiveness as the diffusion barrier to retain the U-density stability within the metallic fuel.
3. U diffused into Zr side faster and thus U-Zr solid solution, βZr phase in U10Mo-Zr system and $(\text{U,Mo})\text{Zr}_2$ phase in HIP fuel plates, was formed in Zr side.

The differences between U10Mo-Zr system and U10Mo/Zr interface in HIP fuel plate are listed in Table 19.

Table 19. Comparison the U10Mo-Zr system and the U10Mo/Zr interface in HIP fuel plate.

Diffusion couples	HIP fuel plates
<p>Phenomenon: The incubation time (159 hours) was considered before nucleation and growth for interdiffusion and reaction zone. Reason: No pressure was applied.</p>	<p>Phenomenon: The interdiffusion and reaction zone grew faster despite shorter annealing time (75 minutes). Reason: High pressure to overcome experimental environment during the fabrication was applied during co-rolling.</p>
<p>Phenomenon: About 95 wt.% βU phase was observed at the U10Mo/Zr interface. Reason: During water-quenching after annealing 650 °C, γU was transformed into βU. However, there was no allotropic transformation of βU into γU because of 5 wt.% Mo composition.</p>	<p>Phenomenon: Above 99 wt.% αU phase was observed at the U10Mo/Zr interface. Reason: Although U10Mo/Zr coupon was annealed at 650 °C during the co-rolling process, the sample was HIP'ed below eutectoid temperature (520~580 °C) and slow-cooled under room temperature.</p>
<p>Phenomenon: βZr (BCC) was observed for the solid solution phase. Reason: The couples were annealed above 615 °C to separate βZr and δ.</p>	<p>Phenomenon: δ (HCP) was observed for the solid solution Reason: HIP were carried out below 615 °C (520 ~ 580 °C)</p>
<p>Phenomenon: αZr precipitates within U10Mo were observed. Reason: The diffusion couples were sufficiently annealed for diffusion of Zr into U10Mo.</p>	<p>Phenomenon: αZr precipitates within U10Mo were not observed. Reason: HIP were insufficiently carried out for diffusion of Zr into U10Mo.</p>
<p>Phenomenon: Only γU10Mo was stabilized within U10Mo alloy. Reason: The phase transformation of γ into α and γ' did not occur according to the TTT diagram for the water-quenched couples.</p>	<p>Phenomenon: γU10Mo was destabilized into α and γ' phases within U10Mo alloy after HIP'ed below the eutectoid temperature. Reason: HIP process below the eutectoid temperature and slow-cooling caused decomposition of γ according to the TTT diagram</p>

CHAPTER 8: Summary

Development of phase constituents, microstructure and concentration profiles were investigated for U10Mo vs. Zr diffusion couples annealed as a function of time (240, 480 and 720 hours) at 650 °C. Thick and thin layers of β Zr and β U, respectively, were observed, while a discontinuous layer of Mo_2Zr was observed between β Zr and β U layers. Formation of the Mo_2Zr phase altered the local compositions and led to the formation of β U and α Zr (upon cooling) phases nearby. In addition, acicular α Zr and $\text{U}_6\text{Zr}_3\text{Mo}$ phases were observed within the γ U(Mo). These observations were similar for all couples including the one that was furnace cooled after anneal at 650 °C. In addition, these results were quite similar to a previous diffusion couple investigation at 700 °C. Despite the development of a complex microstructure, the concentration profiles projected as semi-quantitative diffusion paths on an isothermal ternary phase diagram agreed in general to the phase equilibrium at 650 °C. With an assumption of an incubation period, thickness for the zone of interdiffusion and reaction grew at a rate of $7.75 (\pm 5.84) \times 10^{-16} \text{ m}^2/\text{s}$ with an activation energy of 219 kJ/mol.

Microstructural and kinetics analyses were carried out for U vs. Zr diffusion couples annealed at 580 °C for various time (360, 480, 720 and 960 hours), at 650 °C for 480 hours, at 680 °C for 240 hours and at 710 °C for 96 hours. Primarily, the interdiffusion and reaction layers consisted of α U(oC4) with Zr acicular precipitate, α' (assumed as oC4) and (γ U, β Zr) (cI2) solid solution. From concentration profiles, the interdiffusion flux was estimated for each phase using the Boltzmann-Matano analysis. The integrated interdiffusion coefficient was determined using Sauer-Freise with Wagner analysis to avoid error due to $\partial C/\partial x = 0$. The integrated interdiffusion

coefficients as a function of temperature obeyed Arrhenius relationship, therefore, activation energies, 251.66, 107.58 and 152.23 kJ/mol, and pre-exponential factors, 1.11×10^{-3} , 4.84×10^{-12} and 1.07×10^{-7} m²/s, were calculated for α U with Zr precipitate, α' and (γ U, β Zr) above 615 °C, respectively. The intrinsic diffusion coefficients of U and Zr for (γ U, β Zr) phase at 650, 680 and 710 °C, and δ -UZr₂ at 580 °C were calculated at the marker plane from Heumann analysis, and the pre-exponential factor and activation energy of intrinsic diffusion coefficient for each element in (γ U, β Zr) phase were determined as $D_{0,Zr} = 5.10 \times 10^{-13}$ m²/s, $Q_{Zr} = 51.38$ kJ/mol, $D_{0,U} = 9.14 \times 10^{-13}$ m²/s and $Q_U = 48.81$ kJ/mol. At the marker plane, the interdiffusion coefficients calculated from the Darken equation corresponded closely with the result from the Boltzmann-Matano method. The activation energies and pre-exponential factors for α U with α Zr, α' and (γ U, β Zr) were estimated for the parabolic growth constant as 209.35, 229.97 and 199.45 kJ/mol, and 1.66×10^{-4} , 4.58×10^{-6} and 3.43×10^{-4} m²/s, respectively.

Interdiffusion and reaction between the U10Mo fuel alloy and Zr diffusion barrier, as well as Zr and AA6061 cladding alloy were examined by using SEM and TEM for U-Mo monolithic fuel. Specifically, the samples after co-rolling and HIP'ing (i.e., functions of temperature and time) were examined to identify the phase constituents and quantify the growth kinetics. The co-rolling process utilizes soaking at a temperature of 650 °C for an approximate total time of 130 minutes. The HIP was carried at various temperatures (520, 540, 560 and 580 °C) and time duration up to 345 minutes with ramp-cooling rates (35, 70 and 280 °C/hour) at a constant pressure of 103 MPa. The UZr₂, α U and Mo₂Zr phases were observed to develop at the U10Mo/Zr interface, however essentially only during co-rolling (650 °C for 130 minutes), and they exhibited a remarkable

stability during HIP'ing up to 345 minutes. The $(\text{Al,Si})_3\text{Zr}$ phase was observed to grow at the Zr/AA6061 interface during HIP'ing with an activation energy of 457.54 ± 27.60 kJ/mol. Given the negligible growth of interaction products at the U10Mo/Zr interface and slow growth of $(\text{Al,Si})_3\text{Zr}$, HIP provides a robust process with flexibility for process control to fabricate monolithic U10Mo fuel with a co-rolled Zr diffusion barrier, clad in AA6061.

U10Mo alloy for monolithic fuel plates encased in AA6061 cladding was characterized. The constituent phases of U10Mo alloy consisted of γ , α , and γ' , and were identified as $\text{cI}2 \text{ Im}3\text{m}$ ($3.474 \times 3.474 \times 3.474 \text{ \AA}$), $\text{oC}4 \text{ Cmcm}$ ($2.854 \times 5.869 \times 4.955 \text{ \AA}$) and $\text{tI}6 \text{ I}4/\text{mmm}$ ($3.427 \times 3.427 \times 9.834 \text{ \AA}$) by TEM SAED. The phases were formed from decomposition of γ into α and γ' because HIP processing was conducted near the eutectoid temperature with varying fabrication parameters including RC rate, temperature, and holding time. Initial cellular structures of α and γ' from decomposition of γ nucleated discontinuously on grain boundaries, and evolved to lamellar structures of alternating α and γ' . The growth of lamellar structures became more pronounced with the following:

- Decreasing RC rate
- Decreasing temperature in the range of $520 \sim 580 \text{ }^\circ\text{C}$
- Decreasing holding time at $560 \text{ }^\circ\text{C}$

Mo depletion caused the formation of 1~2 wt.% Mo α while around 17 wt.% Mo γ' was observed, maintaining a balance of total Mo composition. In order to ensure the best performance and stability of fuel during irradiation, retention of γ is essential. Therefore, the fabrication process must be optimized to reduce decomposition of γ without detrimental effects to the integrity of the

monolithic fuel plate. Furthermore, improved TTT diagrams can yield thermo-kinetic information critical to optimization of HIP process parameters.

The microstructural anomalies in the U10Mo fuel alloy and near the interface between the U10Mo fuel alloy and Zr diffusion barrier were examined by SEM and TEM/STEM. The cF8, Fm-3m (225) UC phase and cF12, Fm-3m (225) UO₂ phase were identified to be distributed throughout the U10Mo alloy. Volume percent of these inclusions ranged from 0.5 to 1.8, and did not change as functions of HIP temperature and time. The presence of UC and UO₂ inclusions near the surface of the U10Mo alloy in contact with Zr diffusion barrier produced regions of limited interdiffusion and reaction observed by cross-sectional microscopy. HIP at higher temperature partially removed these regions of impeded interdiffusion and reaction. However, within the HIP duration examined in this study at constant temperature of 560 °C, no noticeable change was observed as a function of time. Difference in physical, mechanical and chemical properties/interactions of UC, UO₂, and γ U10Mo phases can influence structural integrity of the U10Mo monolithic fuel with Zr diffusion barrier.

In previous studies of interdiffusion and reaction in monolithic fuel plates after co-rolling and HIP'ing, HIP did not cause growth of the interaction layer at the U10Mo/Zr interface within the temperatures and holding time range examined. The development of the reaction zone at the U10Mo/Zr interface primarily occurred during the co-rolling process before HIP'ing. However, the intermetallic (Al,Si)₃Zr at the AA6061/Zr interface was shown to grow as HIP holding time increased and the growth followed the Arrhenius relation with an activation energy of 457.54 ± 27.60 kJ/mol. The regions of impeded interdiffusion and reaction were partially decreased as the

HIP temperature increased at U10Mo/Zr interface regardless of HIP holding time. From this it can be deduced that the optimal HIP process to ensure the highest quality of adhesion at the U10Mo/Zr and AA6061/Zr interfaces without excessive growth of $(Al,Si)_3Zr$ layer at the AA6061/Zr. In addition, the minimized decomposition of γ phase was figured out after HIP'ed at 580 °C with the ramp-cool rate of 280 °C/hour regardless of duration.

APPENDIX A: MATHEMATICAL THEOREM FOR RECIPROCAL LATTICE

In order to complete the crystallographic identification, the comparisons of theoretical results with experimental results were used in this research. The theoretical results were derived from calculating the spacing and angle of the reciprocal lattice. Otherwise, the experimental results were derived from measurement of the spacing and angle of the reciprocal lattice in the electron diffraction patterns. Figure 78 shows computational mechanism, which was used in this research for identification of these phases.

The original interplanar spacing (d_{hkl}) can be expressed by the reciprocal lattice vectors, \mathbf{a}^* , \mathbf{b}^* and \mathbf{c}^* :

$$d_{hkl} = \frac{1}{|\mathbf{h}\mathbf{a}^* + \mathbf{k}\mathbf{b}^* + \mathbf{l}\mathbf{c}^*|} \quad (\text{A.1})$$

$$\begin{aligned} & |\mathbf{h}\mathbf{a}^* + \mathbf{k}\mathbf{b}^* + \mathbf{l}\mathbf{c}^*|^2 \\ &= (h^2\mathbf{a}^{*2} + k^2\mathbf{b}^{*2} + l^2\mathbf{c}^{*2} + 2klb^*c^*\cos\alpha^* + 2lhc^*a^*\cos\beta^* \\ &+ 2hka^*b^*\cos\gamma^*) \end{aligned} \quad (\text{A.2})$$

The original interplanar angle is:

$$\begin{aligned} \cos \varphi = d_{hkl} d_{h'k'l'} [hh' a^{*2} + kk' b^{*2} + ll' c^{*2} + (kl' + lk') b^* c^* \cos \alpha^* \\ + (hl' + lh') a^* c^* \cos \beta^* + (hk' + kh') a^* b^* \cos \gamma^*] \end{aligned} \quad (\text{A.3})$$

Orthorhombic:

Orthorhombic interplanar spacing square is derived from (A.1) and (A.2):

$$d_{hkl}^2 = \frac{1}{h^2 a^{*2} + k^2 b^{*2} + l^2 c^{*2}} \quad (\text{A.4})$$

Orthorhombic interplanar angle is derived from (A.3):

$$\cos \varphi = d_{hkl} d_{h'k'l'} [hh' a^{*2} + kk' b^{*2} + ll' c^{*2}] \quad (\text{A.5})$$

where:

$$\alpha^* = \beta^* = \gamma^* = 90^\circ$$

$$a^* = \frac{1}{a}, \quad b^* = \frac{1}{b}, \quad c^* = \frac{1}{c}$$

Tetragonal:

Tetragonal interplanar spacing square is derived from (A.1) and (A.2):

$$d_{hkl}^2 = \frac{1}{(h^2 + k^2) a^{*2} + l^2 c^{*2}} \quad (\text{A.6})$$

Tetragonal interplanar angle is derived from (A3):

$$\cos \varphi = d_{hkl} d_{h'k'l'} [(hh' + kk') b^{*2} + ll' c^{*2}] \quad (\text{A.7})$$

where:

$$\alpha^* = \beta^* = \gamma^* = 90^\circ$$

$$a^* = b^*$$

$$a^* = \frac{1}{a}, \quad c^* = \frac{1}{c}$$

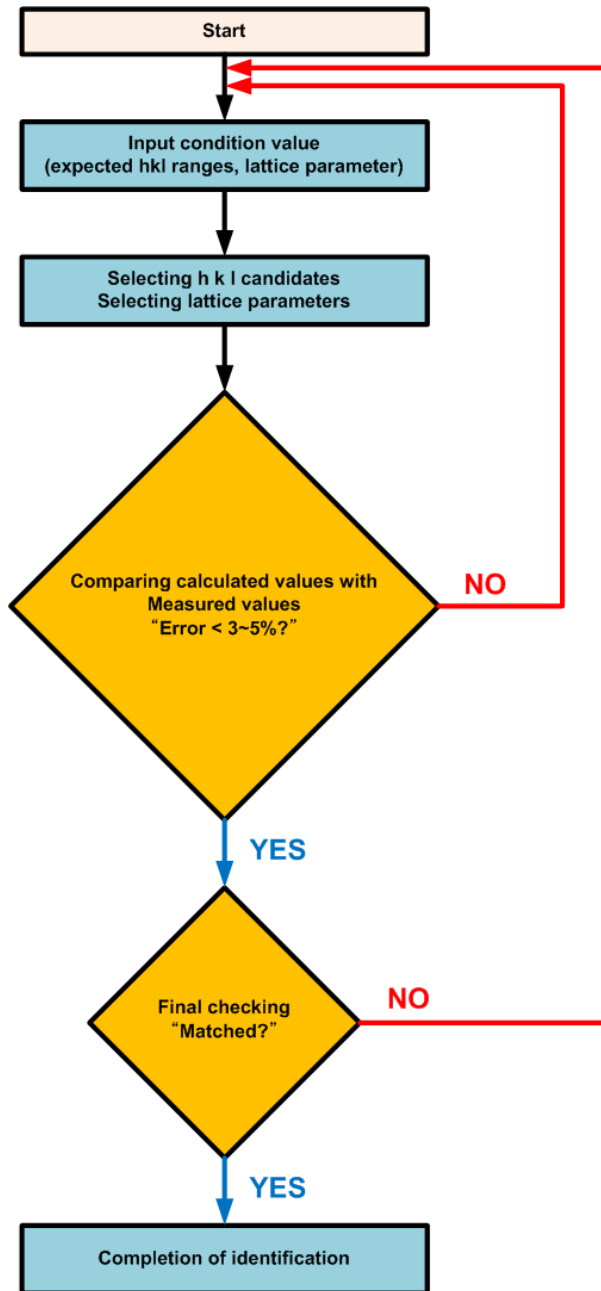


Figure 78. The procedure C++ coding for the identification of crystal structure and indexing

APPENDIX B: LIST OF PUBLICATIONS AND PRESENTATIONS

1. Journal Publications

1. K. Huang, **Y. Park**, A. Ewh, B.H. Sencer, J.R. Kennedy, K.R. Coffey, Y.H. Sohn. Interdiffusion and Reaction of Uranium and Iron. *Journal of Nuclear Materials* 424 (2012) 82–88.
2. K. Huang, **Y. Park**, D.D. Keiser Jr., Y.H. Sohn. Interdiffusion between Zr Diffusion Barrier and U-Mo Alloy. *Journal of Phase Equilibria and Diffusion* 33 (2012) 443-449.
3. K. Huang, **Y. Park**, D.D. Keiser Jr., Y.H. Sohn. Interdiffusion between Potential Diffusion Barrier Mo and U-Mo Metallic Fuel Alloy for RERTR Applications. *Journal of Equilibria and Diffusion* 34 (2013) 307-312.
4. K. Huang, **Y. Park**, B.H. Sencer, J.R. Kennedy, K.R. Coffey, Y.H. Sohn. Effects of Cr and Ni on interdiffusion and reaction between U and Fe-Cr-Ni alloys. *Journal of Nuclear Materials* 431 (2014) 372-378.
5. **Y. Park**, K. Huang, A. Paz y Puente, H.S. Lee, B.H. Sencer, J.R. Kennedy, Y.H. Sohn. Diffusional Interaction Between U-10 wt pct Zr and Fe at 903 K, 923 K, and 953 K (630 °C, 650 °C, and 680 °C). *Metallurgical and Materials Transaction A* (2014) 1-11.
6. **Y. Park**, J. Yoo, K. Huang, D. D. Keiser Jr., J. F. Jue, B. Rabin, G. Moore, Y. H. Sohn. Growth Kinetics and Microstructural Evolution during Hot Isostatic Pressing of U-10 wt.% Mo Monolithic Fuel Plate in AA6061 Cladding with Zr Diffusion Barrier. *Journal of Nuclear Materials* 447 (2014) 215-224.
7. L. Shao, D. Chen, C. Wei, M. Martin, X. Wang, B. H. Sencer, J.R. Kennedy, **Y. Park**, E. Dein, K. R. Coffey, Y. H. Sohn. Radiation effects on interface reactions of U/Fe, U/(Fe+Cr), and U/(Fe+Cr+Ni). *Journal of Nuclear Materials* 456 (2015) 302-310.
8. **Y. Park**, D. D. Keiser Jr., Y. H. Sohn. Diffusional Interactions between U-Mo and Zr at 650 °C as a Function of Time. *Journal of Nuclear Materials* 456 (2015) 31-358.
9. **Y. Park**, N. Eriksson, D. D. Keiser Jr., J. F. Jue, B. Robin, G. Moore, Y. H. Sohn. Microstructural anomalies in hot-isostatic pressed U-10 wt.%Mo fuel plates with Zr diffusion barrier. *Materials Characterization* 103 (2015) 50-57.

2. Conference Presentations

1. K. Huang, **Y. Park**, A. Ewh, Y. H. Sohn. Metallic Nuclear Fuel Study at University of Central Florida (UCF), 3rd Florida Energy Systems Consortium (FESC) Summit, Gainesville, Florida USA, September 27-28, 2011.
2. K. Huang, **Y. Park**, B.H. Sencer, J.R. Kennedy, K.R. Coffey, Y. H. Sohn. Interdiffusion and Reaction of Uranium and Iron, Materials Science & Technology 2011 (MS&T'11), Columbus, Ohio USA, October 16-20, 2011.
3. K. Huang, **Y. Park**, D. D. Keiser Jr., Y. H. Sohn. Observations and Analyses of Diffusion Couples, U-10 wt.% Mo vs. Zr, The Minerals, Metals & Materials Society 2012 Annual Meeting (TMS'12), Orlando, Florida USA, March 11-15, 2012.
4. **Y. Park**, K. Huang, B. Sencer, J. Kennedy, Y. H. Sohn. Interdiffusion between U - 10wt.% Zr and Fe Diffusion Couples Annealed at 903, 923, 953 and 973K. The Minerals, Metals & Materials Society 2012 Annual Meeting (TMS'12), Orlando, Florida USA, March 11-15, 2012.
5. **Y. Park**, K. Huang, B. Sencer, J. Kennedy, Y. H. Sohn. Interdiffusion between U-10wt.%Zr and Fe-15wt.%Cr-15wt.%Ni Diffusion Couples Annealed at 600, 650 and 700 °C. Materials Science & Technology 2012 (MS&T'12), Pittsburgh, Pennsylvania USA, October 07-11, 2012.
6. **Y. Park**, K. Hunag, B. Sencer, J. Kennedy, Y. H. Sohn. Interdiffusion and Reaction between U-Zr and Fe-Cr-Ni alloys. 2012 Materials Research Society Fall Meetings & Exhibits ('12 MRS Fall), Boston, Massachusetts USA, November 25-30, 2012.
7. **Y. Park**, K. Huang, B. Sencer, J. Kennedy, K. Coffey, Y. H. Sohn. Interdiffusion and Reaction between U-Zr and Fe-Cr-Ni Alloys. The Minerals, Metals & Materials Society 2013 Annual Meeting (TMS'13), San Antonio, Texas USA, March 3-7, 2013.
8. **Y. Park**, J. Kang, D. D. Keiser Jr., Y. H. Sohn. Development of Phase Constituents and Microstructure in Monolithic U-Mo Fuel Plate Assembly during Hot Isostatic Pressing. The Minerals, Metals & Materials Society 2014 Annual Meeting (TMS'14), San Diego, California USA, February 16-20, 2014.
9. **Y. Park**, K. Huang, D. D. Keiser Jr., Y. H. Sohn. Growth Kinetics and Microstructural Evolution during Hot Isostatic Pressing of U-Mo Monolithic Fuel Plate in AA6061 Cladding with Zr Diffusion Barrier. Advanced Test Reactor National Scientific User Facility User's Meeting 2014 (ATR User Meeting'14), Falls, Idaho USA, June 4-6, 2014.
10. **Y. Park**, K. Huang, D. D. Keiser Jr., Y. H. Sohn. Interdiffusion Reaction between U-Zr Alloy and Fe. Advanced Test Reactor National Scientific User Facility User's Meeting 2014 (ATR User Meeting'14), Falls, Idaho USA, June 4-6, 2014.

11. **Y. Park**, K. D. D. Keiser Jr., Y. H. Sohn. Microstructural Evolution in Zr-Laminated U-Mo Fuel Plate Encased in AA6061 Cladding during Hot Isostatic Pressing. US-Korea Conference 2014 (UKC2014), San Francisco, California USA, August 6-9, 2014.
12. **Y. Park**, N. Eriksson, D. D. Keiser Jr., Y. H. Sohn. Microstructural Anomalies in Hot-Isostatic Pressed U-10 wt.%Mo Fuel Plates with Zr Diffusion Barrier. Materials Science & Technology 2014 (MS&T'14), Pittsburgh, Pennsylvania USA, October 12-16, 2014.
13. N. Eriksson, **Y. Park**, D. D. Keiser Jr., Y. H. Sohn. Phase Transformations and Microstructural Evolution in the U-10 wt.%Mo Alloy with Various Zr Additions. Materials Science & Technology 2014 (MS&T'14), Pittsburgh, Pennsylvania USA, October 12-16, 2014.
14. **Y. Park**, N. Eriksson, D. D. Keiser Jr., Y. H. Sohn. Microstructural Development in Hot-Isostatic Pressed U - 10 wt.% Mo Fuel Plates with Zr Diffusion Barrier. The Nuclear Materials Conference (NuMat'14), Clearwater, Florida USA, October 27-30, 2014.
15. **Y. Park**, K. Huang, K. R. Coffey, Y. H. Sohn, B. H. Sencer, J. R. Kennedy. Interdiffusion and Reaction between U-10 wt.%Zr and Fe-Cr-Ni Alloys. The Nuclear Materials Conference (NuMat'14), Clearwater, Florida USA, October 27-30, 2014.
16. **Y. Park**, D. D. Keiser Jr., Y. H. Sohn. Interdiffusion and Reaction between U-Mo and Zr at 650 °C as a Function of Time. The Minerals, Metals & Materials Society 2015 Annual Meeting (TMS'15), Orlando, Florida USA, March 15-19, 2015.
17. **Y. Park**, N. Eriksson, D. D. Keiser Jr., Y. H. Sohn. Evaluation of phase constituents and microstructure in hot isostatic pressed monolithic U-Mo fuel plates in AA6061 cladding with Zr diffusion barrier. The Minerals, Metals & Materials Society 2015 Annual Meeting (TMS'15), Orlando, Florida USA, March 15-19, 2015.
18. **Y. Park**, N. Eriksson, D. D. Keiser Jr., Y. H. Sohn. Phase transformation of γ -U (U-10 wt.% Mo) in hot isostatic pressed fuel plates. Materials Science & Technology 2015 (MS&T'15), Columbus, Ohio USA, October 4-8, 2015.
19. N. Eriksson, F. Bentancor, **Y. Park**, D. D. Keiser Jr., Y. H. Sohn. Phase transformation of microstructural evolution in the U-10Mo-xZr (x=0, 0.5, 1, 2, 5, 10, 20) alloys with various heat treatments. Materials Science & Technology 2015 (MS&T'15), Columbus, Ohio USA, October 4-8, 2015.
20. A. Mehta, **Y. Park**, D. D. Keiser Jr., Y. H. Sohn. Interdiffusion and reaction in Al vs. Zr and Al vs. Mo solid-to-solid diffusion. Materials Science & Technology 2015 (MS&T'15), Columbus, Ohio USA, October 4-8, 2015.
21. **Y. Park**, N. Eriksson, D. D. Keiser Jr., Y. H. Sohn. Microstructural development and phase transformations in hot isostatic pressed monolithic U-Mo fuel plates in AA6061 cladding with Zr

diffusion barrier. The Minerals, Metals & Materials Society 2016 Annual Meeting (TMS'16), Nashville, Tennessee USA, February 14-18, 2016.

22. A. Mehta, **Y. Park**, D. D. Keiser Jr., Y. H. Sohn. Interdiffusion and reaction between Al vs. X (X = Zr, Mo, U) diffusion couples. The Minerals, Metals & Materials Society 2016 Annual Meeting (TMS'16), Nashville, Tennessee USA, February 14-18, 2016.

LIST OF REFERENCE

- [1] G.L. Hofman, L.C. Walters, T.H. Bauer, *Progress in Nuclear Energy*, 31 (1997) 83-110.
- [2] D. Petti, D. Crawford, N. Chauvin, *MRS Bulletin*, 34 (2009) 40-45.
- [3] T. Sofu, *Nuclear Engineering and Technology*, 47 (2015) 227-239.
- [4] A.E. Dwight, *Journal of Nuclear Materials*, 2 (1960) 81-87.
- [5] S.P. Garg, R.J. Ackermann, *Journal of Nuclear Materials*, 64 (1977) 265-274.
- [6] A. Saroja, Y.J. Bhatt, S.P. Garg, *Journal of the Less Common Metals*, 114 (1985) 291-297.
- [7] S.C. Parida, S. Dash, Z. Singh, R. Prasad, V. Venugopal, *Journal of Physics and Chemistry of Solids*, 62 (2001) 585-597.
- [8] X. Zhang, Y.F. Cui, G.L. Xu, W.J. Zhu, H.S. Liu, B.Y. Yin, Z.P. Jin, *Journal of Nuclear Materials*, 402 (2010) 15-24.
- [9] L.B. Lundberg, *Journal of Nuclear Materials*, 167 (1989) 64-75.
- [10] K. Huang, D.D. Keiser, Y. Sohn, *Metall and Mat Trans A*, 44 (2012) 738-746.
- [11] V.V. Kalashnikov, V.V. Titova, G.I. Sergeev, A.G. Samoilov, *At Energy*, 5 (1959) 1315-1325.
- [12] A.L. Lotts, Oak Ridge National laboratory, 1960.
- [13] M.K. Meyer, G.L. Hofman, S.L. Hayes, C.R. Clark, T.C. Wiencek, J.L. Snelgrove, R.V. Strain, K.H. Kim, *Journal of Nuclear Materials*, 304 (2002) 221-236.
- [14] A. Leenaers, S. Van den Berghe, E. Koonen, C. Jarousse, F. Huet, M. Trotabas, M. Boyard, S. Guillot, L. Sannen, M. Verwerft, *Journal of Nuclear Materials*, 335 (2004) 39-47.
- [15] A. Leenaers, S. Van den Berghe, W. Van Renterghem, F. Charollais, P. Lemoine, C. Jarousse, A. Röhrmoser, W. Petry, *Journal of Nuclear Materials*, 412 (2011) 41-52.
- [16] A.B. Robinson, G.S. Chang, D.D. Keiser Jr, D.M. Wachs, D.L. Porter, Idaho National Laboratory, Falls, Idaho, 2009.
- [17] D.D.J. Keiser, B. Miller, J. Madden, J.-F. Jue, J. Gan, *Microscopy Today*, 22 (2014) 30-35.
- [18] J.L. Snelgrove, G.L. Hofman, M.K. Meyer, C.L. Trybus, T.C. Wiencek, *Nuclear Engineering and Design*, 178 (1997) 119-126.
- [19] K.H. Kim, D.B. Lee, C.K. Kim, G.E. Hofman, K.W. Paik, *Journal of Nuclear Materials*, 245 (1997) 179-184.
- [20] D.D. Keiser, Jr., S.L. Hayes, M.K. Meyer, C.R. Clark, *JOM*, 55 (2003) 55-58.
- [21] W.J. Carmack, *Nuclear Engineering*, University of Idaho, University of Idaho, 2012.
- [22] D.C. Fee, C.E. Johnson, *Journal of Nuclear Materials*, 96 (1981) 80-104.

- [23] R.C. Vogel, L. Burris, A.D. Tevebaugh, D.S. Webster, E.R. Proud, Argonne National Laboratory, Argonne National Laboratory, 1969.
- [24] K. Huang, Y. Park, A. Ewh, B.H. Sencer, J.R. Kennedy, K.R. Coffey, Y.H. Sohn, *Journal of Nuclear materials*, 424 (2012) 82-88.
- [25] K. Nakamura, T. Ogata, M. Kurata, A. Itoh, M. Akabori, *Journal of Nuclear materials*, 275 (1999) 246-254.
- [26] T. Ogata, M. Kurata, K. Nakamura, A. Itoh, M. Akabori, *Journal of Nuclear materials*, 250 (1997) 171-175.
- [27] D.D. Keiser Jr, M.A. Dayananda, *Journal of Nuclear materials*, 200 (1993) 229-243.
- [28] D. Keiser, M. Dayananda, *Metall and Mat Trans A*, 25 (1994) 1649-1653.
- [29] H.J. Ryu, Y.S. Han, J.M. Park, S.D. Park, C.K. Kim, *Journal of Nuclear Materials*, 321 (2003) 210-220.
- [30] H. Ryu, J. Park, C. Kim, Y. Kim, G. Hofman, *Journal of Phase Equilibria and Diffusion*, 27 (2006) 651-658.
- [31] E. Perez, D.D. Keiser, Jr., Y.H. Sohn, *Metall and Mat Trans A*, 42 (2011) 3071-3083.
- [32] M.I. Mirandou, S.N. Balart, M. Ortiz, M.S. Granovsky, *Journal of Nuclear Materials*, 323 (2003) 29-35.
- [33] Y.S. Kim, G.L. Hofman, J.S. Cheon, *The 34th Interational Meeting on Reduced Enrichment for Research and Test Reactors*, Warsaw, Poland, 2012.
- [34] H. Palancher, P. Martin, V. Nassif, R. Tucoulou, O. Proux, J.-L. Hazemann, O. Tougait, E. Lahera, F. Mazaudier, C. Valot, S. Dubois, *Journal of Applied Crystallography*, 40 (2007) 1064-1075.
- [35] F. Mazaudier, C. Proye, F. Hodaj, *Journal of Nuclear Materials*, 377 (2008) 476-485.
- [36] D.D. Keiser Jr, J.-F. Jue, B. Yao, E. Perez, Y. Sohn, C.R. Clark, *Journal of Nuclear Materials*, 412 (2011) 90-99.
- [37] B. Yao, E. Perez, D.D. Keiser Jr, J.-F. Jue, C.R. Clark, N. Woolstenhulme, Y. Sohn, *Journal of Alloys and Compounds*, 509 (2011) 9487-9496.
- [38] K. Huang, C.C. Kammerer, D.D. Keiser, Jr., Y.H. Sohn, *Journal of Phase Equilibria and Diffusion*, 35 (2014) 146-156.
- [39] E. Perez, B. Yao, D.D. Keiser Jr, Y.H. Sohn, *Journal of Nuclear Materials*, 402 (2010) 8-14.
- [40] V.F. Sears, *Neutron News*, 3 (1992) 26-37.
- [41] *Springer Handbook of Condensed Matter and Materials Data*, Springer Berlin Heidelberg, 2006.
- [42] *ASM Metals Handbook-Corrosion*.

- [43] K. Huang, Y. Park, D.D. Keiser, Jr., Y.H. Sohn, *Journal of Phase Equilibria and Diffusion*, 33 (2012) 443-449.
- [44] G.A. Moore, M.C. Marshall, Idaho National Laboratory, 2010.
- [45] G.A. Moore, F.J. Rice, N.E. Woolstenhulme, J.F. Jue, B.H. Park, S.E. Steffler, N.P. Hallinan, M.D. Chapple, M.C. Marshall, B.I. Mackowiak, C.R. Clark, B.H. Rabin, Idaho National Laboratory, 2009.
- [46] J.-F. Jue, D.D. Keiser Jr, C.R. Breckenridge, G.A. Moore, M.K. Meyer, *Journal of Nuclear Materials*, 448 (2014) 250-258.
- [47] G.A. Moore, F.J. Rice, N.E. Woolstenhulme, W.D. Swank, D. Haggard, J. Jue, B.H. Park, S.E. Steffler, N.P. Hallinan, M.D. Chapple, *Proceedings of RERTR 2008 30th International Meeting on Reduced Enrichment for Research and Test Reactors*, Washington, DC USA, 2008.
- [48] S. Van Den Berghe, A. Leenaers, E. Koonen, L. Sannen, *Advances in Science and Technology*, 73 (2010) 78-90.
- [49] P. Lemoine, D. Wachs, *Global 2007-Advanced Nuclear Fuel Cycles and Systems*, 2007.
- [50] A. Travelli, *The 24th International Meeting on Reduced Enrichment for Research and Test Reactors*, San Carlos de Bariloche, Argentina, 2002.
- [51] A. Glaser, *Proceedings of the 26th RERTR Meeting*, 2004, pp. 7-12.
- [52] H. Okamoto, *Journal of Phase Equilibria and Diffusion*, 33 (2012) 497-497.
- [53] H.L. Yakel, Oak Ridge National Laboratory, 1974.
- [54] C.V. Sundaram, S.L. Mannan, *Sadhana*, 14 (1989) 21-57.
- [55] R.L. Miller, G.A. Reimann, Idaho National Engineering Laboratory, 1993.
- [56] M.M. Baker, L.N. Less, S. Orman, *Transactions of the Faraday Society*, 62 (1966) 2525-2530.
- [57] J.M. Macki, R.L. Kochen, The Dow Chemical Company, 1971.
- [58] V.F. Peretrukhin, A.G. Maslennikov, A.Y. Tsivadze, C.H. Delegard, A.B. Yusov, V.P. Shilov, A.A. Bessonov, K.E. German, A.M. Fedoseev, L.P. Kazanskii, N.Y. Budanova, A.V. Kareta, A.V. Gogolev, K.N. Gedgovd, G.S. Bulatov, *Prot Met*, 44 (2008) 211-232.
- [59] W.R. McDonell, G.R. Caskey, C.L. Angerman, Westinghouse Savannah River Company 1975, pp. 23-30.
- [60] G. Beghi, European Atomic Energy Community, 1968, pp. 82.
- [61] M.K. Meyer, J. Gan, J.F. Jue, D.D. Keiser Jr, E. Perez, A. Robinson, D.M. Wachs, N. Woolstenhulme, G.L. Hofman, Y.S. Kim, *Nuclear Engineering and Technology*, 46 (2014) 169-182.
- [62] M. Lehmann, *Journal of Nuclear Materials*, 2 (1960) 261-268.
- [63] P.E. Repas, R.H. Goodenow, R.F. Hehemann, *Transactions of the ASM*, 57 (1964) 150-163.

- [64] C.A.W. Peterson, W.J. Steele, S.L. DiGiallonardo, Other Information: Orig. Receipt Date: 31-DEC-65, 1964, pp. Medium: ED; Size: Pages: 28.
- [65] S. Neogy, M.T. Saify, S.K. Jha, D. Srivastava, M.M. Hussain, G.K. Dey, R.P. Singh, *Journal of Nuclear Materials*, 422 (2012) 77-85.
- [66] G.L. Hofman, M.K. Meyer, The 21th International Meeting on Reduced Enrichment for Research and Test Reactors, Sao Paulo, Brazil, 1998.
- [67] B.-S. Seong, C.-H. Lee, J.-S. Lee, H.-S. Shim, J.-H. Lee, K.H. Kim, C.K. Kim, V. Em, *Journal of Nuclear Materials*, 277 (2000) 274-279.
- [68] P. Villars, K. Cenzual (Eds.), Springer-Verlag Berlin Heidelberg & Material Phases Data System (MPDS), Switzerland & National Institute for Materials Science (NIMS), Japan.
- [69] P. Villars, K. Cenzual (Eds.), Springer-Verlag Berlin Heidelberg & Material Phases Data System (MPDS), Switzerland & National Institute for Materials Science (NIMS), Japan.
- [70] P. Villars, K. Cenzual (Eds.), Springer-Verlag Berlin Heidelberg & Material Phases Data System (MPDS), Switzerland & National Institute for Materials Science (NIMS), Japan.
- [71] B.R.T. Frost, *Journal of Nuclear Materials*, 10 (1963) 265-300.
- [72] A.M. Nomine, D. Bedere, D. Miannay, in: J.J. Burke, D.A. Colling, A.E. Gorum, J. Greenspan (Eds.) *Proceedings of the Third Army Materials Technical Conference*, Brook Hill Publishing Company, Vail, CO, 1974, pp. 657–699.
- [73] S. Jaroszewicz, E.L. Losada, J.E. Garcés, H.O. Mosca, *Journal of Nuclear Materials*, 441 (2013) 119-124.
- [74] H.A. Saller, F.A. Rough, A.A. Bauer, Battelle Memorial Institute, 1955.
- [75] R.M. Willard, A.R. Schmitt, *Atomics International*, 1965.
- [76] K.H. Kim, H.J. Kwon, J.M. Park, Y.S. Lee, C.K. Kim, *Journal of the Korean Nuclear Society*, 33 (2001) 365-374.
- [77] E.K. Halteman, *Acta crystallographica*, 10 (1957) 166-169.
- [78] R.J. Jackson, *Metallurgy*, Iowa State University, Ames, Iowa, 1964, pp. 162.
- [79] P.E. Armstrong, D.T. Eash, J.E. Hockett, *Journal of Nuclear Materials*, 45 (1972) 211-216.
- [80] S.L. Robinson, *Journal of Nuclear Materials*, 46 (1973) 293-302.
- [81] D.E. Burkes, G.S. Mickum, D.M. Wachs, Idaho National Laboratory, 2010.
- [82] T.R.G. Kutty, S. Dash, J. Banerjee, S. Kaity, A. Kumar, C.B. Basak, *Journal of Nuclear Materials*, 420 (2012) 193-197.
- [83] A. Paul, T. Laurila, V. Vuorinen, S.V. Divinski, *Thermodynamics, diffusion and the Kirkendall effect in solid*, Springer, 2014.
- [84] L. Boltzmann, *Ann. der Physik und Chemie*, 53 (1894) 959-964.

- [85] C. Matano, *Japanese Journal of Physics*, (1933) 109-113.
- [86] M.A. Dayananda, C.W. Kim, *Metallurgical Transactions A*, 10 (1979) 1333-1339.
- [87] F. Sauer, V. Freise, *Zeitschrift für Elektrochemie*, 66 (1962) 353-362.
- [88] C. Wagner, *Acta Metallurgica*, 17 (1969) 99-107.
- [89] Y. Park, J. Yoo, K. Huang, D.D. Keiser Jr, J.F. Jue, B. Rabin, G. Moore, Y.H. Sohn, *Journal of Nuclear Materials*, 447 (2014) 215-224.
- [90] H. Okamoto, *Journal of Phase Equilibria*, 14 (1993) 267-268.
- [91] U.D.o. Energy, O.o.N. Energy, S.a. Technology, Report to Congress, (2006).
- [92] D.E. Burkes, R.S. Fielding, D.L. Porter, D.C. Crawford, M.K. Meyer, *Journal of Nuclear Materials*, 389 (2009) 458-469.
- [93] M.C. Petri, M.A. Dayananda, Argonne National Laboratory, 1996.
- [94] M.C. Petri, M.A. Dayananda, *Philosophical Magazine A*, 76 (1997) 1169-1185.
- [95] M.C. Petri, M.A. Dayananda, *Journal of Nuclear Materials*, 240 (1997) 131-143.
- [96] Y.H. Sohn, M.A. Dayananda, G.L. Hofman, R.V. Strain, S.L. Hayes, *Journal of Nuclear Materials*, 279 (2000) 317-329.
- [97] T. Ogata, M. Akabori, A. Itoh, T. Ogawa, *Journal of Nuclear Materials*, 232 (1996) 125-130.
- [98] Y. Adda, J. Philibert, H. Faraggi, *REVUE DE METALLURGIE-CAHIERS D INFORMATIONS TECHNIQUES*, 54 (1957) 597.
- [99] M. Akabori, A. Itoh, T. Ogawa, T. Ogata, *Journal of Alloys and Compounds*, 271-273 (1998) 597-601.
- [100] P. Duwez, *Journal of Applied Physics*, 24 (1953) 152-156.
- [101] E. Perez, Y.-H. Sohn, D.D. Keiser, *Metall and Mat Trans A*, 44 (2012) 584-595.
- [102] D. Burkes, N. Hallinen, J. Wight, M. Chapple, RERTR, 2007.
- [103] N.A. Mara, 33rd International Meeting on Reduced Enrichment for Research and Test Reactors, 2011.
- [104] M.K. Meyer, G.A. Moore, J.F. Jue, D.D. Keiser Jr, I.Y. Glagolenko, D.M. Wachs, P.E. Murray, A.B. Robinson, F.J. Rice, H. Ozaltun, S.J. Miller, M.A. Okuniewski, B.H. Rabin, H.W. Glunz, N.J. Lybeck, Idaho National Laboratory, 2012.
- [105] V.K. Orlov, V.S. Sergeev, M.A. Fomishkin, A.A. Rostovtsev, A.K. Kruglov, *Atomic Energy*, 95 (2003) 536-539.
- [106] D.E. Burkes, R. Prabhakaran, T. Hartmann, J.-F. Jue, F.J. Rice, *Nuclear Engineering and Design*, 240 (2010) 1332-1339.
- [107] K.G. Hoge, *Journal of Basic Engineering*, 88 (1966) 509-517.

- [108] S.M. Lang, F.P. Knudsen, C.L. Fillmore, R.S. Roth, 1956.
- [109] F.A. Halden, H.C. Wohlers, R.H. Reinhart, Other Information: Orig. Receipt Date: 31-DEC-60, 1959, pp. Medium: ED; Size: Pages: 24.
- [110] A.C.J. Secrest, E.L. Foster, R.F. Dickerson, Other Information: Orig. Receipt Date: 31-DEC-59, 1959, pp. Medium: ED; Size: Pages: 17.
- [111] G.A. Meerson, R.B. Kotel'nikov, S.N. Bashlykov, Journal of Nuclear Energy. Parts A/B. Reactor Science and Technology, 16 (1962) 485-488.
- [112] J. Belle, United States Atomic Energy Commission, Washington, DC, 1981.
- [113] S. Van den Berghe, A. Leenaers, The 34th Interational Meeting on Reduced Enrichment for Research and Test Reactors, Warsaw, Poland, 2012.
- [114] J.K. Jain, S.P. Gupta, Materials Characterization, 49 (2002) 139-148.
- [115] J. Dickson, L. Zhou, A. Paz y Puente, M. Fu, D.D. Keiser Jr, Y.H. Sohn, Intermetallics, 49 (2014) 154-162.
- [116] D.A. Lopes, T.A. Guisard Restivo, A.F. Padilha, Journal of Nuclear Materials, 440 (2013) 304-309.
- [117] K.H. Kim, H.S. Ahn, J.M. Park, C.K. Kim, D.S. Sohn, RRFM '98. 2nd International topical meeting on research reactor fuel management, Berne, Switzerland, 1998, pp. 176-180.
- [118] N.-T.H. Kim-Ngan, I. Tkach, S. Mašková, L. Havela, A. Warren, T. Scott, Advances in Natural Sciences: Nanoscience and Nanotechnology, 4 (2013) 035006.